Hippocampal Coordination of Navigation, Reward, and Epilepsy Circuits

by

Danny Siu

A dissertation submitted in partial fulfillment
of the requirements for the degree of
Doctor of Philosophy
(Psychology)
in the University of Michigan
2022

Doctoral Committee:

 Assistant Professor Omar J. Ahmed, Chair
 Associate Professor Kamran Diba
 Professor Miriam Meisler
 Professor Terry Robinson

Danny Siu

dsiu@umich.edu

ORCID iD: 0000-0003-0742-233X

DEDICATION

This dissertation is dedicated mainly to the two most important women in my life.

To my wife Sakura for listening to my rambles about the PhD process and people, making this experience bearable.

To my sister Christina who first walked down the PhD path with no guidance, who encouraged me to pursue what I wanted instead of what I was told, and who taught me all her mistakes so that I wouldn't have to experience those hardships myself.

I also dedicate this to my parents who left Vietnam and gave me this opportunity in America to begin with.

ACKNOWLEDGEMENTS

First and foremost I have to thank the Biopsychology program and my advisor Dr. Omar Ahmed who took a gamble with me, a student with a barely passing GPA. I inherently prefer to get things done quickly rather than accurately, and you forced me to have higher standards of detail for better or worse. You've always held high expectations and we had a couple of memorable disagreements, but as a result I think surviving all of that has prepared me for anything else in my future.

I dedicate this next section to the members of the Omar lab. Thanks to Dr. Ellen Brennan and Izabela Jedrasiak-Cape for their inputs on colors and Adobe Illustrator so that we have eye popping figures. Thanks to Megha Ghosh for all the conversations on analytics, as well as Tibin John, Alcides Lorenzo Gonzales, Dr. Tyler Ekins and everybody else in the lab for the fun late night philosophical conversations. A special thanks to Dr. Allison Ahrens and Vaughn Hetrick for collecting the data that makes this thesis possible. Seriously, I would have never been able to develop either of your necessary surgical prowess and careful experimental skills. I tried and found out I'm not very good at it. Lastly, I thank the rats and mice of the Omar lab for cooperating and being a part of this research.

My journey to graduate school would not have been possible without the opportunities during my undergraduate education at UC Irvine. Dr. Yama Akbari was my very first exposure to the realm of research. I felt like the possibilities were endless and you constantly encouraged

us to present our work. You were able to acknowledge when we were going through rough patches in life and reminded us of our worth. All of this support made getting into graduate school possible in the first place. I would also like to thank Dr. Beth Lopour for our collaborations and teaching the Akbari Lab how to do signal processing properly, as well as Dr. Salomi Asaridou for your advice and help with graduate school applications.

I also have to acknowledge my close friends prior to graduate school who made life hilarious. To Nam Hoang who ate lunch with me every day in high school for no particular reason. We've grown a lot together in incomprehensible ways in the last decade. To Lauren Lee, my hustling partner in crime where we became friends because you happened to play some video games. You luckily taught me a semblance of normality during undergrad. I have no clue why but working with you created a crazy positive feedback loop of energy that compelled us to work on undergraduate research *for free* at coffee shops until they closed every other night. To the "BFF" group Rachel Jang, Victor Quach, and Garvey Xu where we somehow found time to play League and Valorant despite our busy schedules. I lost some sleep and we'll always be hardstuck bronze but it's a journey we will tread together. To my friends Areeb Baig, Joe Greene, Michael Housworth, Raul Ibarra, Zeed Jarrah, and Tara Johnson in Discord (formerly Skype, formerly Xfire) where we kept in touch but never learned to be normal.

Lastly I'd like to acknowledge my friends at Michigan that made my time here more memorable. Special thanks to Dr. Michael Demidenko and Katie Demidenko for providing a place for Sakura and I to live in for an unexpected extended period of time. That was one of my favorite chaotic months in my life. It was a wild ride watching the market crash in March 2019 together in real time with all the trading halts, followed by our amateur analysis of which airline

would survive (surprise surprise, it was none of the ones we predicted). Thanks to Daniel Geiszler for being my first and last roommate, the camping crew for showing the wonders of the Michigan outdoors, as well as everybody else that attended our yearly Friendsgiving celebrations. Oh, and I thank my dog Winry Joestar for helping me get out of the house more to touch some grass.

TABLE OF CONTENTS

LIST OF TABLES

Abstract

The successful acquisition of food is critical for mammalian survival and necessitates a neural mechanism that allows for rapid association of location, context, and reward information. Many of these fundamental computations relating to spatial navigation and learning have been shown to coordinate with hippocampal oscillations including theta rhythms and sharp wave ripples (SWRs). The hippocampus is also impaired in various disease states including epileptic encephalopathy. In this dissertation, we describe how hippocampal oscillations may contribute to neural circuits relating to spatial navigation, reward, and epilepsy. In Chapter 2, we identify novel angular head velocity cells in the nucleus accumbens (NAcc) and ventral pallidum (VP), two essential regions in the mesolimbic reward circuit. We show that these head velocity cells are state-dependent, where head velocity encoding is selectively lost during motivated tasks, and is instead replaced by cue and reward encoding. The loss of AHV encoding is correlated to increases in the hippocampal theta rhythm. These results indicate that the NAcc and VP are well suited to precisely track head rotations before transitioning to support the motivated acquisition of reward. In Chapter 3 we show that neurons in the NAcc and VP also coordinate with hippocampal SWRs. Reactivation of neuronal ensembles during SWRs are thought to be one mechanism of memory consolidation. We identified multi-timescale responses of the NAcc and VP during SWRs outside of the task, which were associated with greater likelihood of cue responses during the task. Finally, in Chapter 4, we show the hippocampal contributions in a

rodent model of epileptic encephalopathy, where we observed hippocampal epileptic activity during both fatal and non-fatal seizures. Together these results further our understanding of how the hippocampus contributes to healthy and pathological circuit computations.

Chapter 1: Introduction

The research presented in the following three chapters may appear to span a range of diverse topics, but these topics are tied together by one key ingredient: the hippocampus and its oscillations. In this introduction, I review the basics of hippocampal oscillations and how they relate to state-dependent behavior, as well as to epilepsy. Each of the individual chapters then provides an additional introduction that reviews the chapter-specific background information.

1.1   Hippocampal oscillations

1.1.1   Theta

Hippocampal theta rhythms are the largest oscillation in the rodent brain (Buzsaki, 2002) and are consistently present during various types of locomotor activities such as voluntary, preparatory, orienting, or exploratory behavior (Vanderwolf, 1969). In general, theta waves are absent in the immobile animal, and are not present during automatic movements like grooming or reward consumption. (Buzsáki, 2005; Vanderwolf, 1969). On the other hand, active states - those involving either running or motivated behaviors - are consistently associated with large increases in hippocampal theta rhythms (Ahmed & Mehta, 2012; Aronov et al., 2017; Furtak et al., 2012; Ghosh et al., 2020; Schultheiss et al., 2020; Tsanov, 2017).

The theta oscillation can be found in the range of 4-12 Hz, or 4-12 cycles per second, but the theta rhythm is defined differently in various species such as 7-9 Hz in rodents, 4-7 Hz in dogs, and 4-8 Hz in humans (Foo & Bohbot, 2020). Traditionally, hippocampal theta oscillations

are thought to originate from projections from the medial septum (MS), since inactivation of the

MS reliably impairs hippocampal theta (Buzsaki, 2002; Colgin, 2013; Yoder & Pang, 2005). As

a result, studies attempting to investigate the causal impact of hippocampal theta oscillations on

behavior commonly utilize MS inactivations (Brandon et al., 2014; Lamprea et al., 2010;

Leutgeb & Mizumori, 1999; Pastor et al., 2020; Rashidy-Pour et al., 1995). Manipulations of

indirectly connected regions also modulate hippocampal theta, such as the vestibular nuclei

(Aitken et al., 2018; Russell et al., 2006) and ventral tegmental area (Orzeł-Gryglewska et al.,

2012). Despite the clear contributions of the medial septum to theta rhythms, in vitro

experiments using isolated hippocampal slices suggest that the hippocampus contains the

intrinsic machinery necessary to self-generate theta oscillations, and that the MS more likely

helps facilitate the hippocampal neuronal population to shift into a theta generating state

(Goutagny et al., 2009). Furthermore, there may be multiple local generators of theta oscillations

within the hippocampus (Buzsaki, 2002; Kocsis et al., 1999)(Goutagny et al., 2009; Lubenov &

Siapas, 2009)(Goutagny et al., 2009; Lubenov & Siapas, 2009)(Goutagny et al., 2009; Lubenov

& Siapas, 2009).

1.1.2   Sharp wave ripples

The hippocampus is known to be involved in spatial navigation and memory, playing an

important role in both navigation towards rewards as well as the learning of reward-related

information (Agarwal et al., 2014; O'Keefe et al., 1971). These processes take place through

hippocampal replay during sharp wave ripples (SWRs). During periods of quiet wakefulness and

non-rapid eye movement (non-REM) sleep, neuronal ensembles replay prior experiences during

SWRs. Indeed, populations of cells encoding properties such as reward and head direction have

been shown to preferentially re-activate during hippocampal SWRs (Lansink et al., 2008; Viejo

& Peyrache, 2020), and precise perturbations of these SWR events lead to worse behavioral performance (Girardeau et al., 2009; S. P. Jadhav et al., 2012). SWR reactivation is also stronger after undergoing behavior in the prefrontal cortex, amygdala, and more importantly in the context of this thesis, the ventral striatum (Girardeau et al., 2017; S. P. P. Jadhav et al., 2016; Lansink et al., 2008). SWR amplitudes are larger following tasks and are longer under increased cognitive demand (Eschenko et al., 2008; Fernández-Ruiz et al., 2019). While hippocampal theta is supported and generated by MS cholinergic inputs, ripples cannot occur during cholinergic states, indicating these are two orthogonally occurring brain rhythms.

Hippocampal SWRs in the CA1 are characterized by a slow, high amplitude sharp wave (~10Hz) followed by a brief 100-250 Hz oscillation lasting up to 100ms (Buzsáki, 2015). CA1 SWRs are thought to be initiated by synchronous pyramidal cell activity in hippocampal CA3, which excites pyramidal neurons in the CA1, generating the characteristic sharp wave. The pyramidal neurons then induce local reciprocal inhibition within interneurons in the CA1, eliciting the high frequency ripple event (Buzsáki, 2015; Schlingloff et al., 2014). Notably, the mechanism of SWRs and hippocampal gamma rhythms are different – gamma rhythms are thought to be generated through pyramidal-interneuron networks whereas SWRs are likely due to interneuron-interneuron networks (Schlingloff et al., 2014; Tiesinga & Sejnowski, 2009). The frequency of SWRs are thought to be primarily set by the reciprocal inhibition whereas the duration and amplitude are influenced by the strength of excitatory input from the CA3 (Schlingloff et al., 2014).

1.2 Behavior

1.2.1 Spatial navigation

The ability to quickly learn new environments with accurate internal representations and having the capacity to traverse them are essential functions for survival. These computations can be performed using external sensory stimuli and previously learned landmarks creating an allocentric representation of the environment. Alternatively, using self-motion (idiothetic) cues such as motor, vestibular, and optic flow, animals can estimate perceived distance and direction with an egocentric frame of reference, a strategy known as path integration (Etienne & Jeffery, 2004; Séguinot et al., 1993). These idiothetic cues are essential for the generation of head direction cells and angular head velocity cells, neurons responsive to a preferred heading direction or head rotation speed respectively (Bassett & Taube, 2001; Butler et al., 2017; J. S. Taube et al., 1990a; Jeffrey S. Taube & Bassett, 2003). Head direction cells were first discovered in the post-subiculum, and have been since found in many more upstream cortical and subcortical brain regions (Cho & Sharp, 2001; Dudchenko et al., 2019; Mehlman et al., 2019; Ranck, 1984; Taube et al., 1990a; Taube, 1995). Head direction encoding is thought to be supported and stabilized by angular head velocity signals. This relationship is bidirectional, where AHV signals can be derived from HD inputs, and HD can be re-computed from AHV (Blair & Sharp, 1995; Brennan et al., 2021; Clark & Taube, 2012).

The hippocampus is known to be necessary for generating a cognitive map of an environment (Moser et al., 2017). Hippocampal theta oscillations are essential for the tuning of some navigational cell types such as entorhinal grid cells and hippocampal place cells, but the contributions to head direction (HD) cells and angular head velocity (AHV) cells are currently unclear, where theta may contribute in direct and indirect ways (Buzsáki, 2005; Hafting et al.,

2005; Koenig et al., 2011; O'Keefe et al., 1971; Pastor et al., 2020; Tsanov et al., 2011). The

direct causal relationship of hippocampal theta and HD cells has been investigated in the anterior

thalamus and medial entorhinal cortex (Brandon et al., 2011; Koenig et al., 2011; Pastor et al.,

2020). These studies inactivated the medial septum (MS), where the cholinergic inputs are major

contributors to the hippocampal theta rhythm (Buzsaki, 2002). MS inactivations reduced HD

tuning only in darkness, when visual input cannot be used for path integration (Pastor et al.,

2020). Furthermore, stimulation of vestibular nuclei, which are the primary source of self-motion

cues, can induce and modulate hippocampal theta rhythms (Aitken et al., 2018).

1.2.2 Reward

With its connections with the mesolimbic reward circuitry, the hippocampus and its

subregions are essential for learning the associations between reward and behavior (LeGates et

al., 2018; Lisman & Grace, 2005; Salgado & Kaplitt, 2015; Sosa et al., 2020; Trouche et al.,

2019). The nucleus accumbens (NAcc), ventral pallidum (VP), and ventral tegmental area (VTA)

are major components of the mesolimbic reward pathway (Berridge & Kringelbach, 2015;

Morales & Margolis, 2017; Root et al., 2015; Salgado & Kaplitt, 2015) and are well connected

with the hippocampus through direct and indirect pathways (Lisman & Grace, 2005; Oades &

Halliday, 1987). The hippocampus receives direct projections from the VTA and sends direct

projections to the NAcc (Lisman & Grace, 2005; Trouche et al., 2019). Conversely, the

hippocampus also indirectly innervates the VTA via projections to the lateral septum and NAcc

(Lisman & Grace, 2005; Trouche et al., 2019; van der Meer et al., 2014). These connections

between the hippocampus and mesolimbic reward circuit are critical for learning the spatial

representation of reward (Salgado & Kaplitt, 2015; Sosa et al., 2020; Trouche et al., 2019)

5

The nucleus accumbens is a major component of the ventral striatum, and is an essential region for the acquisition and processing of motivational stimuli (Mogenson & Nielsen, 1984; Salgado & Kaplitt, 2015). The ventral striatum receives direct innervations from the ventral subiculum (Floresco et al., 2001; Groenewegen et al., 1987) which coordinate memory consolidation of spatial information (Torromino et al., 2019). Furthermore, the ventral striatum is responsive during hippocampal sharp wave ripples (Pennartz, 2004). The ventral pallidum (VP) is a primary target of the NAcc (Root et al., 2015). An estimated 50-80% of dopamine receptor 1 and 2 (D1R & D2R)-expressing GABAergic medium spiny neurons (MSNs) in the NAcc project to the dorsal ventral pallidum (VP) (Kupchik et al., 2015). Conversely, the VP also sends many GABAergic projections back to the NAcc (Root et al., 2015; Vachez et al., 2021). The VP also receives major dopaminergic afferents from the ventral tegmental area (VTA), with 30-60% of VTA dopamine neurons projecting to the VP (Klitenick et al., 1992; Maslowski-Cobuzzi & Napier, 1994). Therefore, the VP and NAcc are part of an integrated network that mediates motivational salience and contributes to navigation and motor activity. While the functional connectivity between the NAcc and hippocampus is well defined, there has been less work done on the relationship between the VP and hippocampus since there are no known direct innervations (Root et al., 2015).

1.2.3 Sleep

Sleep is an essential physiological state in all known mammals (Eban-Rothschild et al., 2017; Siegel, 2008), which can be easily decoded by oscillatory patterns in the hippocampus. Awake states are characterized by desynchronized slow wave activity during quiet wakefulness, but during motivated behaviors theta and gamma oscillations are prevalent (Buzsaki, 2002; Colgin, 2013; Montgomery et al., 2008). Sleep states are defined by two distinct phases in

mammals – rapid eye movement (REM) and slow wave non-REM (NREM) sleep. Throughout

the sleep cycle, the mammals transition from awake, NREM, REM, then briefly back to awake

before returning to NREM (Aserinsky & Kleitman, 1953; Eban-Rothschild et al., 2017;

Scammell et al., 2017; Van Twyver, 1969). NREM sleep is defined by slow synchronized waves,

sleep spindles, and hippocampal SWR events (Buzsáki, 2015; De Gennaro & Ferrara, 2003).

REM sleep displays neural oscillation patterns similar to active states with the presence of strong

theta rhythms, and recently with evidence of high frequency oscillations named "splines" in the

retrosplenial cortex (Ghosh et al., 2022; Lee et al., 2005; Xu et al., 2015). Indeed, sleep states

can be identified with >90% accuracy using various types of machine learning classifiers

(Alickovic & Subasi, 2018; Bresch et al., 2018; Sors et al., 2018; Zhang et al., 2020).

1.3 Epilepsy
The hippocampus is involved in temporal lobe epilepsy, a neurological disorder

characterized by seizures which often lead to cognitive deficits, affecting nearly 1% of the

population (Devinsky et al., 2018; G. Huberfeld et al., 2015). Epileptic seizures may manifest in

many ways, depending on whether the onset zone is focal or generalized (Devinsky et al., 2018).

In temporal lobe epilepsy, a variant of focal epilepsy, high frequency oscillations have been

identified as a biomarker, where hippocampal sharp wave ripples manifest instead as

pathological interictal fast ripples (250-500 Hz) (Buzsáki, 2015; Cimbalnik et al., 2018; Jirsch et

al., 2006; Worrell et al., 2004).

Sodium channel gene mutations associated with epileptic encephalopathy are *SCN1A*,

SCN2A, *SCN3A*, and *SCN8A* (Meisler et al., 2021). The *SCN8A gene* mutation, affecting Nav1.6

sodium channels, and its role in epilepsy was first described in 2012 in humans, with

approximately 2% of all epileptic encephalopathies being due to *SCN8A* mutations (Meisler,

2019; Veeramah et al., 2012). The *SCN8A* pathogenic mechanism primarily causes epilepsy via gain of function (GOF) $Na_v1.6$ mutations which are thought to lead to hyperexcitability (Meisler et al., 2016). A smaller fraction of *SCN8A* related epilepsies are due to LOF mutations (Blanchard et al., 2015), and alterations in sleep architecture have been observed in the preclinical $Scn8a^{med-jo/+}$ LOF mouse model (Papale et al., 2010). Here, we focus on a GOF mouse model that has been shown to involve hippocampal hyperexcitability (Lopez-Santiago et al., 2017) and investigate how this relates to changes in sleep and hippocampal ripples.

1.4 Conclusions

This thesis examines the contributions of the hippocampus in circuits relating to navigation, reward, and epilepsy. In Chapter 2 we report angular head velocity cells in the NAcc and VP. This encoding is limited to task-free conditions, and is overridden by reward encoding during the task. Further investigations revealed that head velocity encoding was also abolished by periods of high hippocampal theta rhythms, which are known to be associated with motivated and active states. As a secondary analysis to Chapter 2, in Chapter 3, we assessed the relationship of hippocampal sharp wave ripples (SWR) and single neuron response in the nucleus accumbens (NAcc) and ventral pallidum (VP). We report a novel multi-timescale response of NAcc and VP neurons during hippocampal SWRs after animals perform a task. We show that neurons which were responsive during the task are more likely to exhibit a multi-timescale response to SWRs outside of the task environment. Furthermore, we report that individual differences of animals during the task can be dissociated by the properties of hippocampal SWRs. Lastly, using continuous 24/7 electrophysiological recordings, Chapter 4 investigates how hippocampal SWRs may systematically change in a GOF preclinical model of *SCN8A* encephalopathy. Chapter 5 details the software developments necessary for this dissertation.

Chapter 2: Angular Head Velocity Cells in the Nucleus Accumbens and Ventral Pallidum Revealed by State-Dependent Behavior

Danny Siu[*], Allison M. Ahrens[*], & Omar J. Ahmed

2.1 Abstract

Successful encoding of both orientation and reward-related information is critical for evolutionary survival. The nucleus accumbens (NAcc) and ventral pallidum (VP) are integral parts of the reward processing network but are thought to lack neurons computing elemental orientation information. Here, contrary to current assumptions, we show that more than a third of neurons in both the NAcc and VP robustly encode angular head velocity (AHV), while some NAcc neurons also encode the animal's head direction. Tracking neurons before, during, and after a reward-related task reveals that pre- and post-task AHV encoding is selectively lost during the task and replaced by cue and reward encoding. This switch is brain-state dependent: increased hippocampal theta rhythms seen during motivated brain states predict the loss of AHV encoding. Thus, NAcc and VP neurons can precisely track head rotations, potentially helping to orient an animal before transitioning to support the motivated acquisition of reward.

2.2   Introduction

Spatial navigation and reward acquisition are essential for mammalian survival. Successful

navigation is thought to be partially supported by path integration, a strategy to estimate one's

current position using self-motion cues (Alexander et al., 2022; Etienne & Jeffery, 2004;

McNaughton et al., 1991; Olson et al., 2017; Séguinot et al., 1993; Sheeran & Ahmed, 2020),

including the precise direction and velocity of head movements (Butler et al., 2017; Valerio &

Taube, 2012). Head direction (HD) cells are neurons that preferentially fire when an animal is

oriented towards a specific direction (Taube, 1998, 2007). First discovered in the post-subiculum

(Ranck, 1984; Taube et al., 1990a, 1990b), HD cells have since been observed in many other

subcortical and cortical brain regions (Cho et al., 2001; Dudchenko et al., 2019; Jacob et al.,

2017; Mehlman, et al., 2019; Taube, 2007). Importantly, HD encoding is known to be supported

and stabilized by angular head velocity (AHV) signals (Blair & Sharp, 1995; Clark & Taube,

2012). AHV information primarily originates from the vestibular nuclei (Brown et al., 2005;

Clark & Taube, 2012), but other factors including visual stimuli also improve AHV encoding

fidelity (Keshavarzi et al., 2022; Mehlman et al., 2019). AHV information can also be re-

computed from HD inputs (Brennan et al., 2021). The precise representation of AHV may help

neural circuits perform precise orientation-related computations that can guide diverse behaviors.

AHV-encoding cells have been found in several regions including the dorsal tegmental

nucleus, lateral mammillary nucleus, and retrosplenial cortex, all components of the ascending

pathway leading from vestibular nuclei to the cortex (Bassett & Taube, 2001; Keshavarzi et al.,

2022; Sharp et al., 2001; Stackman & Taube, 1998). In contrast, little to no AHV encoding has

been reported to date in the nucleus accumbens (NAcc) (McGinty et al., 2013). The NAcc is

primarily known as a mediator of reward and motivation (Ikemoto & Panksepp, 1999; Mogenson

10

et al., 1980), but it is also important for spatial learning (Rinaldi et al., 2012). Indeed, disruption of NAcc activity causes impairments in performance of both reward and spatially relevant tasks (Annett et al., 1989; Chang & Holland, 2013; Ito et al., 2008; Jongen-Rêlo et al., 2003; Parkinson et al., 1999). Through connections with the hippocampal formation, the NAcc plays an important role in the consolidation and retrieval of memories, linking rewarding events with contextual information in the environment (Lansink et al., 2009; Rinaldi et al., 2012; Trouche et al., 2019).

One of the primary output projections from the NAcc is to the ventral pallidum (VP) (Kupchik et al., 2015; Root et al., 2015; Salgado & Kaplitt, 2015; Vachez et al., 2021). As with the NAcc, there is no evidence of AHV encoding in the VP (Lederman et al., 2021). The VP projects to regions controlling motor activity, and is therefore well positioned to translate motivational signals into action (Root et al., 2015; Smith et al., 2009). Furthermore, the NAcc and VP receive major dopaminergic afferents from the ventral tegmental area (VTA), forming the mesolimbic dopamine pathway that is essential for learning and motivation (Berridge & Kringelbach, 2015; Klitenick et al., 1992; Maslowski-Cobuzzi & Napier, 1994). Therefore, the VP and NAcc are part of an integrated network that mediates motivational salience and contributes to navigation and motor activity but are currently thought to lack neurons computing elemental angular velocity and orientation information that may support their navigational and motor functions.

Here, by recording from a large number of NAcc and VP neurons, we find robust encoding of AHV by a third of all neurons in both the NAcc and VP, as well as the presence of HD cells in the NAcc. Importantly, this encoding of AHV is brain-state-dependent and is almost completely

11

overridden during a reward-related task, explaining why previous studies – examining activity during reward tasks – have noted no AHV encoding in the NAcc and VP (Lederman et al., 2021; McGinty et al., 2013). We show that an increase in the hippocampal theta-to-delta power ratio – a marker of activated/motivated brain states (Arduini & Green, 1954; Buzsaki, 2002; Colgin, 2013, 2016; Vanderwolf, 1969; Whishaw & Vanderwolf, 1973) – strongly predicts the transition of NAcc and VP cells from robust pre-task AHV encoding to task-related cue and reward encoding. Our results emphasize the fact that neurons in these regions have access to both navigational and motivational information and highlight a state-dependent switch between orientation and reward coding in the NAcc and VP.

2.3   Methods

2.3.1   Animals and surgery

We used 6 male Sprague Dawley rats weighing 300-400g (Charles River; Colony P04). Rats were singly housed in a reverse 12:12-h light/dark cycle with food and water available ad-libitum. All procedures were approved by the University of Michigan Committee on the Use of Care of Animals.

Animals were chronically implanted with electrode microdrives containing 14 independently movable tetrodes which were connected to a 64-channel electrode interface board (EIB-36-16TT, Neuralynx), targeting the nucleus accumbens (NAcc), ventral pallidum (VP), and hippocampus (HPC). Rats were anesthetized with isoflurane (4% induction, 1.5-2% maintenance), and the incision site was treated with lidocaine. A 2x8 mm craniotomy was made unilaterally to allow all tetrodes to enter the brain. After the dura matter was carefully removed, the top of the brain was covered with bio-compatible Kwik-Sil gel. The microdrive was secured with bone screws and dental cement. To serve as a ground, a bone screw was connected to the EIB with a soldered wire. For the following two days, rats were treated with enrofloxacin (8 mg/kg) and carprofen (5 mg/kg). Animals were allowed to recover for one week, during which tetrodes were lowered 0.5-1 mm per day until target sites were reached. Tetrodes in the NAcc and VP were lowered everyday by 40-330 µM before each session to record different cells each day. Hippocampal tetrodes targeting the CA1 were lowered until sharp wave ripples (SWR) were observed, then the tetrodes were left stationary for the rest of the sessions. At the end of the experiment, current was passed through the tetrodes to create electrolytic lesions and Nissl staining was performed to verify tetrode locations. Only cells with high confidence of hitting the target regions were included.

2.3.2 Electrophysiological recordings

Neural data were acquired continuously at 32 kHz with the Neuralynx data acquisition system (Neuralynx, Inc,MT). During 25-30 min pre-task and post-task periods, recordings were obtained while the animal freely roamed in a circular enclosure (30 cm diameter, 15 cm high). During the 40-45 min task period, the animal was transferred to a custom operant chamber (30 x 27.5 x 30 cm) containing a retractable lever and food dish, where it performed the Pavlovian conditioned approach (PCA) task (Flagel et al., 2009). The tetrode microdrive remained connected and recordings continued during the transfer of the animal from one apparatus to the other. The PCA task consisted of 25 trials in which a retractable lever (the conditioned stimulus) is extended into the cage for 8 s, then retracted and immediately followed by the delivery of food reward (banana flavored pellets; BioServ, #F0059). Trials were separated by inter-trial intervals (ITI) of 90-150s.

Single unit activity was sorted with Offline Sorter (Plexon). Waveform features such as trough to peak width, amplitude, and the first two principal components from principal component analysis were used to ensure unit isolation. A total of 501 NAcc and 345 VP single units were recorded. In HD and AHV analyses, cells with >0.5Hz during the pre-task period were included (N=282 NAcc; N=246 VP). To make comparisons of AHV encoding across various conditions (pre-task, within-task, post-task, ITI, quartiles), we utilized the same cells identified in the pre-task AHV group.

2.3.3 Video data acquisition

Video recordings of the session were obtained at 30Hz using overhead cameras. The x and y coordinates of the left and right LED were tracked and positional information was further processed with DeepLabCut, a markerless pose-estimation software utilizing deep learning

(Mathis et al., 2018). . Each video frame contained a timestamp in microseconds, allowing precise alignment of position and neural activity. Head direction was calculated from the relative positions of the two LEDs, and angular head velocity was determined by changes in head direction over time.

2.3.4   PCA Task analyses

Single unit analyses were performed in MATLAB and Neuroexplorer (Nex Technologies). Neural activity was assessed in periods 8 s before lever extension (pre-CS), 8 s after the illuminated lever cue extended (task period), and 8 s after reward delivery. Cue onset was defined as 0 s when the illuminated lever cue extended. Reward delivery was defined as the simultaneous lever retraction and pellet delivery in the magazine port. For task analysis, firing rate was determined via peristimulus time histograms (PSTH) by calculating the average number of spike times generated in 100 ms bins divided by the bin size to obtain spikes per second. Entire session assessments were generated in 5 s bins. Changes in firing rate during the task period were compared with the pre-CS baseline for each unit. For comparisons of angular head velocity cells in task conditions, the within-task period was defined as 14 seconds after the cue onset period (0s to 14s) and the ITI was defined as a duration-matched 14s period before the cue onset (-16s to -2s).

To determine the magnitude of task-triggered firing, each unit firing rate was Z-score normalized to the task-triggered baseline (-5 s to 0 s). Task modulations were determined by the magnitude and direction of a cell's cue-evoked activity after lever presentation from 0 s to 0.4 s (CS Onset), 1 s to 8 s (CS Period), 8 s to 8.4 s (CS Offset), and 8.6 s to 9.6 s (US). For CS onset, CS offset, and US, upmodulations were categorized as cue-evoked activity $\geq$ +1.3 Z-score while downmodulations were cue-evoked activity $\leq$ -1.3 Z-score. During the CS period, upmodulations

15

and downmodulations were defined as +/-1.0 Z-score respectively. Otherwise, a cell was considered non-modulated by the task. To examine the proportion of neurons responsive to the PCA task in each of the 4 task periods, we conducted pairwise χ^2 tests comparing the NAcc and VP upmodulation and downmodulations.

2.3.5 **Head direction detection**

To determine a head direction (HD) cell's tuning curve, the animal's head direction was recorded as the momentary head direction value for each spike. The momentary head direction for each spike and recorded head directions per session were then binned from 0° to 360° in 6° bins. The tuning curves were generated for each spike by dividing the binned spike head directions by all binned visited head directions in the session. The resulting tuning curves were smoothed with a gaussian kernel of 3 bins. Preferred firing directions (PFD) were determined by the mean direction of each head direction tuning curve via circular statistics. For the tuning widths, we identified values half of the peak firing rate to the left and right of the PFD. The directional information content value was also calculated for each HD cell in bits per spike, with detailed methods in Skaggs et al. (Skaggs et al. 1993). The information content per spike represents the predictive strength of cell firing to animal head direction (Skaggs et al. 1993).

The Rayleigh R was computed for each session as a measure of the directional tuning strength. To determine whether a cell displayed significant PFD, we used bootstrapped statistics on the computed Rayleigh R's for 1000 shuffles. To create the shuffled distribution, inter-spike intervals (ISIs) were shuffled, head direction encoding was calculated, and the Rayleigh value was computed for each shuffled outcome. If the Rayleigh value was greater than 99% of the shuffled distribution, > 0.3 Rayleigh R, > 3 fold firing rate change from PFD to baseline, and >

16

0.5 Hz baseline HD firing rate, the cell was identified to have significant HD tuning.

Comparisons of HD proportions were performed with χ^2 tests.

2.3.6 Clockwise vs Counterclockwise (CW vs CCW) analyses

The angular head velocity (AHV) was calculated as the difference in head degrees per second. Similar to estimating HD spike tuning curves, the nearest recorded AHV value was found for each spike. The momentary AHV for each spike and recorded AHV per session were then binned by 6 °/s from -200 °/s to 200 °/s. Bins with less than 15 samples per °/s were excluded. The tuning curves were calculated by dividing the binned spike AHV by all binned AHV in the session, and we applied a 4-bin gaussian kernel smoothing window to the resulting AHV versus spike rate vector. Head direction measurements were separated into clockwise (CW) and counterclockwise (CCW) conditions. CW conditions were denoted as angular head velocities > + 45 °/sec, and CCW conditions occurred when samples were < - 45 °/sec. With these limitations in place, the head is required to move at least 45 °/sec to be considered turning. PFD was recalculated individually for the CW and CCW conditions.

2.3.7 Angular Head Velocity Cell Classification

To classify AHV cells, we calculated the AHV score based on the Pearson correlation between unsigned AHV and firing rate. We performed shuffling statistics, where we shuffled ISIs and recalculated the AHV tuning curve for 1000 iterations. AHV cells were considered significant in either CW or CCW directions when the following criteria were met: 1) AHV scores were greater than 0.5 from unsigned 0 to 200 °/s, 2) the slope from unsigned 0 to 200 °/s was greater than 0.001 spikes per degree, and 3) the cell's AHV score and slope were greater than 99% of the shuffled distribution for CW or less than 1% for CCW. We further categorized AHV cells into symmetric and asymmetric cells. Symmetric cells require both CW and CCW to

be significant. Asymmetric cells require either CW or CCW to be significant, and the opposing side is either significant in the opposite sign or is not significant. Comparisons of AHV proportions across conditions were performed with 5-way χ^2 tests.

Linear relationships of AHV and firing rate were found up to 200 °/s and for most high firing rate cells, continued up to 400 °/s. Due to our smaller recording apparatus, there was difficulty in obtaining sufficient samples for some cells, leading to instability in the AHV relationship. Thus, we proceeded with AHV analyses up to 200 °/s.

2.3.8   Hippocampal rhythm analyses

To determine whether AHV cells were modulated by hippocampal oscillations, we isolated epochs based on the relative delta power (0.5Hz), relative theta power (6-9Hz), and theta-delta ratio (theta/delta) extracted from the local field potential (LFP). We performed the multi-taper analysis with 2s windows and taper of 1 using the chronux toolbox (https://chronux.org/) to acquire the power spectrums from 0.5-20Hz. We calculated the relative power of each 2s window by normalizing each window to the total power from 0.5-20Hz. We performed quartile analyses by finding thresholds for the 25th percentiles of each session and allocating the 2s epochs into each of the four equally distributed groups. This strategy ensured that each group contained an equivalent amount of time for firing rate, occupancy, and AHV related analyses. Some data exploration was performed with the gramm plotting package (Morel, 2018).

To assess the relationship of hippocampal theta rhythms and angular head velocity at a higher time resolution, we extracted individual theta cycles. We filtered the LFP from 6-40Hz and detected the local maxima and minima of each theta cycle. We then calculated the properties

18

of each theta cycle including the peak to trough amplitude, duration, and asymmetry based on instantaneous skewness.

2.3.9   Angular Head Velocity Depth of Modulation

To determine the tuning strength of AHV cells, we calculated the depth of modulation (DoM). The modulation depth is the symmetrized percent change from the baseline (0 °/s) to the peak (± 200 °/s) of each cell. Due to our minimum criteria of 15 samples per °/s, some cells did not have values at ± 200 °/s. Thus, we estimated the firing rate at ± 200 °/s using the slope from the line of best fit between AHV and firing rate. We also calculated the unsigned preferred DoM of each cell by identifying the turn direction with greater DoM.

$$100 \times \frac{(FR_{peak} - FR_{baseline})}{(FR_{peak} + FR_{baseline})}$$

(1)

2.3.10   Spatial and Temporal Invariance Analyses

To assess the spatial robustness of the HD and AHV cells, we partitioned the animal's recording chamber into two halves. The HD and AHV tuning curves were generated individually for both halves and assessed for similarity. To check the temporal stability of HD and AHV cells, we compared the HD and AHV tuning curves between pre-task and post-task epochs of the entire session. The task requires at least 30 minutes to complete, therefore pre-task and post-task epochs are temporally separated by a minimum of 30 minutes. We calculated the HD and AHV tuning curves for both epochs individually and assessed for similarity.

2.3.11   Statistics

Statistical procedures were performed with R (version 4.0.3) and MATLAB (2019b), and results were considered significant for $p \leq 0.05$. Circular statistics were carried out with the CircStat toolbox on the Mathworks File Exchange (Berens, 2009).

19

2.4   Results

2.4.1   Robust Encoding of Angular Head Velocity in Both NAcc and VP

We recorded the activity of NAcc and VP neurons during three epochs per session: pre-task, within-task, and post-task. We first looked for evidence of head direction and angular head velocity encoding during the pre-task phase. A total of 282 NAcc and 246 VP single units from 6 rats were recorded and analyzed (**Figure 2.1A**). In the NAcc, 7.8% (22/282) of single units displayed significantly higher firing rates when facing a specific preferred direction and were therefore classified as HD cells (**Figure S2.1A, Table S2.1**). In the VP, however, fewer HD cells were found—only 3.3% (8/246) of the VP single units analyzed met the criteria for HD classification (**Figure S2.1C, Table S2.1).**

We next examined whether NAcc and VP neurons encoded angular head velocity (AHV). A substantial proportion of NAcc (106/282, 37.6%) and VP (79/246, 32.1%) cells encoded AHV during the pre-task period (**Figure 2.1**). We analyzed the clockwise (CW) versus counterclockwise (CCW) preferences of these cells and found that most AHV cells increased their firing rates with increasing velocities in both the CW and CCW directions. These cells were defined as symmetric positive cells (symPos; **Figures 2.1B and 2.1I**). Others decreased their firing rates during both CW and CCW rotations and were defined as symmetric negative cells (symNeg; **Figures 2.1C and 2.1J**). AHV cells which only responded to one direction were defined as asymmetric cells, either CW preferring (asymCW; **Figures 2.1D and 2.1K**) or CCW preferring (asymCCW; **Figures 2.1E and 2.1L**). Cells which did not meet the criteria for angular velocity encoding in either CW or CCW direction were defined as unmodulated.

Both NAcc and VP AHV populations displayed a preference towards increased firing rates in both CCW and CW directions (**Figures 2.1F and 2.1M).** Indeed, there was a preference

for symPos cells in both the NAcc and VP regions compared to the other subtypes defined here (**Figures 2.1G and 2.1N):** symPos cells significantly outnumbered symNeg cells in the NAcc (χ^2 (1,N=564)=31.69, p=1.8e-8) and in the VP (χ^2(1,N=492)=9.19, p=0.0024). Furthermore, when we assessed differences between the NAcc and VP, we found similar proportions of AHV cells (χ^2(4,N=528)=6.59, p=0.159). Half of all NAcc HD cells (11/22, 50%) also encoded AHV and hence were conjunctive HD-AHV cells (**Figure S2.2**). AHV encoding was not more likely in HD vs non-HD cells, with no significant difference in AHV encoding between the two populations (HD: 50%; non-HD: 37.6%; χ^2(4, 304)=2.04, p=0.728).

To test whether the AHV encoding was independent of position, we divided the recording chamber into top and bottom halves and recalculated the tuning curves in each compartment (**Figure S2.3**). This analysis confirmed that the AHV tuning was independent of the precise position of the animal. We also assessed temporal stability of AHV encoding during pre-task and post-task epochs, where we found similar AHV proportions between these two periods (**Figure S2.4;** NAcc: χ^2(4,N=564)=2.13, p=0.712; VP: χ^2(4,N=492)=3.91, p=0.418). Similarly, we found spatial and temporal stability within the HD cells (**Figures S2.3 and S2.4**). Overall, these controls confirmed both spatial and temporal stability of the preferred HD during task-free epochs.
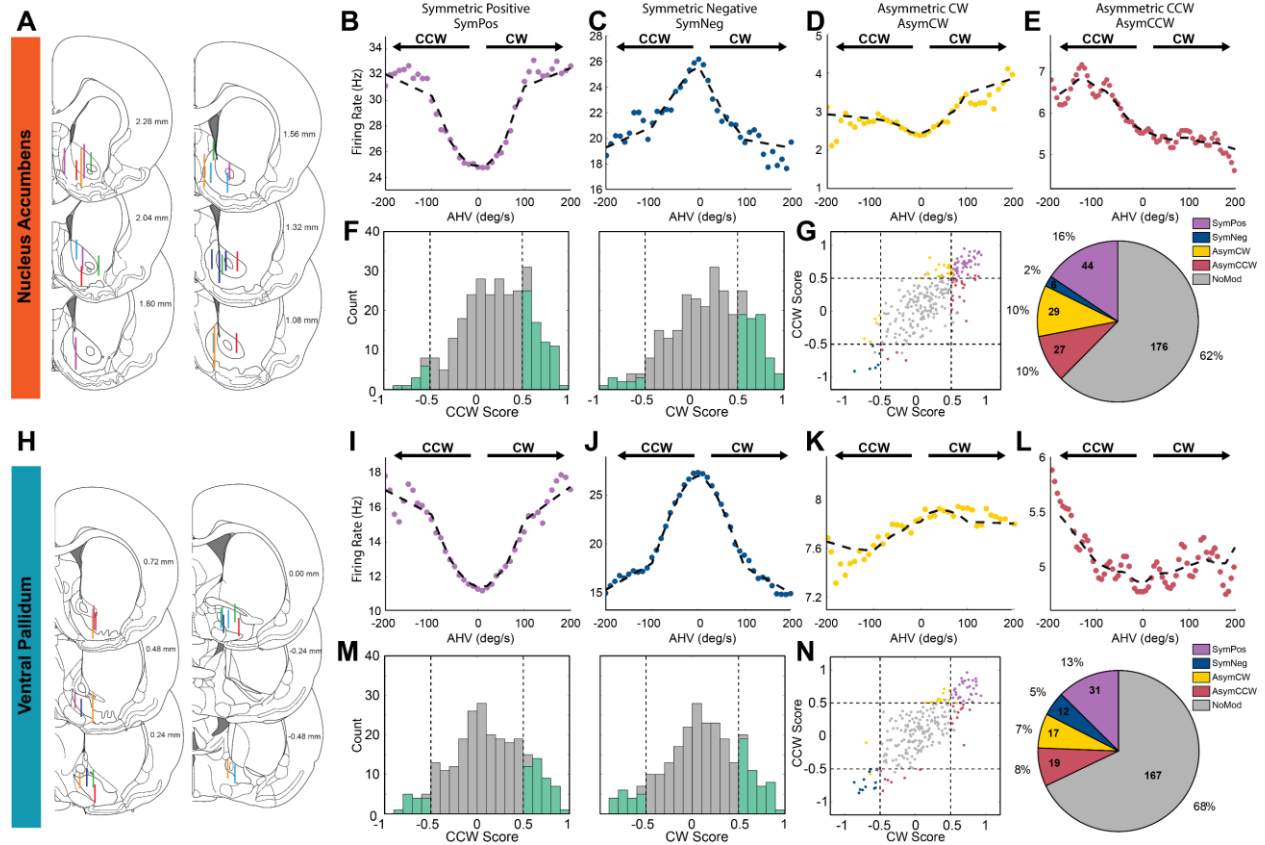
Figure 2.1: Angular head velocity cells in the nucleus accumbens and ventral pallidum
A) Individual recording locations of tetrodes in the nucleus accumbens and ventral pallidum. Implant locations are color-coded by each unique animal. **B-E)** Examples of NAcc AHV cells: **(B)** SymPos AHV cell, defined by increased firing rate at increasing AHV values in both directions. **(C)** SymNeg AHV cells, defined by decreasing firing rates at increasing AHV values in both directions. **(D&E)** AsymCW and asymCCW AHV cells, defined by greater firing rates in the CW and CCW directions, respectively. **F)** Counterclockwise (Left) and clockwise (Right) AHV scores (the Pearson correlation of AHV and firing rate). Vertical dotted lines indicate the correlation threshold at ±0.5. Green bars are designated as AHV cells that met all three test criteria (correlation, slope, shuffling test), while gray bars did not pass these requirements. **G)** (Left) Relationship of CW and CCW AHV scores. Dotted lines represent the correlation thresholds. The dots are color-coded according to the 5 AHV subtype classifications. Some cells are non-significant or asymmetric despite crossing the correlation threshold due to not meeting the shuffling test criteria. (Right) Pie chart for NAcc AHV cells (n=282) indicating the proportion of each AHV subtype among all analyzed single units with the sample sizes and percentages in each category. **I-N)** Similar to the NAcc figures in **B-G** but for VP neurons (n=246).

2.4.2 Angular Head Velocity Encoding in the NAcc and VP is Lost During Reward-Related Task Performance

The NAcc and VP are heavily involved in cued motivation and reinforcement, so we examined whether AHV encoding persisted during the performance of a Pavlovian conditioned approach (PCA) task that is known to engage a sizable proportion of NAcc and VP cells (Ahrens et al., 2018; Ahrens, Meyer, et al., 2016; Gillis & Morrison, 2019). For the PCA task period, animals were transferred (while recording continued) to an open-topped operant chamber with a retractable lever and a pellet delivery dish. During a 30-45 min session, the animal was presented with 25 pairings of a lever-extension conditioned stimulus (CS) and the response-independent delivery of a food pellet (unconditioned stimulus; US). We examined neural activity during the active portions of the task (within-task), when animals were either exposed to the lever cue (8 s) or were retrieving and consuming the pellet (6 s immediately following offset of the lever cue). Cells in both the NAcc and VP were responsive to the PCA task, with varying preference to the four phases (CS, onset, CS period, CS offset, and US) of the task (**Figures 2.2A and 2.2B**). While most cells displayed excitation to various phases of the PCA task, some were preferentially inhibited (**Figure S2.5**). Overall, the VP displayed a greater magnitude of CS-induced firing change than the NAcc during the CS onset, CS offset, and US periods (**Figure 2.2B; Figure S2.5**). This effect may be due to the greater proportion of downmodulated neurons in the VP with respect to the task (**Figure 2.2C**). Indeed, for cells that showed inhibition, the VP had a greater proportion than the NAcc in all of the four epochs (CS onset: $\chi^2(1,N=549)=20.6$, p=5.7e-6; CS period: $\chi^2(1,N=549)=8.56$, p=0.003; CS offset: $\chi^2(1,N=549)=6.52$, p=0.011; US: $\chi^2(1,N=549)=11.16$, p=8.35e-4). For cells that showed excitation, the VP had a greater proportion during CS offset and US epochs ($\chi^2(1,N=549)=5.36$ and 7.62, p=0.021 and 0.0058, respectively), but not CS onset and CS period (**Figure 2.2C**).

23

When we investigated how well pre-task AHV cells encoded AHV during the PCA task, we found that most of the cells temporarily displayed dramatically reduced AHV encoding (**Figure 2.2D**). Instead, these same cells displayed task related firing to reward and cues (**Figures 2.2D and 2.2E**). We found a significant increase in baseline (0 deg/s) firing rate during the PCA task (Wilcoxon signed rank test; p=0.0084 and p=1.01e-6 pre-task compared to within-task for NAcc and VP respectively; **Figure 2.2F and 2.2J**) as well as a significant decline in AHV detections for both NAcc and VP compared to the pre-task period (NAcc: $\chi^2(4,N=564)=88.55$, p<1e-16; VP: $\chi^2(4,N=492)=60.42$, p=2.37e-12); **Figure 2.2G and 2.2K**). This effect was only uniquely present during the task period, as AHV encoding and baseline (0 deg/s, no head rotation) firing rates recovered during the post-task period (NAcc: 34.0%; VP: 34.5% AHV cells). For example, when we tracked individual cell response through the three pre-task, within-task, and post-task periods, individual cells displayed temporarily elevated firing rates and reduced AHV encoding only during the task (**Figures 2.2D and 2.2E**); during the post-task period, these same cells returned to pre-task AHV encoding and baseline firing rates. Indeed, post-task AHV encoding proportions (**Figure S4**) and baseline firing rates were not significantly different from pre-task periods (Wilcoxon signed rank test; p=0.36 and p=0.39 for NAcc and VP respectively; **Figure 2.2F and 2.2J**), confirming that task performance only temporarily reduces AHV encoding.

Furthermore, this result also occurred as the animals waited for the next trial to begin and was not due to under sampling of high angular velocities. We validated this result in two additional ways: (1) detection of AHV cells during the inter-trial intervals (ITI) and (2) analyses of AHV cells limited to ±80 deg/s. Analyses (1) and (2) both led to similar results, where (1) pre-task encoding was significantly greater than during the ITI periods for both the NAcc

(χ^2(4,N=564)=59.4, p=3.88e-12) and VP (χ^2(4,N=492)=57.32, p=1.06e-11), and where (2) angular-velocity delimited pre-task yielded significantly more AHV cells than the task for both the NAcc (χ^2(4,N=564)=65.74, p=1.80e-13) and VP (χ^2(4,N=492)=44.25, p=5.70e-9; **Figure S2.6**). Overall, we found that the reward-related task dramatically reduced angular head velocity encoding in the NAcc and VP, transitioning instead to the cue- and reward-related encoding traditionally associated with neurons in these regions.
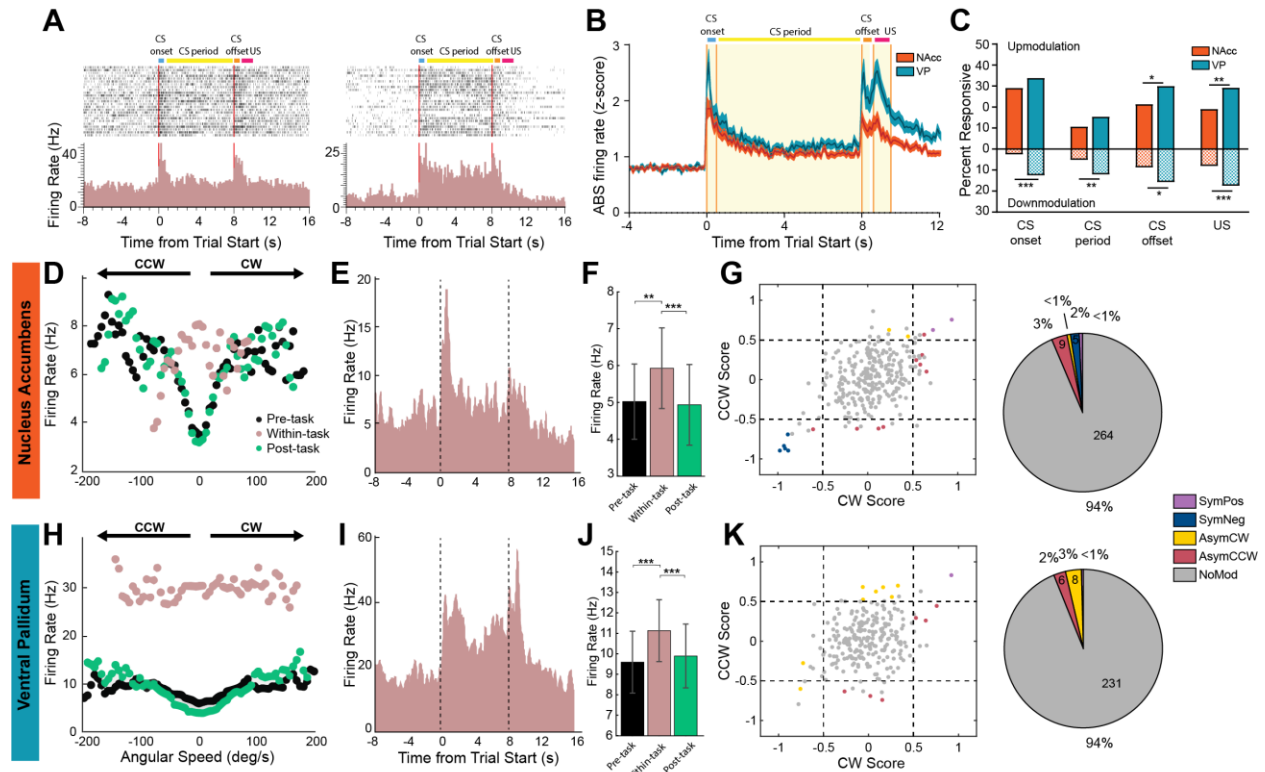
Figure 2.2: Task performance dramatically reduces detection of angular head velocity cells.
A) Examples of responsive cells during the PCA task. Response patterns included combinations of four distinct epochs (CS onset, CS period, CS offset, US), in either up-modulated or down-modulated directions. **B)** Overall, the average activity of all cells (with all change from baseline shown as positive) is greater for VP than NAcc for CS onset, CS offset, and US epochs. **C)** The VP had a greater percentage of cue-responsive cells than the NAcc. The VP had more downmodulated units than the NAcc during all four trial epochs, and a greater percentage of upmodulated units during CS offset and US. **D)** Example of an NAcc AHV cell during the pre-task, post-task, and within-task epochs. **E)** Same example cell from example **D** during the within-task epoch. Firing rates are averaged across 25 trials of the PCA task where the lever is extended at 0s and the lever retracts at 8s. The within-task period was defined as 14 seconds after the cue onset period (0s to 14s). **F)** Baseline AHV firing rate (0 deg/s) for pre-task, post-task, and within-task populations in the NAcc (top) and VP (bottom). Firing rates do not differ between pre-task and post-task periods, but within-task periods are significantly greater than pre-task and post-task in both the NAcc and VP (NAcc: p=0.0084 and p=2.52e-4 for pre-task and post-task respectively; VP: p=1.01e-6 and p=6.39e-6 for pre-task and post-task respectively; Wilcoxon signed rank test). **G)** (left) Relationship of CW and CCW scores, where each point represents a cell. Dotted lines indicate the correlation threshold (r=0.5) and colors indicate the AHV subtype classification. (right) Pie charts indicating the proportion of AHV subtypes during the within-task period for the nucleus accumbens and ventral pallidum. **H-K)** Similar to the NAcc figures in **D-G** but instead in the VP. A total of 6.4% NAcc units and 6.1% of VP units encoded AHV while performing the task. This proportion was significantly lower than the 37.6% of NAcc units and 32.1% of VP units that encoded AHV in the pre-task session. For all figures * p < .05, ** p < .01, *** p < .001

26

2.4.3 Angular Head Velocity Cells in the NAcc and VP are State-Dependent

We next examined the spectral differences that demarcate the pre- and post-task periods

with strong AHV encoding versus the task period with weak AHV encoding. To investigate this,

we utilized hippocampal local field potential (LFP) signals that were simultaneously recorded

together with the NAcc and VP units (**Figure S2.7A**). Active, motivated brain states are

associated with increased hippocampal theta and decreased hippocampal delta power, best

quantified by the ratio of theta (6-9 Hz) power to delta (0.5-4Hz) power (theta-delta ratio;

Arduini et al., 1954; Aronov et al., 2017; Buzsaki, 2002; Colgin, 2013, 2016; Vanderwolf, 1969;

Whishaw et al., 1973). We confirmed this in our data, where the within-task periods were

consistently identified by significantly higher theta-delta ratios (**Figures 2.3A and 2.3B;**

Wilcoxon signed rank test; p=1.74e-10 and p=1e-10 compared to pre-task and post-task

respectively).

To identify the relationship between hippocampal theta-delta ratio and NAcc & VP AHV

cells, we split the entire recording session (combining all of pre-task, within-task, ITI and post-

task) into four equal quartiles of increasing theta-delta ratio (see Methods). As expected, the task

period was more likely to contain epochs of high theta-delta ratio, whereas the pre-task and post-

task periods are dominated by epochs of low theta-delta ratio (**Figure 2.3D; Figures S2.7B and

S2-7C;** pre-task: $F_{(1,3)}$=142.70 p=9.87e-31; within-task: $F_{(1,3)}$=64.76, p=5.64e-14; post-task:

$F_{(1,3)}$=123.11, p=1.65e-26; Friedman test).

We then analyzed the firing rate and AHV encoding in each of these theta-delta ratio

quartiles. The average firing rate of cells in the NAcc and VP increased as a function of

increasing theta-delta ratio (**Figure 2.3E; Figures S2.7D and S2.7E**). Indeed, firing rates of cells

during the top quartile periods of high theta-delta ratio were greater than the bottom quartile

27

periods (Wilcoxon signed-rank test, NAcc: p=2.09e-15; VP: p=2.86e-9). Importantly, we found that theta-delta ratios reliably predicted AHV encoding in both the NAcc and VP, such that there were significantly more AHV cells identified during low theta-delta ratio states (NAcc: (χ^2(4,N=564)=33.54; p=9.25e-7; VP: χ^2(4,N=492)=47.70; p=1.09e-9; **Figure 2.3G**). Consistently, high delta power, low theta power, and low linear translational motion (typically correlated with lower theta-delta ratios; Buzsáki, 2005; McFarland et al., 1975) also individually predicted better AHV encoding. Notably, even minor increases in linear translational motion (>4cm/s) deteriorated the AHV encoding of NAcc and VP cells (NAcc: χ^2(4,N=564)=41.6; p=2.49e-8; VP: χ^2(4,N=492)=48.4; p=7.67e-10; **Figures S2.8-S2.10**). Lastly, to investigate the theta-AHV relationship on a more precise timescale, we extracted individual theta cycle amplitude and assessed this relationship with AHV **(Figures S2.11)**. While we have not yet quantitatively assessed this relationship, future work will more precisely determine how AHV encoding is affected by instantaneous theta states. Overall, we found that brain states with lower hippocampal theta rhythms (and higher hippocampal delta rhythms) are predictive of AHV encoding in the NAcc and VP, providing evidence for a brain-state dependent switch between AHV encoding versus cue/reward encoding in the mesolimbic reward pathway.
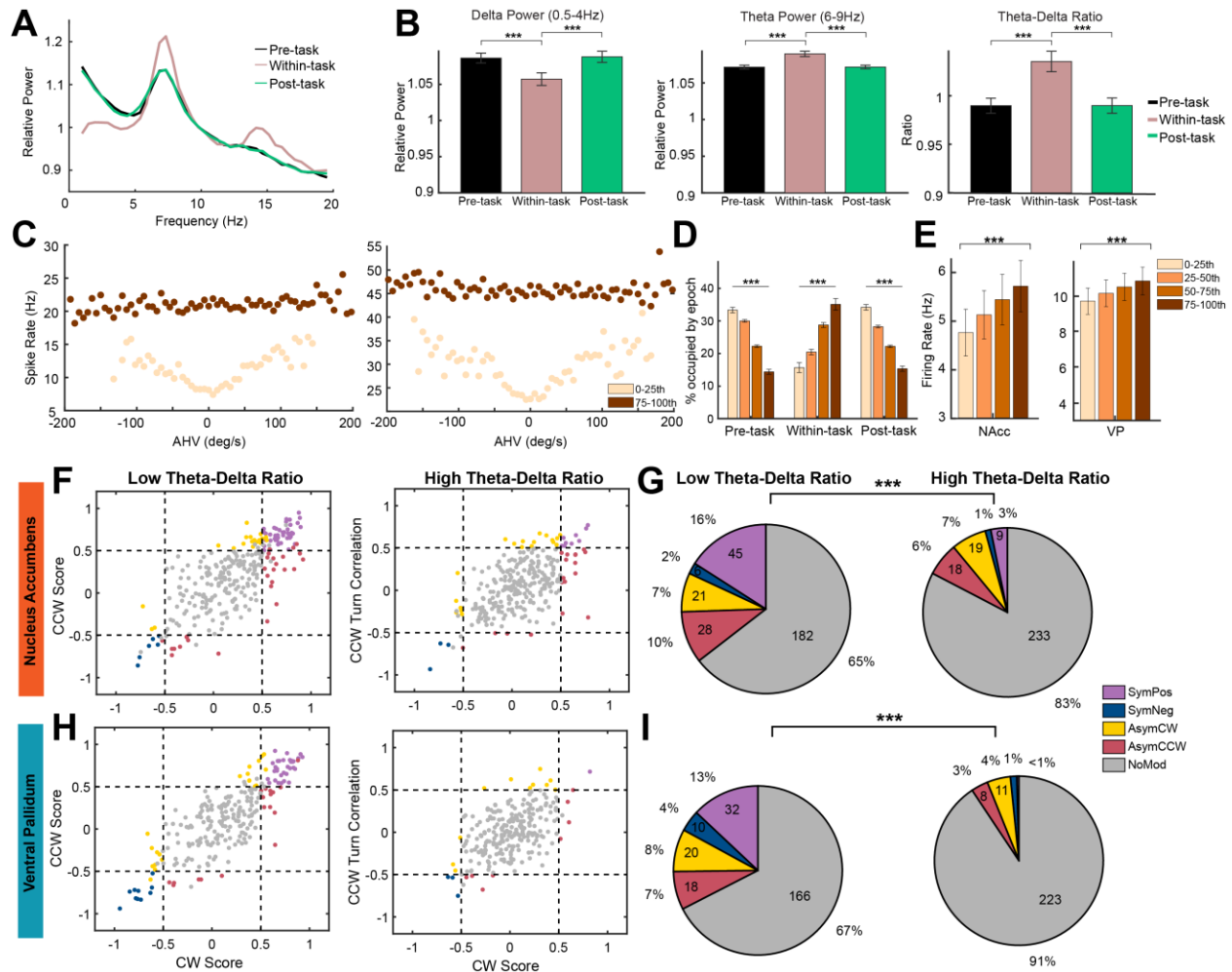
Figure 2.3: Brain state dependent encoding of angular head velocity in the NAcc and VP
A) Hippocampal power spectrum during pre-task, within-task, and post-task epochs of a single session. Within-task periods are identified by lower delta power (0.5-4Hz) and higher theta power (6-9Hz). **B)** Population statistics for relative delta power, relative theta power, and theta-delta ratio. Pre- and post-task have higher delta power, but lower theta power and theta-delta ratio compared to the within-task period (p<4e-8; signed rank for all tests, Bonferonni corrected). These differences were not found between pre-task and post-task. **C)** Example AHV encoding for two cells split by the bottom (0-25th) and top (75-100th) percentile epochs of theta-delta ratio. High theta-delta ratio increases the baseline firing rate and abolishes AHV encoding. **D)** Average occupancy of each quartile of theta-delta ratio per task period. Occupancy is normalized within each period (pre-task, within-task, post-task). Each period had significantly different occupancies per quartile (pre-task: $F(1,3)=142.70$ p=9.87e-31; within-task: $F(1,3)=64.76$, p=5.64e-14; post-task: $F(1,3)=123.11$, p=1.65e-26; Friedman test). **E)** Average firing rate of cells in the NAcc (left) and VP (right) in epochs separated by 4 quartiles of theta-delta ratio. As theta-delta ratio increases, firing rate increases as well. Baseline firing rates are greater in the top quartile compared to the bottom quartile for both the NAcc and VP (NAcc: p=2.09e-15; VP: p=2.86e-9; signed rank test, Bonferonni corrected). **F&H)** AHV encoding split by the bottom (left) and top (right) quartiles of theta-delta ratio epochs in the NAcc and VP. **G&I)** There are more detected AHV cells during low theta-delta ratio epochs for the NAcc and VP ($\chi^2(4,N=564)=33.54$; p=9.25e-7; $\chi^2(4,N=492)=47.70$; p=1.09e-9 for NAcc and VP respectively). Bottom quartile theta-ratio AHV proportions - NAcc: symPos (16%, 45/282), symNeg (2.1%, 6/282), asymCW (7.5%, 21/282), asymCCW (9.9%, 28/282); VP: symPos (13.0%, 32/246), symNeg (4.1%, 10/246), asymCW (8.1%, 20/246), asymCCW (7.3%, 18/246). Top quartile theta-ratio AHV proportions - NAcc: symPos (3.2%, 9/282), symNeg (1.1%, 3/282), asymCW (6.7%, 19/282), asymCCW (6.4%, 18/282); VP: symPos (0.4%, 1/246), symNeg (1.2%, 3/246), asymCW (4.5%, 11/246), asymCCW (3.3%, 8/246). For all figures * p < .05, ** p < .01, *** p < .001

29

2.5   Discussion

In this study, we investigated whether individual neurons in the nucleus accumbens (NAcc) and ventral pallidum (VP) encode angular head velocity (AHV). In contrast to prior studies of the NAcc and VP (Lederman et al., 2021; McGinty et al., 2013), we report that a third of cells in the NAcc and VP robustly encode AHV during task-free behavior **(Figure 2.1).** This AHV encoding is lost when the animal is placed in a task context, where the encoding is instead replaced by cue and reward processing **(Figure 2.3, Figure S2.6)**, but AHV encoding clearly returns recovers when the animal returns to a task-free context **(Figure 2.2, Figure S2.3).** Further investigation revealed that this loss of AHV encoding is coupled to motivated behavioral states, identifiable by pronounced hippocampal theta oscillations and reduced delta rhythms (**Figure 2.3, Figures S2.9 and S2.10**). These results may potentially explain why AHV cells were not previously reported in the NAcc and VP, since studies which investigated spatial navigation or orientation encoding in these structures were primarily performed within contexts that involved active reward consumption (Lavoie & Mizumori, 1994; Lederman et al., 2021; Martin & Ono, 2000; McGinty et al., 2013). Our findings may be unique to the regions in the mesolimbic reward circuit, as AHV cells in other brain regions have been identified mostly during motivated behavior (Bassett et al., 2001; Mehlman et al. 2019; Stackman et al., 1998). Therefore, the mesolimbic reward circuit may be ideally suited for a state-dependent switch between spatial orientation and reward encoding.

It may be computationally beneficial for reward processing regions to also have the capacity for navigational encoding. Previous work has hinted that major components of the mesolimbic reward circuit, namely the NAcc, VP, and ventral tegmental area (VTA), have important roles in spatial navigation. Indeed, selective manipulations of these regions lead to deficits in spatial

learning (Annett et al., 1989; Ito et al., 2008; Jongen-Rêlo et al., 2003; van der Meer et al., 2014), suggesting that these brain regions encode fundamental information about orientation or place, consistent with our finding of robust AHV encoding in the NAcc and VP.

We report that over a third of cells in these regions encoded AHV **(Figure 2.1)**. This is a considerably larger proportion AHV cells than those found in many other brain regions (outside of the traditional angular velocity pathway; Bassett et al., 2001; Sharp et al., 2001; Stackman et al., 1998): 15% of cells in the somatosensory cortex (Long et al., 2022), 17% in the parahippocampus (Spalla et al., 2022), 18% in the precentral cortex (Mehlman et al. 2019), and 7% in the dorsal striatum (Mehlman et al. 2019). One exception to these low proportion of observed AHV cells is the retrosplenial cortex, where 62% of cells were found to encode AHV (Keshavarzi et al., 2022). However, the proportion of AHV encoding in the retrosplenial cortex study may be inflated due to differences in statistical methodology: Keshavarzi et al. (2022) required that the correlation of AHV and spike rate be greater than 95% of the shuffled distribution, whereas we utilized a stricter 99% threshold among two other criteria (see methods). When we used Keshavarzi and colleagues' criteria, we found similar AHV proportions in the NAcc and VP (61% and 58% respectively, data not shown) as reported in the retrosplenial cortex (62%). This highlights the need for careful consideration before making comparisons of AHV proportions across brain regions, but also emphasizes the remarkably robust encoding of AHV by a significant proportion of NAcc and VP neurons.

The NAcc and VP are not directly connected to parts of the ascending pathways where HD and AHV are computed from vestibular information (e.g. dorsal tegmental nucleus, lateral mammillary nucleus, vestibular nuclei; Root et al., 2015; Salgado et al., 2015). Instead, the NAcc

and VP may receive AHV signaling from the VTA, which is potentially a source of head rotation signals (Hughes et al., 2019). The VTA sends major dopaminergic projections to the NAcc and VP, such that stimulation of the VTA leads to significant downstream influence on NAcc and VP activity (Klitenick et al., 1992; Maslowski-Cobuzzi & Napier, 1994; Morales & Margolis, 2017). Behaviorally, VTA stimulation modifies movement response/vigor towards motivational stimuli (Hughes et al., 2020). Importantly, VTA GABA neurons encode rotational kinematics, synonymous with AHV signals, and selective stimulation of these neurons immediately induces head rotation (Hughes et al., 2019). Alternatively, the NAcc may compute AHV using orientation-related information arriving from the subicular formation (Cooper et al., 2006; Groenewegen et al., 1987). Collectively, the results presented here show that the NAcc and VP are well positioned to encode angular velocity information, but only during specific brain states, highlighting the state-dependent orientation and reward computations performed by neurons in the NAcc and VP.

2.6   Supplementary Figures and Tables

Brain Region	Total Units	HD Cells	Baseline Firing (Hz)	Peak Firing Rate (Hz)	Peak Firing Rate Range (Hz)	IC	Tuning Width (degrees)
NAcc	282	22	0.77	11.10±3.21	2.72-73.73	0.34±0.06	79.09±11.07
VP	246	8	1.0	14.35±4.31	3.31-32.31	0.32±0.09	94.50±15.58

Supplementary Table 2.1: Properties of head direction cells.

Values are denoted in mean ± SE. HD – head direction; IC - information content; Baseline firing (Hz) is defined as the firing rate outside of the preferred firing direction. Tuning curves of HD cells in the NAcc had an average width of 79.09 ± 11.07 degrees, and the mean directional information content was 0.34 ± 0.06 bits per spike. Peak firing rates at preferred HDs ranged from 2.72 – 73.73 Hz, averaging 11.10 ± 3.21 Hz. While we detected fewer HD cells in the VP compared to the NAcc (χ^2(1,N=528)=5.07, p=0.024), these HD cells displayed similar HD tuning properties in the tuning widths (94.50 ± 15.58 degrees, p>0.05, t-test), mean directional information content (0.32 ± 0.09, p>0.05, t-test), and peak firing rates (14.35 ± 4.31 Hz, p>0.05, t-test) when facing the preferred HD.

NAcc	Baseline Rate (Hz)	CCW Rate (Hz)	CW Rate (Hz)	CCW DoM	CW DoM	Pref. Rate (Hz)	Pref. DoM (abs. val)	N
SymPos	9.63±2.65	14.69±3.34	14.98±3.33	33.65±2.89	34.26±2.94	14.69±3.34	33.65±2.89	44
SymNeg	8.19±2.76	4.59±1.53	2.52±0.92	-32.82±5.26	-50.10±6.66	4.59±1.53	32.82±5.26	6
AsymCW	5.38±1.09	6.10±1.20	7.20±1.25	9.73±3.09	19.47±3.57	6.10±1.20	16.36±1.70	29
AsymCCW	5.00±1.63	6.87±1.55	5.70±1.46	22.14±4.29	2.99±7.22	6.87±1.55	27.62±2.82	27
No Mod	3.78±0.49	3.96±0.52	3.97±0.53	1.97±1.14	0.21±1.39	3.96±0.52	10.11±0.87	176
VP								
SymPos	11.14±2.95	15.96±3.09	15.94±3.15	31.31±3.76	30.77±3.55	15.94±3.15	30.77±3.55	31
SymNeg	17.40±4.05	12.56±3.58	13.06±3.87	-39.32±16.18	-53.06±29.59	13.06±3.87	53.06±29.59	12
AsymCW	9.18±3.51	9.40±3.29	10.40±3.44	12.77±6.07	19.74±5.78	10.40±3.44	24.41±4.43	17
AsymCCW	9.50±3.42	11.03±3.59	9.71±3.47	15.06±6.01	5.12±4.74	9.71±3.47	14.65±2.60	19
No Mod	8.67±0.79	8.73±0.79	8.79±0.80	0.25±0.97	-0.99±1.10	8.79±0.80	7.78±0.94	167

Supplementary Table 2.2: AHV subtype properties

Baseline rates are calculated at 0 deg/s, CCW rate at -200 deg/s, CW rate at +200 deg/s, and preferred rates were found for every cell prior to averages. Depth of Modulation (DoM) were calculated in CW, CCW, and preferred turn directions. Values are denoted as mean ± SE.
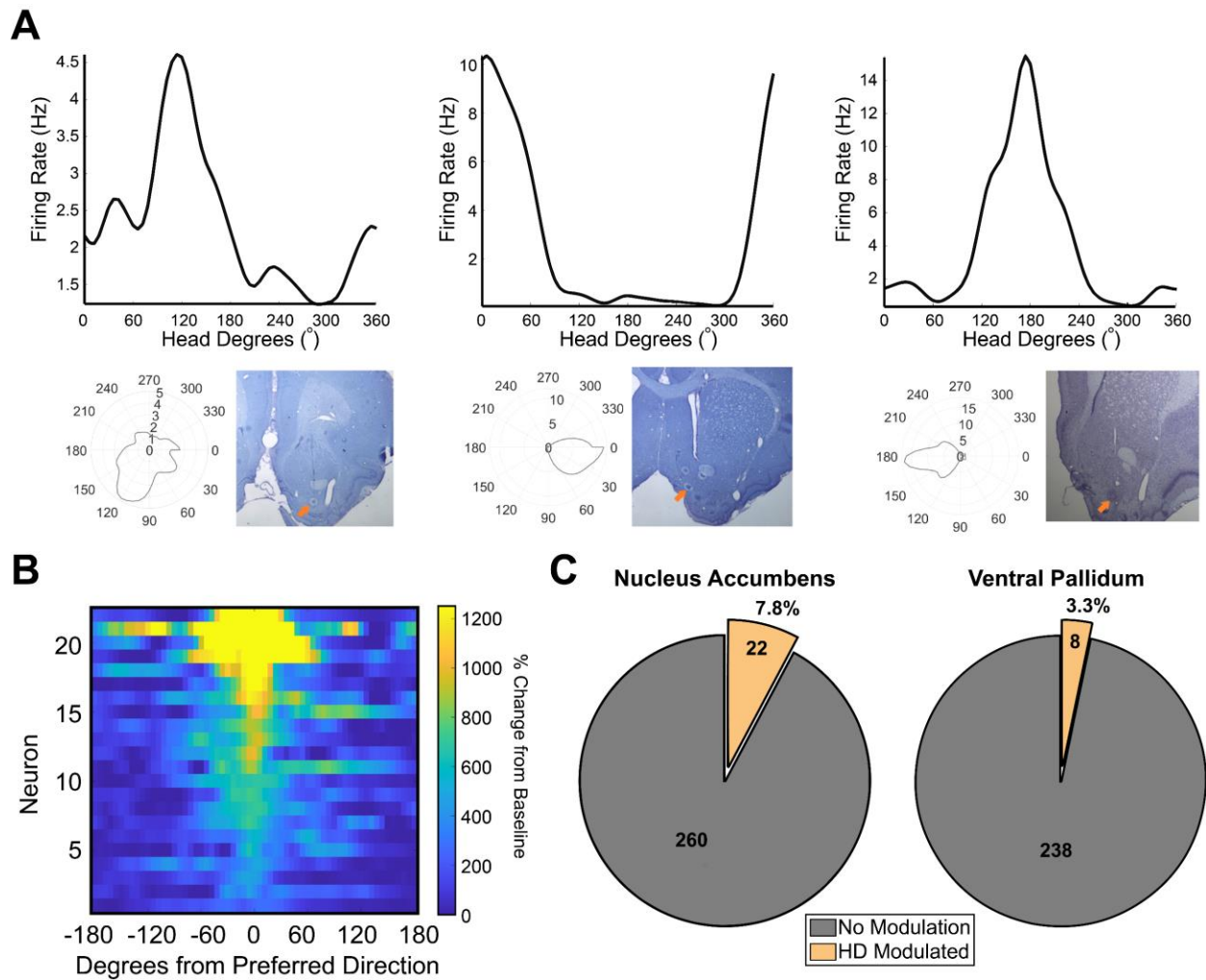
Supplementary Figure 2.1: Head direction cells in the nucleus accumbens

A) Three example head direction cells in the NAcc. Top: Tuning curve for each HD cell. Bottom left: Tuning curve shown as polar plots. Bottom right: Histology showing electrolytic lesions identifying location of each HD cell. Orange arrows denote the location of the lesion. **B)** Head direction cells aligned by preferred firing direction. Cells are sorted by the average percent change in firing rate ($\pm$ 60 degrees) from the baseline of the tuning curve. Many NAcc units exhibited a 5-fold firing rate increase at the preferred direction compared to baseline **C)** Pie chart indicating percent of head direction cells relative to all cells recorded in the NAcc (7.8%; Left) and VP (3.3%; Right).
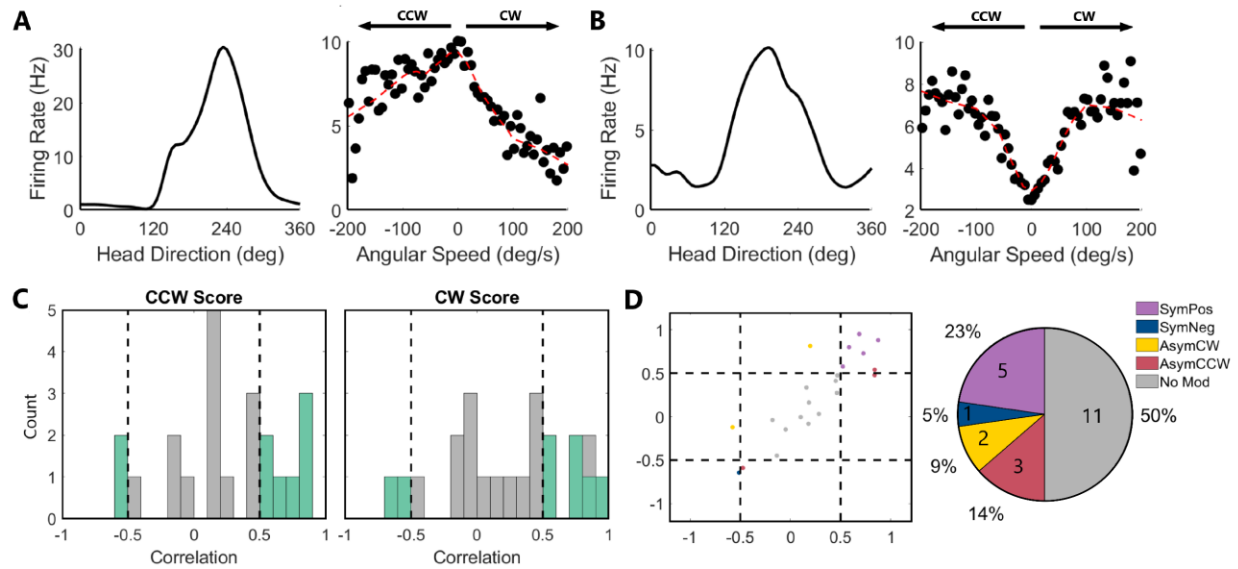
Supplementary Figure 2.2: Conjunctive NAcc HD-AHV cells

A&B) Examples of conjunctive NAcc HD-AHV cells with the head direction tuning curves (Left) and AHV response (Right). **C)** NAcc HD cell (n=22) AHV scores in CCW (left) and CW (right) directions. Vertical dotted lines denote the correlation threshold at ±0.5. Green shaded bars indicate cells that met the AHV cell criteria while gray indicate cells which did not. **D)** (Left) NAcc HD cells further categorized into the 5 AHV subtypes defined by the relationship of CCW and CW turn correlations. (Right) Pie chart identifying the percentage of AHV subtypes for the NAcc HD cells.
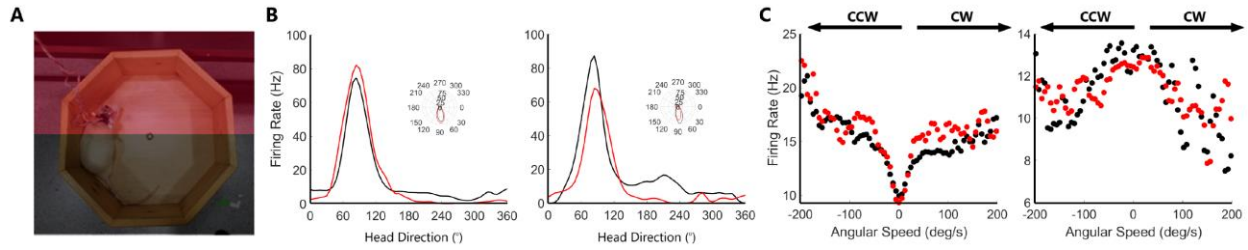
Supplementary Figure 2.3: Spatial stability of HD and AHV cells.
A) Depiction of the recording chamber partitioned into top (red) and bottom (black) halves. **B)** Two examples of NAcc HD cells in both halves of the chamber. The insets are polar plots for each corresponding HD cell. **C)** Examples of symmetric negative (symNeg; Left) and symmetric positive (symPos; Right) AHV tuning in the top and bottom halves of the recording chamber.
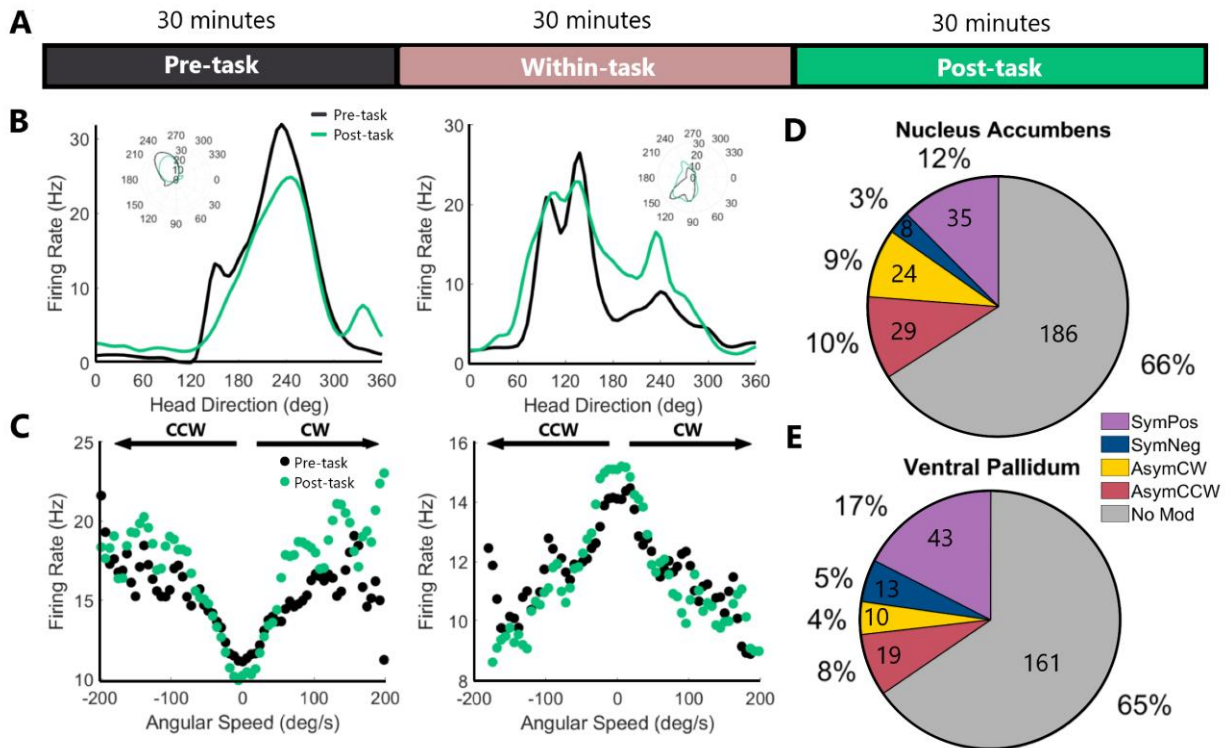
Supplementary Figure 2.4: Temporal stability of HD and AHV cells.

A) Recording timeline during pre-task , within-task , and post-task . The examples compare tuning curves during pre-task and post-task. HD proportions during pre-task were similar to post-task periods (post-task NAcc: 29/282, 10.3%, $\chi^2(1,N=564)=1.06$, p=0.304 when comparing to pre-task; post-task VP: 8/246, 3.3%, $\chi^2(1,N=492)=0.0$, p=1 when comparing to pre-task). **B)** Two examples of HD cells with stable HD tuning from pre-task to post-task recordings. The insets depict the polar representation of HD tuning. **C)** Examples of symmetric positive (symPos; Left) and symmetric negative (symNeg; Right) AHV tuning during pre-task and post-task epochs. **D&E)** Pie charts indicating AHV subtype classification during the post-task period in the NAcc and VP respectively. A total of 34.0% NAcc units and 34.5% of VP units encoded AHV during the post-task sessions. This proportion was similar to the 37.6% of NAcc units and 32.1% of VP units that encoded AHV in the pre-task session (NAcc: $\chi^2(4,N=564)=2.13$, p=0.712; VP: $\chi^2(4,N=492)=3.91$, p=0.418).

Supplementary Figure 2.5: Single unit responses during the PCA task

A-D) The population activity in heatmaps broken into the four individual epochs, with the average response of each cell (each row) sorted by the strength of change from the pre-CS baseline. These panels contain the same data as **Figure 2.2B**, but broken down to assess the differences statistically. The intensity of activity is generally similar between regions; however, more responses can be seen in the VP, particularly in the down-modulated direction. There were no significant differences in up-modulated responses during the CS onset epoch, the CS period, and CS offset (**A-C**), though down-modulated responses were stronger in VP than NAcc during the US epoch (Mann Whitney U = 316; p<0.01).

Supplementary Figure 2.6: AHV encoding during inter-trial-intervals of the reward task and using a lower angular speed range

A) (Left) Relationship of CW and CCW scores as well as the labeled AHV sub-type in the NAcc and VP during the inter-trial interval (ITI) of the PCA task. The ITI period was defined as a 14s period before the cue onset (-16s to -2s). (Right) Pie charts indicating the distribution of AHV subtypes during the ITI phase. **B-D)** Same as **(A)** but limited to assessing AHV encoding within ±80deg/s during the ITI **(B)** pre-task **(C)** and within-task **(D)** phases.
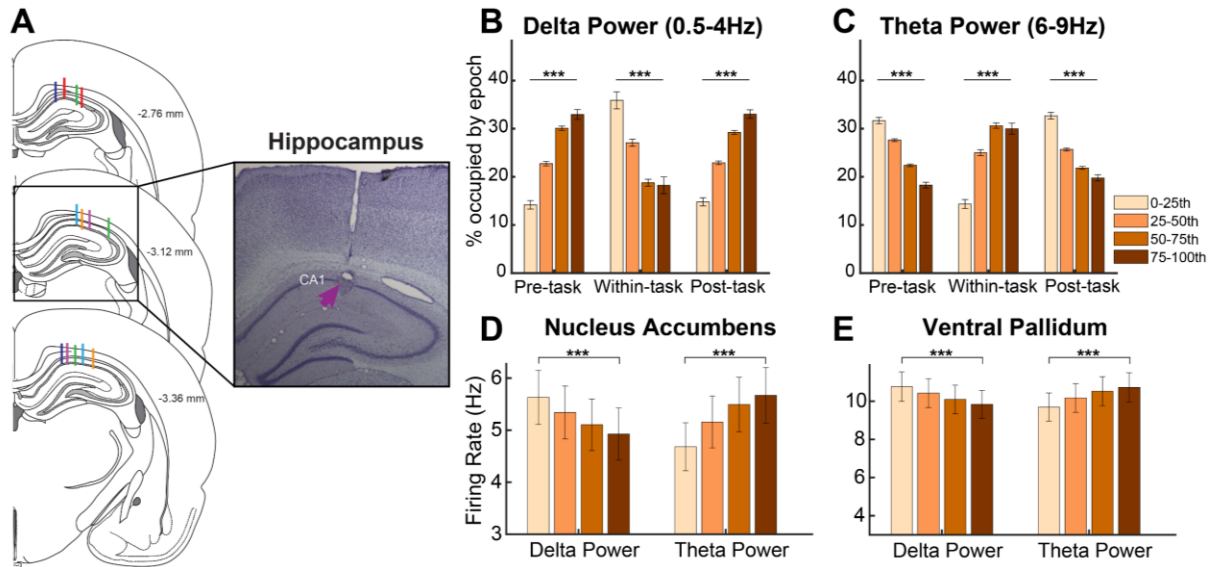
Supplementary Figure 2.7: Relative delta and theta power changes in the hippocampus
A) Hippocampal implantation sites. Each unique color represents tetrodes in a given animal. **B&C)** Changes in occupancy per period for relative delta power **(B)** and relative theta power **(C)** There are more pre-task and post-task periods, but less within-task periods captured as delta power increases. The inverse is true for theta power, where pre- and post-task occupancy decreases while within-task periods increase as theta power increases. These are significant changes in occupancy as the delta (Friedman test; pre-task: $F_{(1,3)}=116.61$, p=4.14e-25; within-task: $F_{(1,3)}=47.87$, p=2.27e-10; post-task: $F_{(1,3)}=132.28$, p=1.75e-28) and the theta power increases (pre-task: $F_{(1,3)}=134.92$, p=4.70e-29; within-task: $F_{(1,3)}=79.48$, p=3.97e-17; post-task: $F_{(1,3)}=106.95$, p=4.97e-23). **D&E)** Firing rate across quartiles for the NAcc **(D)** and VP **(E).** Firing rate decreases significantly between the bottom and top 25th percentile for delta and theta power in both the NAcc and VP (NAcc: p=7.43e-11 and p=1.53e-18 for delta and theta power respectively; VP: p=2.68e-7 and p=1.09e-9 for delta and theta power respectively; signed rank test).

41
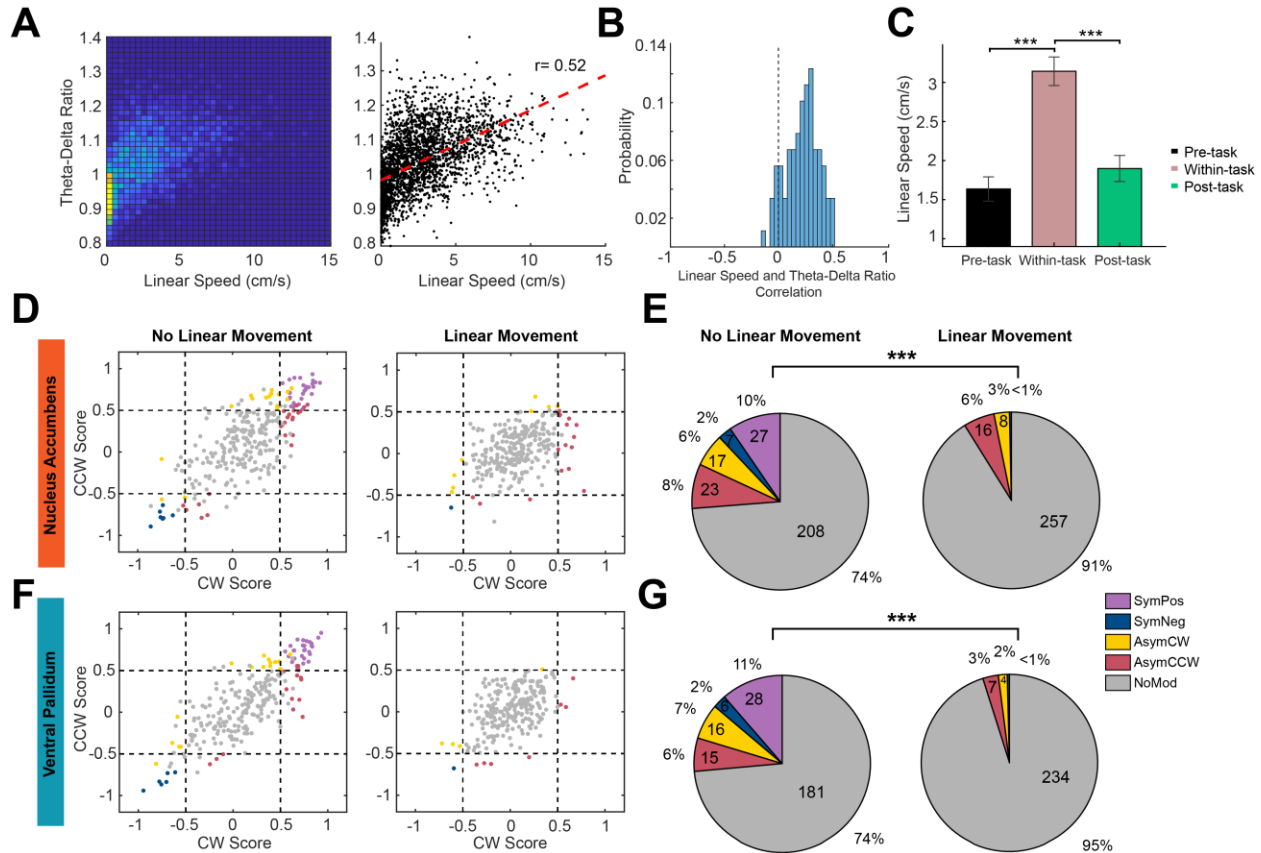
Supplementary Figure 2.8: Relationship of AHV encoding and linear speed

A) Example of a recorded session (including pre-task, task, and post-task periods) with the 2D histogram (left) and scatter plot (right) of linear speed and theta-delta ratio. **B)** Distribution of the correlation coefficients between linear speed and theta-delta ratio (n=89), which is different than a standard normal distribution (Kolmogorov-Smirnov test, p=2.17e-17). **C)** Average linear speeds in the pre-task, task, and post-task periods (n=89). There is greater linear motion during the within-task period compared to the pre-task and post-task periods (Wilcoxon signed-rank test, pre-task: p=1.15e-14, post-task: p=7.59e-14). **D)** Nucleus accumbens scatter plot of AHV scores without (<1cm/s) and with (>4cm/s) linear movement. **E)** Pie charts indicating the AHV subtypes identified in **D,** where more AHV cells are identifiable during no linear movement (χ^2(4,N=564)=41.6; p=2.49e-8). **F&G)** Similar to **D&E** but in the ventral pallidum (χ^2(4,N=492)=48.4; p=7.67e-10)
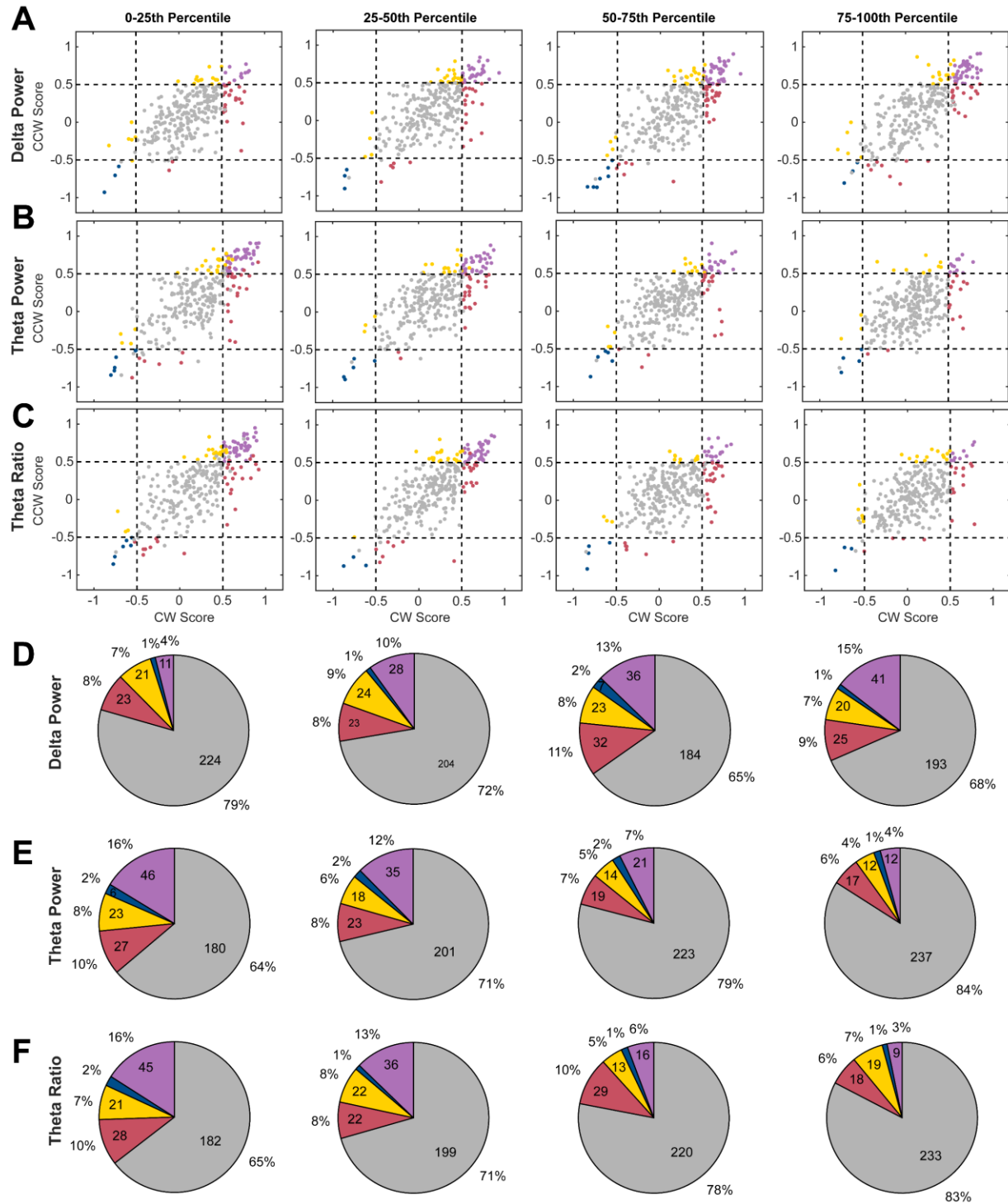
Supplementary Figure 2.9: Nucleus Accumbens AHV encoding across four quartiles
A-C) Nucleus Accumbens (NAcc) relationship of CW and CCW AHV encoding in four quartiles for relative delta power, relative theta power, and theta-ratio respectively. Each point is color coded as the classified AHV subtype defined in the methods. **D-F)** Pie charts indicating the AHV subtype distribution for relative delta power, relative theta power, and theta-ratio respectively. The numbers inside the pie chart indicate the number of cells in each category. Numbers are omitted in sections where the pie chart cannot accommodate the text.
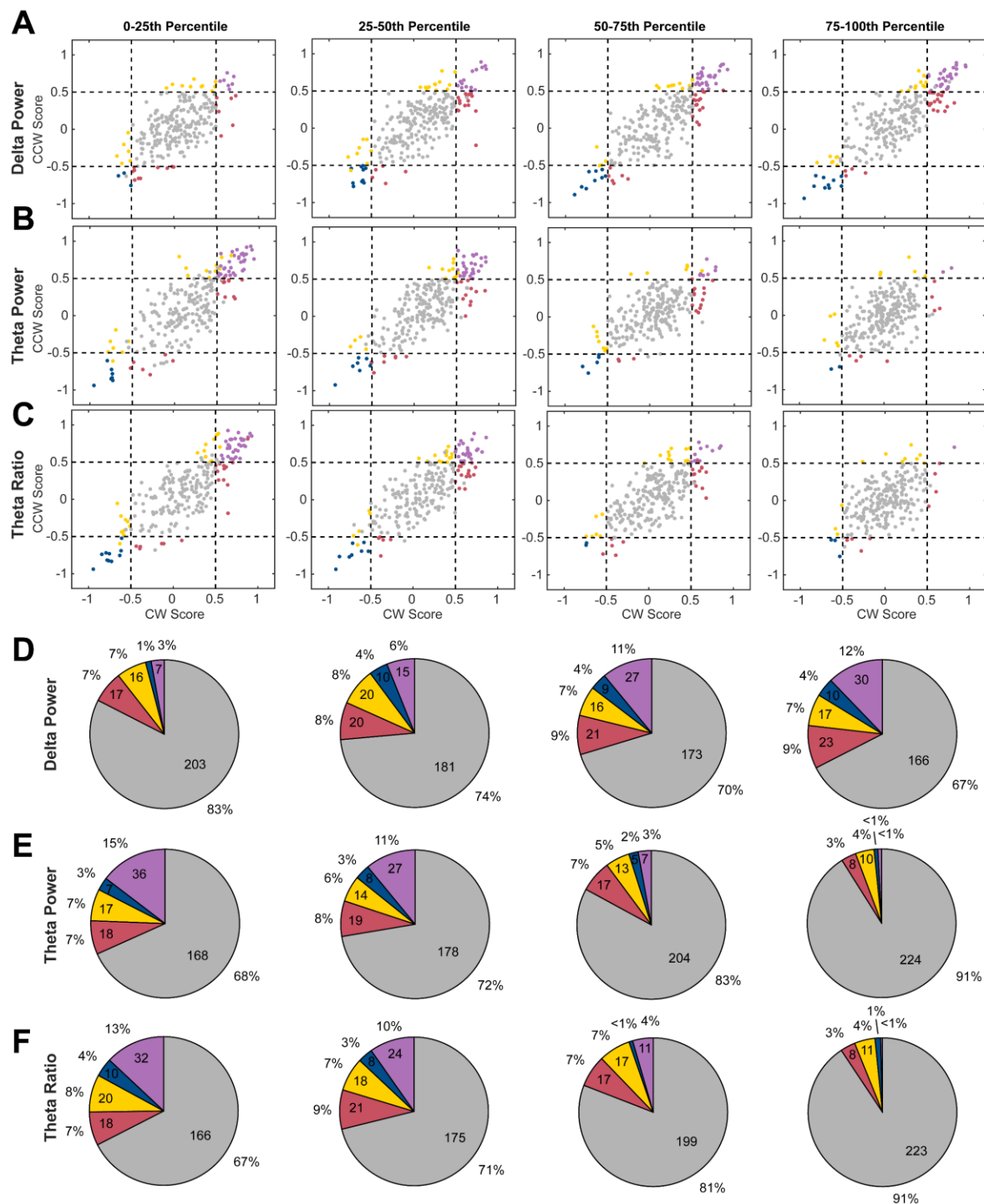
Supplementary Figure 2.10: Ventral Pallidal AHV encoding across four quartiles
A-C) Ventral pallidum (VP) relationship of CW and CCW AHV encoding in four quartiles for relative delta power, relative theta power, and theta-ratio respectively. Each point is color coded as the classified AHV subtype defined in the methods. **D-F)** Pie charts indicating the AHV subtype distribution for relative delta power, relative theta power, and theta-ratio respectively. The numbers inside the pie chart indicate the number of cells in each category. Numbers are omitted in sections where the pie chart cannot accommodate the text.

A)
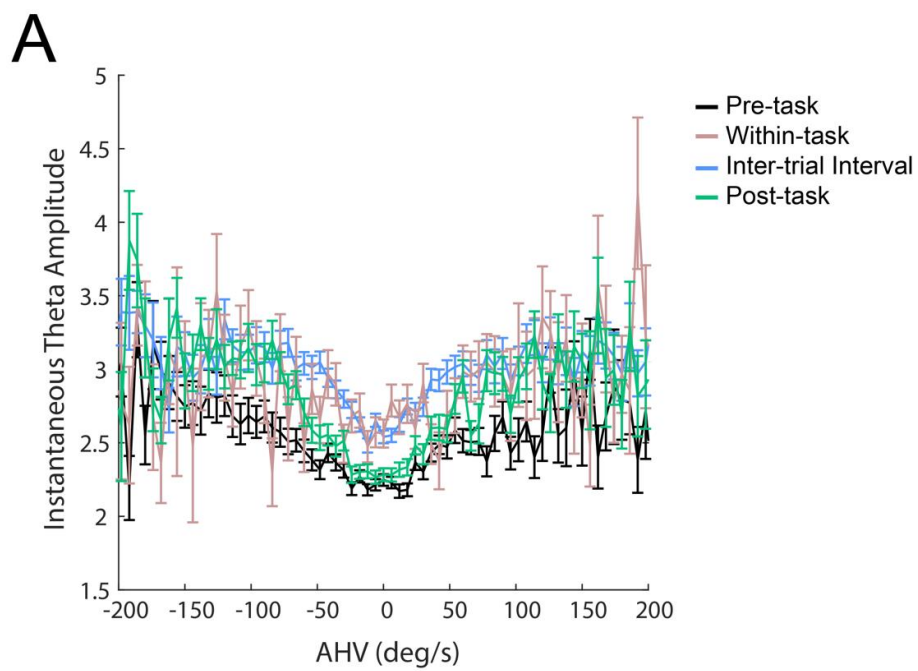
Supplementary Figure 2.11: Relationship of instantaneous theta amplitude and angular head velocity

A) The relationship of instantaneous theta amplitude and angular head velocity for an example animal session. Each panel shows this relationship during the four task periods (pre-task, ITI, within-task, post-task).

Chapter 3: Multi-timescale Coordination in the Nucleus Accumbens and Ventral Pallidum Reward Network During Hippocampal Ripples

Allison M. Ahrens*, Danny Siu*, & Omar J. Ahmed

3.1 Abstract

Sharp-wave ripples (SWRs) coordinate activity between the hippocampus and reward-related circuits during memory consolidation. This interaction is canonically considered to be short-lasting. Here, using simultaneous recordings across the dorsal hippocampus, nucleus accumbens (NAcc), and ventral pallidum (VP) in rats performing an appetitive conditioned approach task, we reveal multi-timescale coordination in this motivational circuit. Many NAcc and VP cells slowly decrease their activity for several seconds around SWRs. In the NAcc, these slow tonic changes are often accompanied by rapid phasic increases in firing just after SWRs during sleep and resting states. These multi-timescale NAcc neurons better encode task-related cues. Individual differences of approach behavior to reward cues correlate with differences in hippocampal SWR duration and with differences in SWR-triggered phasic drive of NAcc neurons. Our results thus highlight multi-timescale coordination between the hippocampus and NAcc that can facilitate individually different consolidation of cue and reward related information during periods of sleep and rest.

3.2   Introduction

Sharp wave ripples (SWR) are endogenous patterns of high frequency (150-250 Hz) network oscillations that are generated in the hippocampus during periods of awake rest and slow-wave sleep, and are critically involved in the consolidation of episodic memories. SWRs coincide with the reactivation or replay of neuronal ensembles in hippocampal-cortical networks that encode specific memories, which are considered a primary mechanism for the acquisition and consolidation of novel information (Buzsáki, 2015; Joo & Frank, 2018; Pfeiffer, 2020; Wilson & McNaughton, 1994). Disruption of SWR activity causes significant impairments in spatial working memory, particularly during the initial phases of familiarization with a new environment or learning a new task, when post-exposure consolidation processes are crucial for the formation of new memories (Ego-Stengel & Wilson, 2010; Girardeau et al., 2009; S. P. Jadhav et al., 2012; Wang et al., 2015).

Coordinated activity during non rapid eye movement (non-REM) sleep has also been observed between the hippocampus and subcortical structures that regulate appetitive learning and motivation (Girardeau et al., 2017; Gomperts et al., 2015; Lansink et al., 2008, 2009), and is critical for the integration of spatial representation with reward information and emotional memories (Girardeau et al., 2017; Sosa et al., 2020). Joint reactivation takes place between the hippocampus and nucleus accumbens (NAcc), with input from hippocampal neurons triggering replay of neuronal ensembles within the NAcc (Lansink et al., 2008, 2009; Sjulson et al., 2018). Reactivation in the NAcc typically takes place on a short time scale (<1 s) and is unidirectional in nature, with the strongest reactivation seen in cell pairs in which hippocampal firing immediately precedes NAcc firing (Lansink et al., 2009). The connections between the hippocampus (particularly dorsal but not ventral hippocampus) and the NAcc are critical for the

47

consolidation of memories that link information about reward to specific spatial locations (Sosa et al., 2020; Trouche et al., 2019).

Using the same dataset from Chapter 2, we examined the relationship between SWRs in the dorsal hippocampus and single unit firing in the nucleus accumbens and the ventral pallidum (VP). We simultaneously recorded neural firing and local field potential in the NAcc, VP, and hippocampus during daily sessions that included an initial period of rest, a Pavlovian conditioned approach (PCA) task, and then a post-task period of rest. The PCA task involved pairing an environmental cue (a retractable lever being extended into the cage for 8 s) with the response-independent delivery of a food reward (Flagel et al., 2009; Meyer et al., 2012; Robinson et al., 2014). Both the NAcc and the VP showed robust cue-related neural firing in a significant proportion of cells during the performance of the PCA task. During the pre- and post-task periods of rest, a portion of cells in both the NAcc and VP were modulated by hippocampal SWRs, and many cells were modulated by both the task and SWRs. In the NAcc, there were brief phasic responses on a short timescale (<1 s) that were influenced by cue-related activity during the task. We also found cells in the NAcc and VP that showed prolonged inhibition or excitation surrounding SWR events (lasting several seconds). In the VP, long duration modulation far outnumbered short duration modulation and was in fact the dominant response profile. In the NAcc, this long-duration modulation was often accompanied by short bursts of firing within milliseconds of SWR peaks, and the NAcc cells that showed this response combination were also more likely to respond to the reward cue during the PCA task. The results suggest that the shutting down of neurons in the VP, and perhaps the NAcc, represent a precursor for the occurrence of hippocampal SWRs, while also increasing the signal to noise ratio of subsequent reactivation of NAcc cells..

48

3.3 Methods

The animals and implants utilized in Chapter 3 is identical to Chapter 2.

3.3.1 Animals and Surgery

This experiment used male Sprague-Dawley rats weighing 300-400 g (Charles River; Colony P04). Rats were singly housed in standard polycarbonate cages with food and water available ad libitum throughout the experiment and a reverse 12:12-h light/dark cycle. Animals were handled and habituated for several days prior the start of the experiment to acclimate them to testing procedures. Seven rats were used, but the data from one rat was excluded due to missed tetrode placement. All procedures were approved by the University of Michigan Committee on the Use and Care of Animals. This experiment used chronically implanted electrode microdrives that contained 14 independently movable tetrodes (see Chapter 2 Animals and Surgery methods)

3.3.2 PCA Behavior training and quantification

Rats underwent five days of PCA training prior to surgery and 10-23 PCA sessions after surgery. Initial behavioral training (prior to surgery) took place in standard Med Associates operant chambers (30.5 x 24.1 x 21 cm; Med Associates). Each chamber was outfitted with a pellet dispenser connected to a reward port that recessed 3 cm into the chamber. The reward port contained an infrared sensor to record magazine entries. Furthermore, adjacent to the reward port was a retractable lever. When the lever was extended, it was illuminated with a white LED. There was a red house light opposite to the reward magazine that was illuminated during the entire session. Med Associates software was used to control the task. On the first day of PCA training, a banana pellet (45 mg of banana-flavored pellets; BioServ, #F0059) was delivered without a lever cue every trial for 25 trials to train the rat to retrieve the pellet. In the next five

days of PCA training, 25 trials/session were separated by variable inter-trial intervals (30-150 s, average 90 s). In each trial, an illuminated lever was extended (lever CS) for 8 s. After 8 s, the lever was retracted and a banana pellet was dispensed into the middle reward port.

After surgical implantation for electrophysiological recordings, PCA behavior was assessed in a custom operant chamber with larger dimensions than the standard Med Associates operant chamber. Since animals were implanted with a large microdrive, the custom operant chamber contained a reward port which protruded 4 cm out of the chamber to allow unobstructed entry to the magazine port. An identical PCA task to the training operant chamber was carried out in this custom operant chamber, and actions were recorded via an Arduino program. All input (magazine entries, lever presses) and output (reward delivery, lever cue) events were synchronized to the Neuralynx data acquisition system (Neuralynx, Inc, MT).

An animal's approach index was quantified by the preference to approach the lever compared to reward port through the average latency, probability, and response bias for each session scaled from -1 to +1. The latency score was defined as the difference in the time to first approach the lever and reward port during the 8s period. The probability is defined as whether the animal approached the lever or reward port in each trial. Finally, the response bias $(\frac{\#_{lever} - \#_{magazine}}{\#_{lever} + \#_{magazine}})$ quantifies the difference in number of lever presses and nose pokes. The approach index takes the average of these three scores, where a score of <-0.5 indicates goal tracking behavior and $>+0.5$ is sign tracking behavior (Flagel et al., 2009; Robinson et al., 2014).

3.3.3 Electrophysiological recordings

Neuronal activity in the Sprague-Dawleys was recorded continuously at 32 kHz on a 64-channel Digital Lynx SX acquisition system using Cheetah software (Neuralynx, Inc, MT; see Chapter 2 Electrophysiological recordings methods).

3.3.4 Analyses of neural activity

Single unit analyses were performed in MATLAB and Neuroexplorer (Nex Technologies). Only units with baseline (-5 to 0 seconds prior to onset of each task trial) pre-CS firing rates of >0.5 Hz were analyzed for task specific responses. The magnitude of task-triggered firing and modulations were determined by the cell's cue-evoked activity during four periods of the PCA task (see Chapter 2 PCA Task Analyses methods). Task triggered firing rate differences between STs and GTs were quantified with independent *t* tests and Bonferroni corrected for the CS onset, CS period, CS offset, and US periods.

SWR Detection and Modulation

SWRs were detected using LFPs filtered from 150 - 250 Hz on dorsal CA1 hippocampal tetrodes. SWRs were thresholded at 6 Z with shoulder minimums of 1 Z. SWR durations were extracted from these shoulder edges, as well as peak smoothed amplitudes with 12.5 ms smoothing bins. SWRs lasting less than 15 ms were discarded consistent with prior reports (Girardeau et al., 2017; Karlsson & Frank, 2009). Single units from the nucleus accumbens and ventral pallidum were included in these analyses. Single unit activity was centered onto SWR peaks in +/- 1 s windows for short duration re-activation, and +/- 30 s for long duration re-activation. SWR triggered PSTHs in +/- 1 s were calculated in 5ms bins, and PSTHs from +/-30 s were calculated in 50 ms bins.

SWR modulation was adapted from Jadhav et al., 2012. For the short duration re-activation, we identified -1000 ms to -500 ms as the baseline, and -50ms to 50ms as the modulation time. As for the long duration re-activation, we identified -30 s to -20 s as the baseline, and -8 s to 8 s as the modulation time. To determine SWR modulation, SWR triggered firing rates were randomly shuffled to create a sampled distribution as a baseline. First, 5000 surrogate permuted PSTHs were created by circularly jittering SWR triggered spikes, then averaged to generate a permuted baseline. Then, we calculated the squared difference of the real and baseline PSTH at the modulation time. Afterwards, we calculated the squared difference of the baseline PSTH for each of the 5000 permuted PSTHs at the modulation time to create a sampled distribution of squared differences. If the squared difference of the real PSTH and baseline PSTH was greater than 95% of the shuffled PSTHs, the neuron was determined to be SWR modulated. Otherwise, the neuron was determined to be non-modulated.

Signal amplification ratio

We evaluated signal amplification by calculating the ratio of peak firing change from the short and long duration SWR baselines. The percent change of peak SWR triggered firing rates (+/- 50 ms) from the short duration baseline (-1 s to -0.5 s) was calculated ($Peak_{short}$). For $Peak_{long}$ we found the difference from the peak firing rate (+/- 50 ms) from the short duration baseline (1s to -0.5s) and divided by the long duration baseline (-30 s to -20 s). The signal amplification ratio is $Peak_{short}/Peak_{long}$. A larger ratio indicates greater signal to noise from the long SWR triggered firing rate decrease preceding the brief peak SWR response.

3.3.5 Statistics

Statistical procedures were performed with R (version 4.0.3), MATLAB (2019b), and

GraphPad Prism (version 7.01). Results were considered significant for $p \leq 0.05$.

3.4 Results

To investigate the relationship between hippocampal SWRs and single-unit activity in subcortical structures, we implanted chronic microdrives with 14 independently movable tetrodes that targeting three areas (hippocampus, NAcc, and VP). We recorded from six rats in a total of 92 sessions (10-23 sessions each), and tetrodes in the NAcc and VP were advanced 40-330 µm before each session to record different cells each day (see **Figure 2.1A**). Hippocampal tetrodes were advanced before the first session until they reached the CA1 pyramidal cell layer and SWRs were clearly observed. These tetrodes then remained in place for the remaining sessions, with minor adjustments as necessary to compensate for gradual drift.

Each session began with 25-30 min of rest (the pre-task period) in an open-topped chamber with rats tethered to the acquisition system allowed to move freely or rest/sleep. Recording continued as rats were transferred to an operant chamber for the PCA task, where they received 25 pairings of a Pavlovian cue with food reward over 35-45 min. The PCA task was followed by recording during another 25-30 min of rest (the post-task period). A total of 501 NAcc cells and 345 VP cells were recorded with respect to two events. First, unit firing was aligned to the onset of the reward-predictive cue during the PCA task (time 0 = CS onset). In Chapter 2, we investigated the response of NAcc and VP cells to the PCA task (**Figure 2.2A-C and S2.5**). Second, unit firing was aligned to the peak of hippocampal SWRs during the pre-task and post-task periods (time 0 = SWR peak).

The PCA task is known to elicit individual differences in the type of conditioned behavior that animals display, with some rats showing a tendency to approach and interact with the lever-CS (sign-trackers, STs) and others showing a tendency to approach and interact with the food cup where the reward is delivered (goal-trackers, GTs). These individual differences emerge

naturally in normal populations of outbred rats (Meyer et al., 2012; Fitzpatrick et al., 2013), and were observed in the animals in the current study. Of the 6 rats tested, 4 were GTs and 2 were STs based on behavior during the sessions in which neural activity was recorded (**Figure 3.1**). Rats underwent 5-7 days of initial training prior to recording, but neural data was only recorded during later sessions after the CS-US pairing was learned and conditioned behavior was stable. In the following results, we first analyzed neural data with all rats in a single group before examining individual differences between STs and GTs.
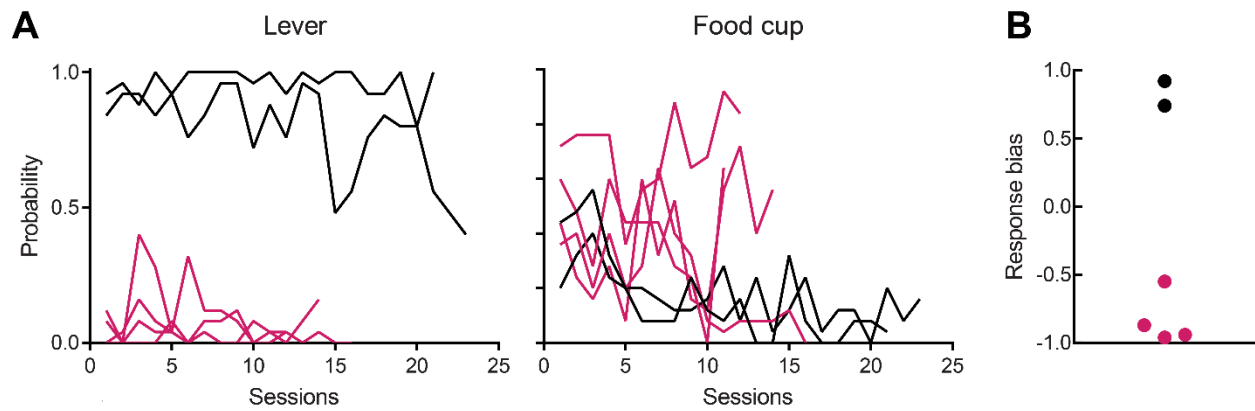
Figure 3.1: Behavioral profiles
A) There were individual differences in behavior during the PCA task, with rats showing preferential approach to either the lever-CS or the food cup during the 8-s cue period that preceded the food reward. Figures show the probability of contacting either the lever or the food cup (out of 25 trials per session) for two rats that preferred the lever-CS (black) versus four rats that preferred the food cup (magenta). **B)** Average response bias across all sessions (response bias = lever probability – food cup probability; +1 indicates lever preference and -1 indicates food cup preference).

56

3.4.1 NAcc unit responses to the food CS are associated with greater SWR-triggered activity after the task.

Neural activity in the NAcc, VP, and hippocampus was recorded during a 25-30 min pre-task resting period while animals waited in a wooden apparatus next to the operant chamber. Recording continued as animals were transferred to the operant chamber to perform the PCA task described above. The PCA task was followed by another 25-30 min resting period in the turning bowl. Hippocampal SWRs were examined during the pre-task and post-task periods of rest, and single-unit firing was aligned to the peak of detected SWRs (**Figure 3.2A**). We found that many cells in the NAcc and VP were responsive to hippocampal SWRs on a short timescale. We categorized cells as being responsive to SWRs either before the task (Pre only), after the task (Post only), or both before and after the task (Both) (**Figure 3.2B**).

The VP had relatively few short-timescale responses to SWRs (11.3% total). Of these 63.6% were positive (excitation), and there were similar proportions of Pre only, Post only, and Both responses (**Figure 3.2C**). The NAcc had more SWR-responsive cells than the VP (24.5% total). Of these, 84.4% were positive, and there was a similar proportion of Pre only, Post only, and Both responses (**Figure 3.2D**). In contrast, almost all single units recorded in the hippocampus were responsive to SWRs (94.8% total) and only positive responses were observed. Most of these cells were responsive both before and after the task (**Figure 3.2E**).

We found that some SWR-responsive cells were also responsive to the lever-CS during the PCA task. Although overall proportions of Pre only, Post only, and Both cells in the NAcc were similar, cells in these categories had different task responses. Post-only cells that responded to SWRs after the task, but not before, were more likely to also respond to the CS during the task. Post-only cells had a higher proportion of responses to CS onset, the CS period, and CS

offset compared to non-responsive cells (Post only compared to None; $\chi = 5.5\text{-}10.1$; $p < 0.05$ - 0.01). Cells in the Both category also had more CS onset responses compared to None ($\chi = 4.6$; $p < 0.05$), but cells in the Pre only category did not differ from None at any point in the task (**Figure 3.2F**). Average activity during the task was higher for Post-only cells than Both or Pre-only cells (one-way ANOVA of CS onset period, $p < 0.05$; multiple comparisons Post only vs None, $p < 0.05$) (**Figure 3.2G**).
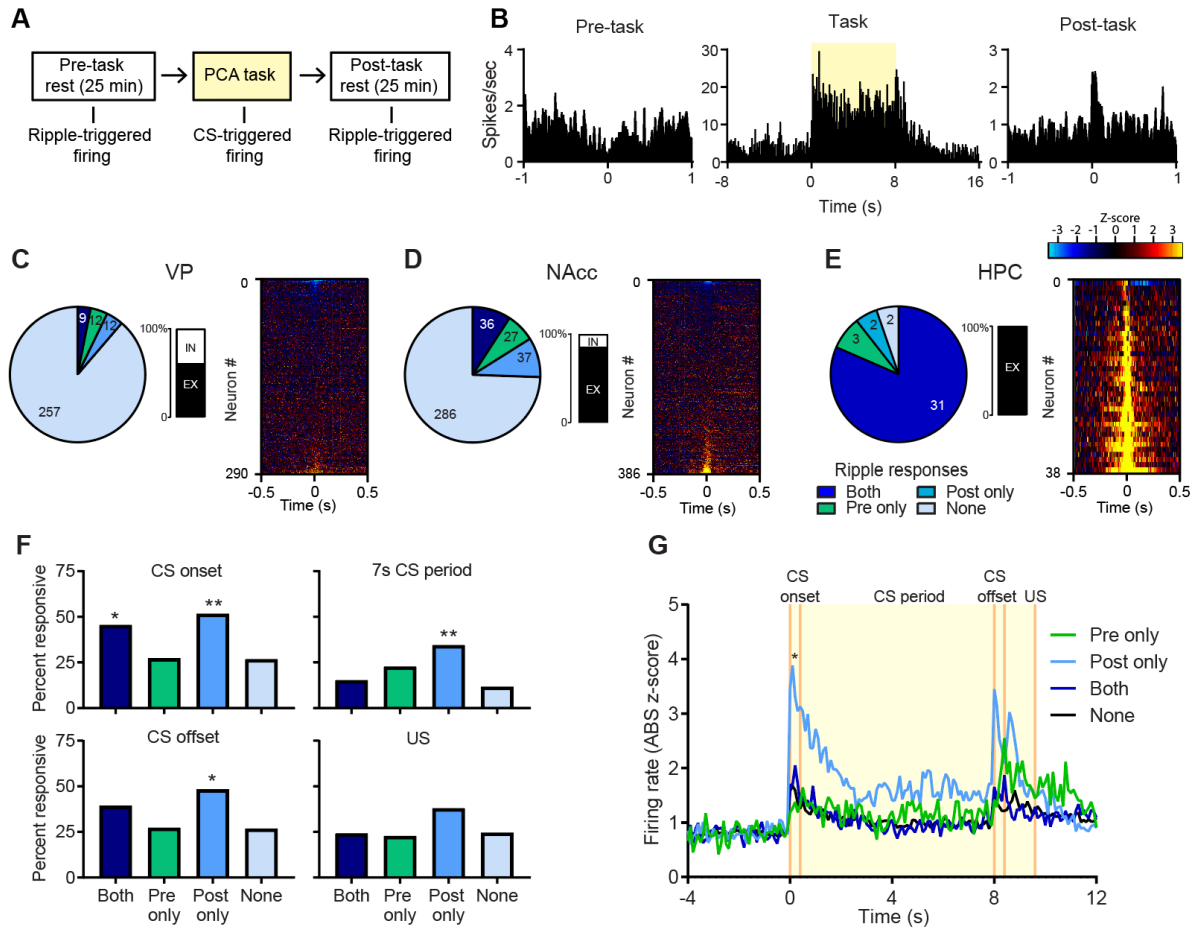
Figure 3.2: NAcc cells with post-task SWR responses are more likely to also show cue-related activity

A) Cells were continuously recorded during 25 min of rest (Pre-task), during performance of the Pavlovian Conditioned Approach task (PCA task), and during another 25 min of rest (Post-task). Responses to hippocampal SWRs were examined during the pre-task and post-task periods, and responses to the food-paired cue (CS) were examined during the PCA task. **B)** An example NAcc cell that was not responsive to SWRs during the pre-task period, but then showed a strong positive response to the task CS, and subsequently showed a positive SWR response in the post-task period. **C-E)** Pie charts show the proportion of cells that were responsive to SWRs before the PCA task (Pre only), after the PCA task (Post only), both before and after the task (Both), or were not responsive (None). Bars in the middle show the percentage of SWR responses that were excitatory (EX) or inhibitory (IN) during the post-task period. Panels on the right show the activity of each recorded cell aligned to SWR peak during the post-task period. **F)** Figures show the percentage of cells in each SWR-response category (Pre only, Post only, Both, None) that were also responsive to different task events (CS onset, CS period, CS offset, US). Cells in the Both category had significantly more responses to CS onset, and cells in the Post-only category had significantly more responses to CS onset, CS period, and CS offset. **G)** Cells in the Post only category had greater average responses to CS onset than cells in the Pre only and Both categories (* $p < 0.05$, ** $p < 0.01$).

59

3.4.2   NAcc and VP show long-duration modulation by hippocampal SWRs

We further examined the relationship between hippocampal SWRs and single unit firing

in the NAcc and VP by extending the window of response detection to 15s before and after peak

SWR times. We found that many cells in the NAcc and VP showed significant changes in firing

in this long-duration timescale (**Figure 3.3A**). The most prominent were slow decreases in firing

(type 1) or increases in firing (type 2) that happened on the scale of 2-10 s before and after

SWRs. There were also brief phasic increases or decreases (types 3 and 4 respectively), that were

detected with a 50ms window around SWR times. These brief responses are the same short

timescale responses described in previous sections; however, they are designated as type 3

(increases) and type 4 (decreases) in the current analysis. Interestingly, many cells showed a

combination of long duration responses and short duration responses. The most common

combination was type 1+3. These cells showed slow decreases in firing around SWRs on a long

timescale, as well as sharp increases in firing within milliseconds of SWRs (**Figure 3.3A**). Other

combinations were observed but were relatively infrequent, such as type 2+4 (long-duration

increase with short inhibition), type 1+4 (long-duration decrease with a brief and distinct

additional decrease at SWR onset), and type 2+3 (long-duration increase with a brief and distinct

excitation at SWR onset).

More than half of the cells recorded in the NAcc and VP showed some type of SWR

response during the pre-task period (**Figure 3.3B**). In both areas the most common were type 1,

followed by type 2. Type 3 and type 1+3 were frequently observed in the NAcc but not the VP,

which is consistent with the higher proportion of excitatory short-duration SWR responses in the

NAcc shown in Fig. 2. Type 4 were infrequent in both the NAcc and the VP, as were the other

combinations of long and short responses. Long-duration responses were rarely observed in the

60

hippocampus. The majority of hippocampal cells were type 3 (89.5%) with only a few cells in other categories (**Figure 3.3B**). The overall population activity of the NAcc is shown in a heat map sorted by Z-scores in ±8 s around peak SWR times (**Figure 3.3C**).

In the NAcc, only the type 1+3 cells have a significant relationship with cue responses during the task. Type 1+3 cells, but not types 1, 2, 3, or 4 alone, are more likely to show CS onset responses than cells that do not respond to SWRs ($\chi = 6.004$; $p < .05$) (**Figure 3.3D**). Other combinations (types 2+4, 1+4, and 2+3) were not examined due to insufficient n. The VP had very few type 1+3 cells or type 3 cells, and for types 1 and 2 there were no significant relationships with cue responses during the task.
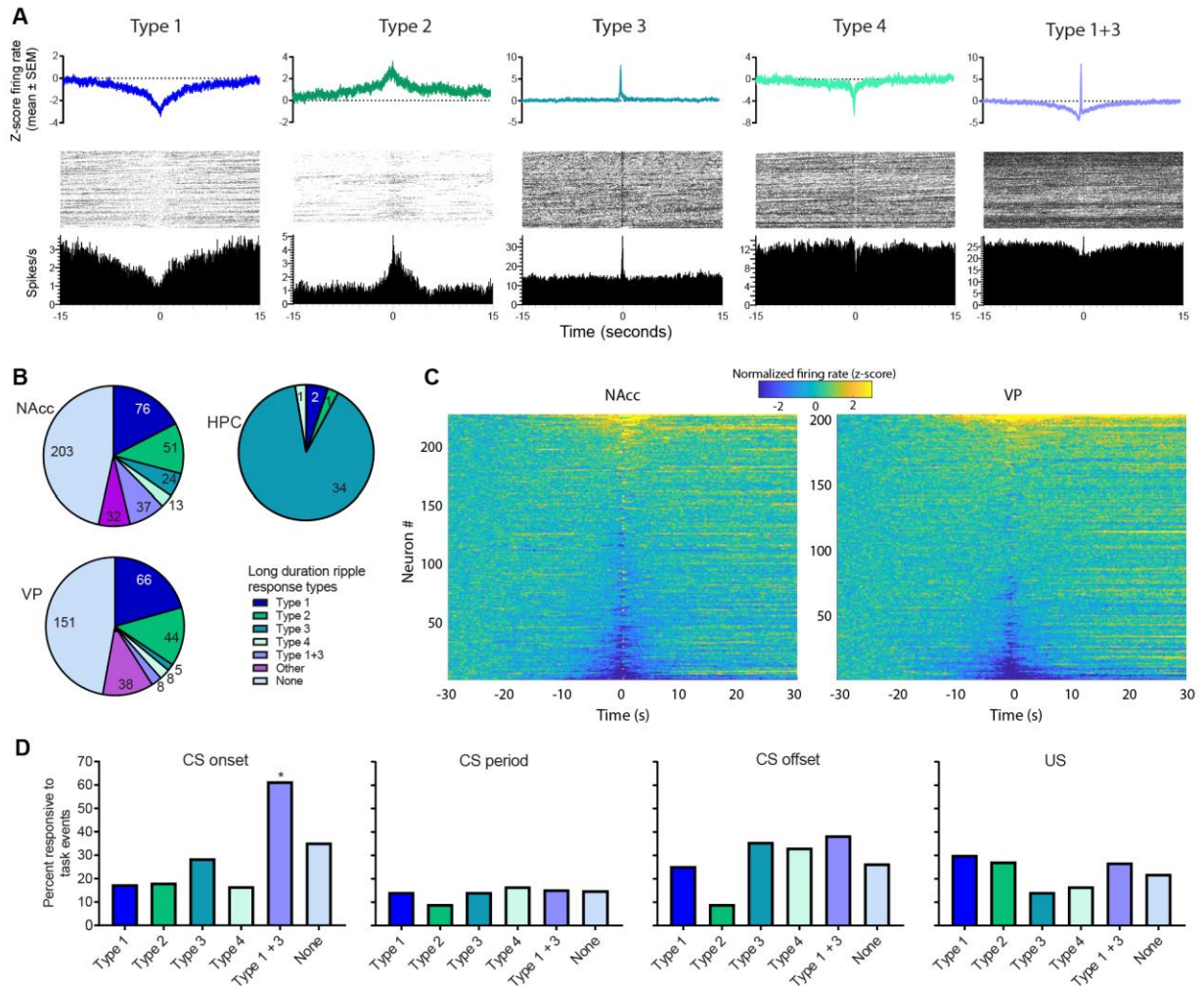
Figure 3.3: Long-duration modulation of NAcc and VP activity by hippocampal SWRs

A) Examples of NAcc cells that show long-duration responses to hippocampal SWRs. There were long-duration decreases or increases (types 1 and 2), short-duration increases or decreases (types 3 and 4), and combinations of long and short responses (type 1+3). Top shows average firing rate of NAcc cells in each category. Bottom shows histograms and rasters of example cells from each category. **B)** Pie charts show the proportion of NAcc, VP, and hippocampal cells that show SWRs responses during the pre-task period. **C)** Heatmap shows population activity of all cells recorded in the NAcc and VP in the pre-task period, sorted by activity in a ±8 s window around SWR peak. Slow inhibition (type 1) or excitation (type 2) can be seen up to 10 s before and after SWRs. Short excitation (type 3) or inhibition (type 4) can be seen at time = 0 s. **D)** NAcc cells that show type 1+3 SWR responses during the post-task period are significantly more likely to respond to CS onset during the task ($p < .05$).

3.4.3   Multi-timescale modulation during SWRs can amplify signal-to-noise ratio

The existence of NAcc cells with both long-duration inhibition and short-duration excitation surrounding hippocampal SWRs (type 1+3) raises the question of whether there are advantages to this response pattern in terms of signal to noise ratio compared to cells that show only short-duration excitation without prior inhibition (type 3). We investigated whether type 1+3 cells had a greater peak excitatory response than type 3 cells due to the transient suppression of baseline firing. We created a signal amplification ratio by calculating the difference between the peak firing change (within 50 ms of SWR events) and the baseline firing rate that briefly preceded the SWR (-1 s to -0.5 s), and compared this to the longer SWR baseline (-30 s to -20 s). We found that type 1+3 neurons showed significantly ($p < .001$) greater signal amplification than type 3 neurons (**Figure 3.4**).
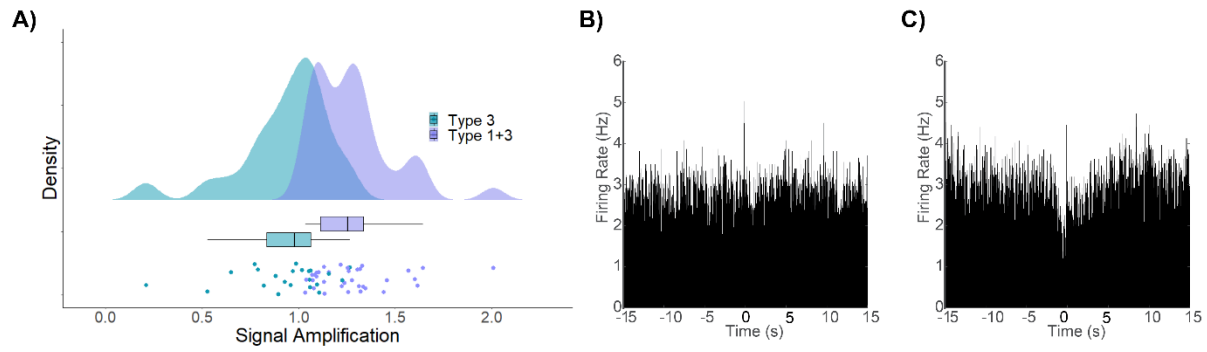
Figure 3.4: Signal amplification by multi-timescale SWR responses
A) Raincloud plot with the distribution, box plots, and individual units of type 3 (short duration excitation) and type 1+3 (long duration inhibition + short duration excitation) isolated units in the NAcc. Type 1+3 neurons have greater signal amplification than Type 3 neurons ($p < .001$). Examples of single units are shown for **B)** type 3**,** and **C)** type 1+3 on the long SWR time scale. In both examples, the transient short excitation can be seen at time 0.

3.4.4 Individual differences in SWR-triggered neural activity and SWR features

We looked at how individual differences in conditioned approach behavior were reflected in SWR-related neural activity. Since there was a low number of animals in the ST group (2 STs, 4 GTs) we could not analyze differences at the level of individual animals or split cells into multiple categories based on different task responses. However, with all cells from each group combined (ST n = 127 NAcc cells; GTs n = 259 NAcc cells) we found a striking difference in the percentage of NAcc cells that were responsive to SWRs on a short timescale, with GTs having significantly more SWR responses than STs both before and after the task [Pre-only, $\chi =$ 6.01, $p < .05$; Post-only, $\chi = 12.89$, $p < .001$; Both, $\chi = 24.38$, $p < .001$] **(Figure 3.5A&B)**. GTs showed stronger short duration SWR responses than STs during both the pre- and post-task periods **(Figure S3.1B&C)**. GTs and STs also showed differences in the features of the SWRs recorded in the hippocampus. We found that the duration of the SWR events were longer on average in GTs compared to STs using a Wilcoxon rank sum test [$p < 0.001$] during both pre- and post-task periods **(Figure 3.5C&D; Figure S3.1A)**. We found no significant differences between STs and GTs in short timescale SWR-triggered firing in the VP.
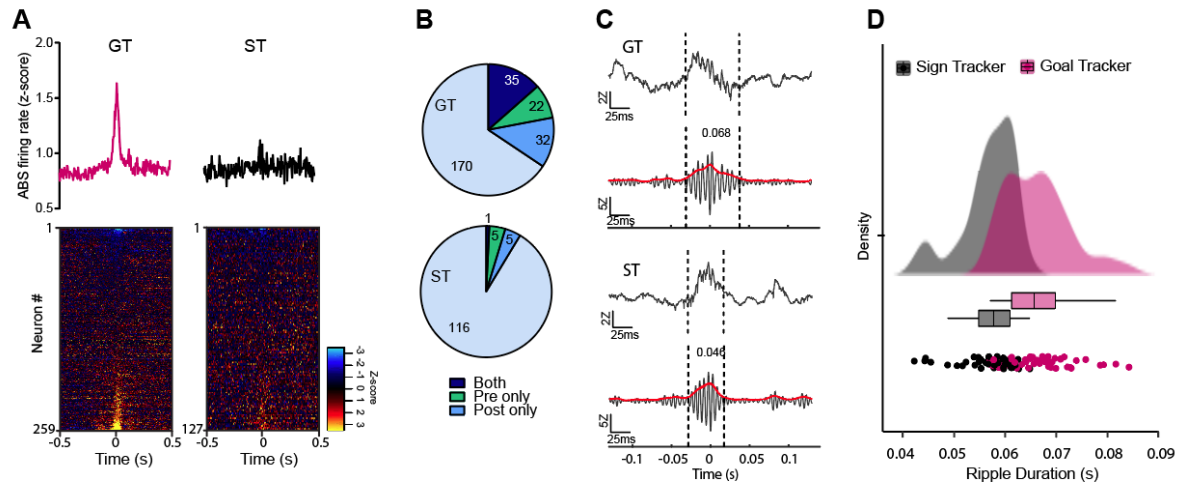
Figure 3.5 Individual differences in hippocampal SWR duration and NAcc responses to SWRs

A) SWR responses in NAcc cells recorded from GTs and STs during the pre-task period. Top shows activity averaged across all cells (shown as positive), and bottom shows heatmaps sorted by Z-score during SWR response epoch (-0.05 to 0.05). **B)** Percentage of GT and ST cells that are responsive to SWRs during the pre-task, post-task, or Both periods. Overall GTs have a significantly higher percentage of responsive cells than STs ($p < .001$). **C)** Representative examples of individual SWRs from GTs and STs with different durations, including unfiltered (top) and filtered (bottom) traces. **D)** Figure shows density and distribution of average SWR durations calculated for each recording session. GTs had significantly longer duration SWRs than STs ($p < .001$).

66

3.5 Discussion

In this study, we examined how firing patterns of individual cells in the NAcc and VP can be modulated by both reward-related cues and by SWRs in the hippocampus. Simultaneous tetrode recordings in these areas before, during, and after an appetitive task (Pavlovian conditioned approach, PCA) revealed that a significant portion of NAcc cells were responsive to SWRs on a short time scale, showing either increases or decreases in firing within 50ms of the SWR peak. These short-timescale responses were modulated by cue-related firing during the task, with positive cue responses leading to greater SWR responses after the task. We also found novel long-duration SWR responses in the NAcc and VP, which were slow increases or decreases in firing lasting several seconds before and after SWRs. In the NAcc, these long-duration changes were often accompanied by brief phasic responses in the opposite direction, a combination that effectively increased the signal-to-noise strength of the phasic SWR response. Furthermore, we found that the prevalence of short-timescale SWR responses in the NAcc varied based on individual differences in the conditioned behavior elicited by the PCA task, with rats presenting a goal-tracking (GT) phenotype having greater SWR-related activity than those presenting a sign-tracking (ST) phenotype. Strikingly, the duration of hippocampal SWRs was also longer for GTs than STs. Overall, these results characterize new types of multiscale interactions between the hippocampus and subcortical structures involved in reward learning and reinforcement.

The input from the hippocampus to the NAcc is important for the formation of associations between reward and spatial information. This pathway is activated by both reward and novelty, and is important for the initial consolidation of place-reward memories during learning, and for the retrieval of memories after learning has taken place (Lansink et al., 2008;

67

Pennartz, 2004; Sjulson et al., 2018; Sosa et al., 2020; Trouche et al., 2019). In the current study, as with several spatial studies that have examined this pathway the reward task was well-learned and familiar to the animal at the time of recording. Despite this familiarity, we found that the "post-only" cells that only responded to SWRs after the task were more likely to be activated by the Pavlovian cue. Therefore, even after performance was stable, exposure to the reward cue and context engaged a subset of NAcc cells and made them more reactive to hippocampal inputs during a subsequent period of rest.

The VP is a critical part of the mesolimbic system. It is the primary output structure of the NAcc (Root et al., 2015) and plays a major role in several aspects of reward and reinforcement (Smith et al., 2009). For example, VP has been shown to encode expected reward value (Tachibana & Hikosaka, 2012), the speed and vigor of reward-seeking behavior in an instrumental task (Avila & Lin, 2014; Richard et al., 2018), and the motivational salience of predictive cues (Ahrens et al., 2018; Ahrens, Meyer, et al., 2016; Lin & Nicolelis, 2008; Tindell et al., 2005). In the current study, we found that the VP had a smaller proportion of cells responsive to SWRs on a short timescale compared to the NAcc. The VP does not receive direct inputs from the hippocampus (Root et al., 2015); therefore, we did not expect to see a large population of VP cells that showed direct responses to SWRs. The fact that a handful of cells did show these responses may have been due to the placement of VP tetrodes, which primarily targeted the anterior and medial portion of the VP. At this location there is not a firm boundary between NAcc shell and VP. Electrophysiological characterization of cell types in this area shows a mix of NAcc-like medium spiny neurons that transition into more VP-like enkephalin-containing cells (Kupchik & Kalivas, 2013). However, it is also possible that the few VP short-duration responses were due to transient inhibition of upstream NAcc cells during SWRs. In

contrast to the short-duration SWR responses, the VP did have a significant portion of cells that showed slow, long-duration excitation or inhibition surrounding SWRs. These responses have not previously been reported in the VP. However, one previous study of primates looked at simultaneous electrophysiological recording in the hippocampus and fMRI in the rest of the brain, and found suppression of blood oxygenation level-dependent (BOLD) activity in the basal ganglia (which encompasses the VP) during SWRs (Logothetis et al., 2012).

We chose the Pavlovian conditioned approach (PCA) task because we were interested in how hippocampal SWRs interact with the subcortical neural activity that is triggered by a conditioned stimulus. This procedure is known to create a CS that has strong predictive and incentive value and elicits robust cue-related neural activity in mesolimbic structures (Ferguson et al., 2020; Flagel et al., 2010; Flagel & Robinson, 2017) as well as robust conditioned anticipatory behavior (Flagel et al., 2009; Meyer et al., 2012). Previous studies using electrophysiology in the NAcc and the VP (recorded separately) have demonstrated strong population responses to the lever cue during the PCA task (Ahrens et al., 2018; Ahrens, Meyer, et al., 2016; Gillis & Morrison, 2019). Although the overall pattern of responses looked similar in both the NAcc and VP, there are important differences. For example, simultaneous recordings of NAcc and VP in other appetitive tasks have shown that the VP contained more reward-selective neurons than the NAcc, and that the onset of responses in the VP preceded the onset of responses in the NAcc (Ottenheimer et al., 2018; Richard et al., 2016). Here we directly compared the NAcc and VP during the PCA task, and found that overall the VP had stronger cue responses than NAcc. There was a greater proportion of responsive neurons in the VP compared to the NAcc, particularly during the cue offset period and during retrieval of the food reward (US). Many of the responsive VP cells showed down-modulation (inhibition) instead of up-

modulation (excitation). This is consistent with a previous study of rostral-caudal differences in the VP, with the anterior portion of the VP (rostral to bregma = 0) showing a greater proportion of inhibitory cue responses than the posterior portion of the VP (caudal to bregma = 0) (Ahrens et al., 2018).

The PCA task has been well documented as a means of uncovering individual differences in the tendency to attribute incentive motivational value to cues. Many studies have found that rats that preferentially approach the lever cue (sign-trackers) show hypersensitivity in reward-related mesolimbic activity compared to rats that preferentially approach the food cup (goal-trackers) (Flagel et al., 2009; Robinson et al., 2014). For example, it has been shown that when exposed to a cue, sign-trackers experience greater cue-induced dopamine release (Flagel et al., 2010), greater neural activity in ventral tegmental area dopamine neurons (Ferguson et al., 2020), and greater neural activity in the VP (Ahrens et al., 2018; Ahrens, Meyer, et al., 2016) than goal-trackers. In this study, we did not have enough animals to perform a comprehensive analysis of ST/GT differences (2 ST, 4 GT). The individual variability in behavior requires larger *n* sizes for comparisons at the group level, and the number of cells obtained from each animal did not allow for analyses that break cell populations into several categories. We did, however, examine the overall population activity of NAcc and VP (with all ST cells and all GT cells combined) and found that GTs had more short-duration SWR responses than STs. We also found that the features of the SWRs reflected individual differences, with SWRs from GTs having a greater duration than SWRs from STs.

One might expect greater SWR-related activity in the NAcc of STs compared to GTs, since STs have typically shown greater activation of mesolimbic structures in the majority of

studies (Ahrens & Ahmed, 2020; Flagel & Robinson, 2017). However, most previous studies have looked at the activation that is triggered by the cue during active performance of an appetitive task. Relatively few have examined baseline differences between STs and GTs during periods of rest when the animals were not expecting to encounter cues or food reward, as was the case during the pre-task and post-task periods analyzed here. Furthermore, although STs are more responsive to physical cues that can be approached and contacted, there is evidence that GTs are more responsive to contextual cues and are faster to adapt when changes in context predict reward (Ahrens et al., 2016; Saunders et al., 2014). The fact that we saw a stronger baseline relationship between hippocampal SWRs and NAcc activity in GTs suggests that the strength of this connection may be a factor that underlies the individual differences that emerge when animals encounter contextual or discrete cues.

Importantly, a significant percentage of cells in the NAcc and VP showed prolonged increases or decreases in firing surrounding SWRs. For some of these neurons, the prolonged responses were accompanied by brief returns to baseline or greater during the 100ms window immediately surrounding the SWR, meaning that some cells showed both long-duration responses and short-duration responses in opposite directions. Similar response patterns have previously been reported in non-serotonergic neurons of the mesopontine median raphe (MnR) (Wang et al., 2015). In the study by Wang et al., it was determined that the prolonged decreases and short increases in MnR neurons were functioning to regulate the occurrence of SWRs. They found that MnR neurons suppressed SWR activity; therefore, slow decreases in MnR firing allowed for disinhibition of SWRs, and when the SWRs occurred, they were followed by a brief increase in MnR firing to prevent additional SWRs from occurring immediately afterward. This

71

was supported by optogenetic excitation and inhibition of the MnR, which caused a corresponding decrease and increase (respectively) in hippocampal SWRs (Wang et al., 2015).

Bidirectional interactions, albeit on shorter timescales, have been observed between hippocampal SWRs and other areas of the cortex. In the auditory cortex, hippocampal SWRs reactivate neural ensembles involved in memory consolidation, whereas pre-SWR activity in the auditory cortex predicts the firing rates of hippocampal neurons during SWR events (Rothschild et al., 2017). This type of cortical-hippocampal-cortical loop may facilitate the transmission and integration of sensory information into long-term memory storage. A similar mechanism may be involved in the consolidation of reward-related memory, with hippocampal SWRs triggering reactivation and replay in the NAcc, and long-duration changes in the NAcc facilitating or suppressing SWRs in the hippocampus. However, the current study did not directly assess directionality and future work will confirm whether long-duration firing changes in the NAcc and VP have a direct influence on SWR activity or if the same modulatory changes that increase the probability of SWRs also impact the firing or NAcc and VP cells over long timescales.

Overall, this study gives new insight into how the hippocampus interacts with NAcc and VP during encounters with a reward-paired cue that elicits incentive-motivational states and conditioned appetitive behavior. We found that hippocampal dynamics and NAcc reactivation depended on both exposure to the Pavlovian cue and the behavioral phenotype of the animal, suggesting that individual differences in how a cue is perceived can affect hippocampal engagement. We also observed long-duration changes in NAcc and VP firing surrounding SWR events, which could indicate bidirectional interactions between these areas, and the ability of subcortical structures to influence SWR activity in the hippocampus. Ultimately, these findings

will help us understand the mechanisms underlying the formation of memories associated with rewarded cues and contexts, how these associations are strengthened by repeated exposure, and how variability in these processes may result in maladaptive reward learning and compulsive behaviors.

3.6   Supplementary Figures and Tables
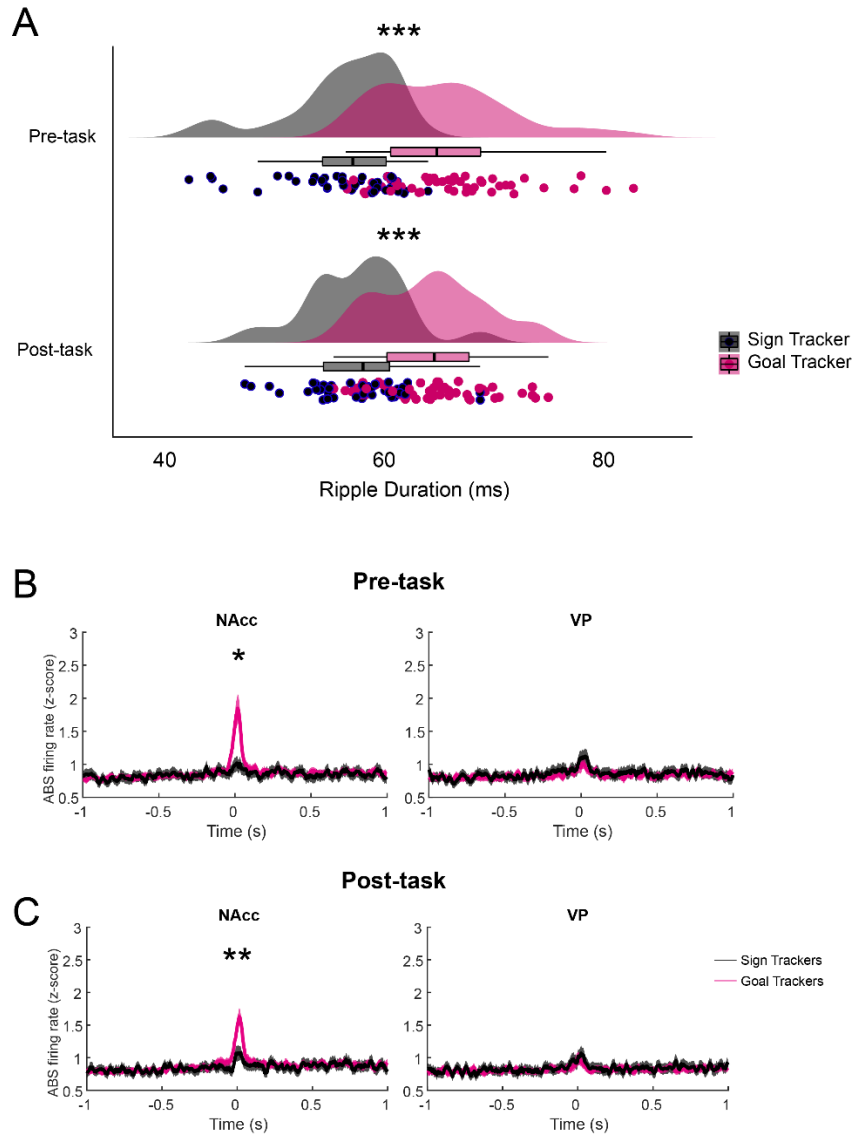
Supplementary Figure 3.1: Pre- and post-task ripple differences between sign and goal trackers

A) SWR durations are greater in goal trackers during both pre- and post-task period (p<0.001). **B&C)** There was greater NAcc single unit short duration ripple reactivation in goal trackers during both the pre-task (B) and post-task (C) periods.

Chapter 4: Seizures, Sleep, and Hippocampal Ripples in *Scn8a* Epileptic Encephalopathy

Danny Siu, Wenxi Yu, Vaughn Hetrick, Miriam H Meisler, Omar J Ahmed

4.1   Introduction

Developmental and epileptic encephalopathies (DEE) lead to cognitive impairments as well as an elevated risk of sudden unexplained death in epilepsy (SUDEP) (Meisler et al., 2021; Specchio & Curatolo, 2021). These conditions develop early in life, usually from *de novo* mutations, with many DEEs characterized by specific gene variants related to ion channels (Meisler, 2019; Mulley et al., 2005; Specchio & Curatolo, 2021). Approximately 1-2% of all epileptic encephalopathies are due to gain of function (GOF) *SCN8A* mutations in the voltage gated $Na_v1.6$ sodium channel alpha subunit (Johannesen et al., 2021; Meisler, 2019; Meisler et al., 2016). Most *SCN8A* patients suffer from pronounced intellectual disability and death commonly occurs in early childhood (Gardella et al., 2018; Johannesen et al., 2018; Kong et al., 2015). Recently, two GOF mouse models based on patient-derived *SCN8A* variants, p.Asn1768Asp (N1786D) and p.Arg1872Trp (R1872W) have been developed (Bunton-Stasyshyn et al., 2019; Wagnon et al., 2015). Fatal seizures are observed in these mouse models, and $Scn8a^{R1872W}$ mice suffer from more severe seizures than $Scn8a^{N1786D}$ mice with a shorter interval between first seizure and death (Meisler, 2019). Furthermore, the R1872W mutation in $Scn8a^{R1872W}$ mice can be conditionally expressed via Cre-induced recombination (Meisler, 2019).

Epilepsy alters sleep architecture, and is reciprocally known to be influenced by sleep deprivation (Malow, 2004; Papale et al., 2010, 2013; Quigg et al., 2016). However, there has

been a paucity of studies which investigated sleep patterns in human patients and rodent models of *SCN8A* encephalopathy (Gardella et al., 2018; Papale et al., 2010). Patients with heterozygous mutations, that are predicted to be GOF, did not conclusively display alterations in sleep architecture (Gardella et al., 2018). In the *Scn8a^{med-jo/+}* loss of function (LOF) mouse model, sleep-wake architecture is altered in various ways, including reduced time spent in awake and rapid eye movement (REM), as well as increased non-REM (NREM) states (Papale et al., 2010). While it is currently unclear how sleep architecture may change in GOF mutations, conditional expression in *Scn8a^{R1872W}* adult mice provides the opportunity to track such changes in subjects with a developed sleep circuit and an established circadian rhythm.

Hippocampal replay of experiences is essential for memory consolidation, and occurs most often during NREM sleep (Buzsáki, 2015). Hippocampal sharp wave ripples (SWR) are thought to be initiated by synchronous pyramidal cell activity in hippocampal CA3, which leads to a sharp wave deflection and brief 100-250 Hz fast oscillations in the CA1 (Buzsáki, 2015; Schlingloff et al., 2014). Reciprocal inhibition within inhibitory neurons in the CA1 helps to set the ripple frequency, while the strength of excitatory input from CA3 influences the duration and amplitude of SWRs (Schlingloff et al., 2014). In an *Scn1a* mouse model with heterozygous global LOF in sodium channel $Na_v1.1$, a dominant sodium current in GABAergic interneurons, hippocampal SWR frequency was lower than in controls (Cheah et al., 2019). However, it is unclear how SWRs will be impacted when $Na_v1.6$ channels have a GOF mutation that alters the excitability of excitatory neurons (Bunton-Stasyshyn et al., 2019) as well as select inhibitory neurons (Wengert, Miralles, et al., 2021).

To investigate these questions, we continuously monitored electrophysiological signals in conditional $Scn8a^{R1872W}$ mutant mice $(Scn8a^{R1872W+}$, CAG-Cre-ER+) after tamoxifen injection until the animals experienced SUDEP. By using a probe targeting the cortex, hippocampus, and thalamus, we observed that SWR in the hippocampus briefly precedes the cortex and thalamus during seizure events in these mice. Importantly, we found uniquely slow interictal discharges which may be predictive of SUDEP in $Scn8a^{R1872W}$ mice. To further investigate other potential biomarkers of seizures, we assessed the electrophysiological and sleep-wake architecture related changes over the course of epileptogenesis. Our results highlight a prolonged arousal state in $Scn8a^{R1872W}$ mice during light off periods, a time of day when mice are more active. These differences may arise early after activation of the mutant allele, since we did not observe changes in sleep-wake distribution nor an increase in sleep fragmentation in the 15 days leading to SUDEP. However, we did observe a slight decrease in duration and peak frequency of SWRs as mice approached SUDEP. Collectively, these results emphasize important hippocampal contributions to $Scn8a$ encephalopathy through hippocampal initiation and changes in SWR, as well as alterations in sleep architecture not previously reported in $Scn8a^{R1872W}$ mice.

4.2   Methods

4.2.1   Animals and Surgery

We used mutant mice with the patient mutation p.Arg1872Trp (R1872W) and a tamoxifen inducible Cre recombinase (*CAG-Cre-ER*). We implanted probes into *Scn8a*-Cre mice, five with tamoxifen-inducible Cre (*Scn8a$^{R1872W/+}$,CAG-Cre-ER$^+$*) and one control *Scn8a$^{R1872W/+}$* lacking Cre). Genders were balanced in our animals (3 males, 3 females). Mice were implanted at 3-4 months of age with NeuroNexus 32 channel probes (A1x32-Edge-5mm-100-177), with the tip of the probe targeting the thalamus (AP -1.9, ML +1.3, DV -2.9). Following surgical implantation, animals were allowed to rest for up to 5 days before the first neural recording. We first acquired several days of pre-injection data as baseline, then carried out tamoxifen injections. Tamoxifen injections were carried out in a different facility, preventing continuous recordings for an interval up to 10 days. After the animals returned, we recorded continuously until the final seizure leading to sudden death. For the sleep architecture analysis, we utilized an additional control animal (C57BL/6J WT).

4.2.2   Data Acquisition

Animals were recorded 24/7 for several weeks in their home cages. Electrophysiological signals were acquired at 32 kHz using an Open Ephys data acquisition system. Neural signals were digitized on the headstage (RHD2132, Intan Technologies Inc, CA), which also allowed the acquisition of 3-axis accelerometer signals due to the onboard chip (ADXL335). Video recordings were acquired at 10 frames per second using Blackfly S BFS-U3-23S3C-C cameras and synchronized with the electrophysiological signals using GPIO outputs, pulsed at every frame capture.

4.2.3 Sleep state classification

Using electrophysiological, video, and accelerometer data, we identified three main sleep states in these animals with a semi-automated procedure: awake, rapid eye movement sleep (REM), and non-REM (NREM). We scored hypnograms in 0.5s intervals. Awake states were identified by high movement signal by either the positional information extracted from video, or the accelerometer signal. NREM states were identified by high delta power (1-4 Hz) and low movement signal. REM states were identified by high theta (4-12 Hz), low delta (1-4 Hz) and alpha (12-20 Hz) powers which were combined as the theta ratio metric (theta/(delta+alpha)). Each sleep feature was calculated in 0.5s intervals with 2s sliding windows. Sleep states were first estimated with a machine learning classifier, followed by manual verification **(see Chapter 5)**.

4.2.4 Analysis of Neural Data

4.2.4.1 *Seizure and interictal discharge detection*

Epileptic events were characterized by synchronous, large amplitude neural activity followed by cessation of activity. These events were manually verified by human scorers. Recovery from seizures ranged from 30 seconds to minutes, and when animals did not recover, the event was identified as sudden unexplained death in epilepsy (SUDEP).

4.2.4.2 *Multi-day analysis*

With the exception of one animal, lights were maintained on a consistent 12:12 light:dark cycle. Out of seven animals, five were scheduled with a light:dark cycle of 01:00 and 13:00 respectively, one animal was scheduled with 07:00 and 19:00 respectively (Mouse 313), and one animal was manually maintained at 10:00 and 22:00 (Mouse 100). Recordings were aligned to the zeitgeber time (ZT), and we defined the lights on period as ZT 0-12 and lights off as ZT 12-

24. Multi-day analyses were performed for sleep architecture and sharp wave ripple. Due to the varying time before SUDEP, 1/5 *Scn8a*^{R1872W} mouse had 10 days of data available prior to SUDEP, and 4/5 *Scn8a*^{R1872W} mice had at least 15 days available. Of the two controls, one had 10 days of recordings, and the other had more than 15 days accessible.

4.2.4.3   Sleep architecture analysis

One animal was excluded from these analyses because the lights on/off periods were not consistent, leading to an irregular circadian rhythm (**Table 4.1; Figure S4.7C**). Manually scored hypnograms had a 30 second TMV applied to minimize transient sleep states. Hypnograms were scored in 2Hz time resolution followed by aggregation of sleep percentage and fragmentation using 12 hour time bins. To calculate the percent of time per sleep-wake state (awake, NREM, REM), the amount of time spent in a state was divided by each 12 hour time bin. State changes between any sleep-wake state such as awake to NREM, NREM to REM or REM to awake, were counted as a sleep transition. We modeled the changes in sleep percentage and transitions leading up to the SUDEP event using linear mixed effect models.

4.2.4.4   Sharp wave ripple detection

SWRs were detected using 100-250 Hz band-passed LFP. The SWR properties in the main analyses are derived from the dorsal CA1 of the hippocampus, identified by the electrode with the largest number of detected ripples during NREM. The 100-250 Hz LFP signal was z-score normalized within sleep states to account for different amplitudes in awake and NREM epochs, similar to the method described in sleep state classification above. SWRs were identified by z-scores greater than 6Z, with shoulders at 1Z indicating the start and end of the SWR. We

excluded SWRs lasting less than 15ms, and we required at least 250ms between each SWR event.

4.2.5   Statistical analysis

We utilized linear mixed effects models to analyze this longitudinal data in MATLAB (R2019b). As a form of multi-level modeling, linear mixed models (LMM) are advantageous when there is non-independence of statistical observations due to underlying grouping.

Sleep parameters such as time spent in each state and transitions were identified as fixed effects and SWR properties such as duration, amplitude, and rate were identified as fixed effects. Since animals were repeatedly sampled and were no longer independent, we used animal IDs as a random effect to account for both random slopes and intercepts.

4.3 Results

4.3.1 *Scn8a^R1872W* mice have seizures which lead to SUDEP

We continually recorded from *Scn8a^R1872W*,CAG-Cre-ER⁺ mice (n=5; control n=1) with an

implant spanning the cortex, hippocampus, and thalamus until animals underwent sudden

unexplained death in epilepsy (SUDEP) **(Figure 4.1A)**. When animals were sent to a separate

facility for tamoxifen injections, we were unable to record data for up to 10 days **(Figure 4.1B)**.

Most mice (4/5) underwent SUDEP in fewer than 30 days from the time of injection, while one

animal required 52 days before SUDEP **(Table 4.1)**.
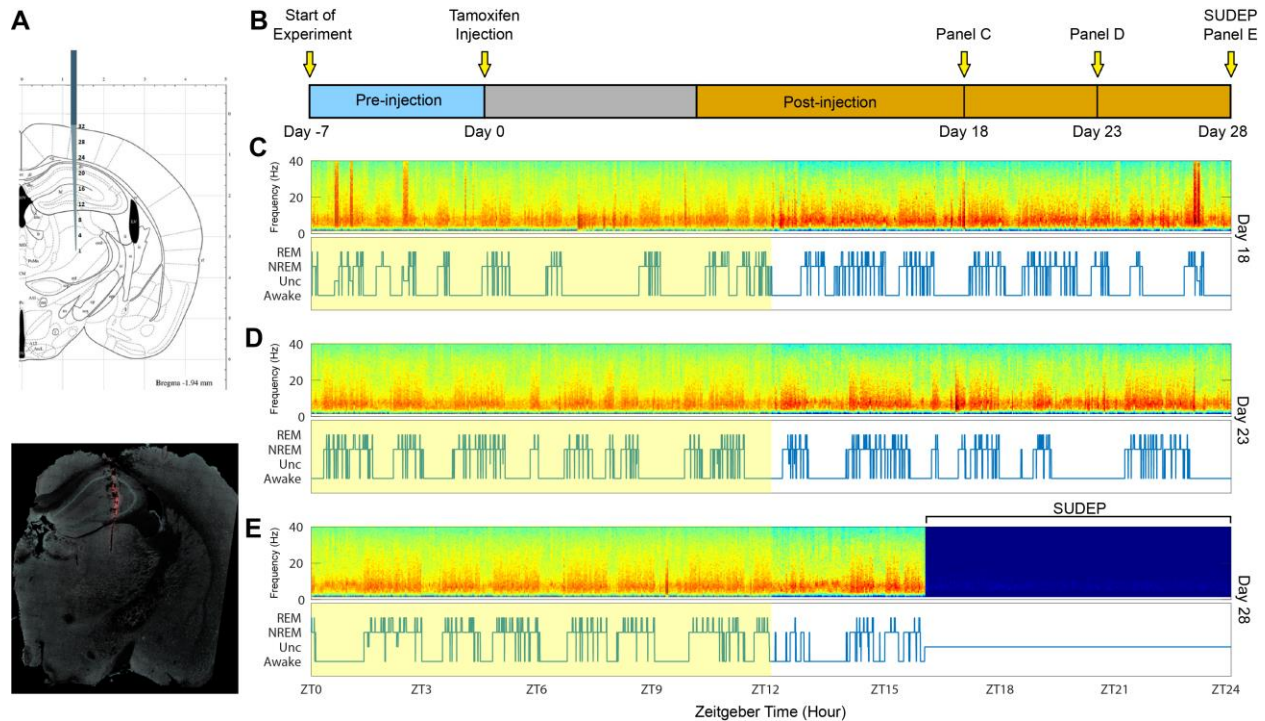
Figure 4.1: Experimental design and recordings in *Scn8a^R1872W* mice

A) Implantation sites targeting the cortex, hippocampus, and thalamus. **B)** Timeline of experimental manipulations and recordings. Tamoxifen injections are marked as Day 0, with 28 days of recording leading up to sudden unexplained death in epilepsy (SUDEP). Animals are continuously recorded for seven days pre-injection, then sent for injections, and recorded post-injections until SUDEP. **C-E)** Sample spectrograms and hypnograms for a 24hr period aligned to zeitgeber time (ZT) for an animal at days 18, 23, and 28 post-injection respectively. (top) Spectrograms representing neural activity from 0-40 Hz. (bottom) Hypnograms indicating sleep state (awake, unclassified, non-REM, REM). Yellow highlights indicate the lights on period from ZT 0-12.

ID	Sex	Total Seizures	Occurrence of SUDEP (Days after Injection)	SUDEP Time of day	Lights manual or automatic	Genotype
Mouse 100	M	1	30 days	Lights on	Manual	$Scn8a^{R1872W}$, Cre-ER$^+$
Mouse 276	F	4	52 days	Lights off	Automatic	$Scn8a^{R1872W}$, Cre-ER$^+$
Mouse 282	F	3	20 days	Lights off	Automatic	$Scn8a^{R1872W}$, Cre-ER$^+$
Mouse 290	F	1	30 days	Lights off	Automatic	$Scn8a^{R1872W}$, Cre-ER$^+$
Mouse 296	F	1	24 days	Lights off	Automatic	$Scn8a^{R1872W}$, Cre-ER$^+$
Mouse 295	M	0	N/A	N/A	Automatic	$Scn8a^{R1872W}$ without Cre
Mouse 313	M	0	N/A	N/A	Automatic	C57BL/6J wildtype

Table 4.1: Features of seizures in experimental animals
Mice were injected with tamoxifen at 4-6 months of age. The time for animals to undergo sudden death after tamoxifen ranged from 20 – 52 days. Lights were automatically on a 12:12 cycle for all mice except for Mouse 100, which was performed manually.

4.3.2 Seizures in *Scn8a^R1872W* mice are often seen first in the hippocampus

Silicon probe recordings across the cortex, hippocampus, and thalamus allow seizures to be carefully examined in each of these regions, helping to identify which of these structures first displays ictal activity. Current source density analysis revealed that the seizures are first detected in the deeper regions of the hippocampus, closer to the stratum lacunosum-moleculare and dentate gyrus, and precede other cortical and thalamic contacts by approximately one second (**Figure 4.2A&B and S4.1A&B**). During this one second period, we observed elevated power in the frequency range of theta and alpha bands of 5-20 Hz in the hippocampal but not the cortical nor thalamic contacts (**Figure S4.2C&G**). These initiations were seen in 3/4 captured seizures which led to SUDEP, and also in 4/5 non-SUDEP seizures (**Figure 4.2C&D**). Furthermore, seconds into the seizure, only the hippocampus transiently displayed this 5-20Hz activity again (**Figure S4.2**). Activity prior to electrocerebral silence varied, with some animals displaying increased activity prior to sudden death (**Figure S4.3**). Overall, these results indicate that seizures in *Scn8a^R1872W* mice may be focal, briefly initiating from or reaching the hippocampus before the cortex and thalamus, with repeated transient activity in all regions until SUDEP.
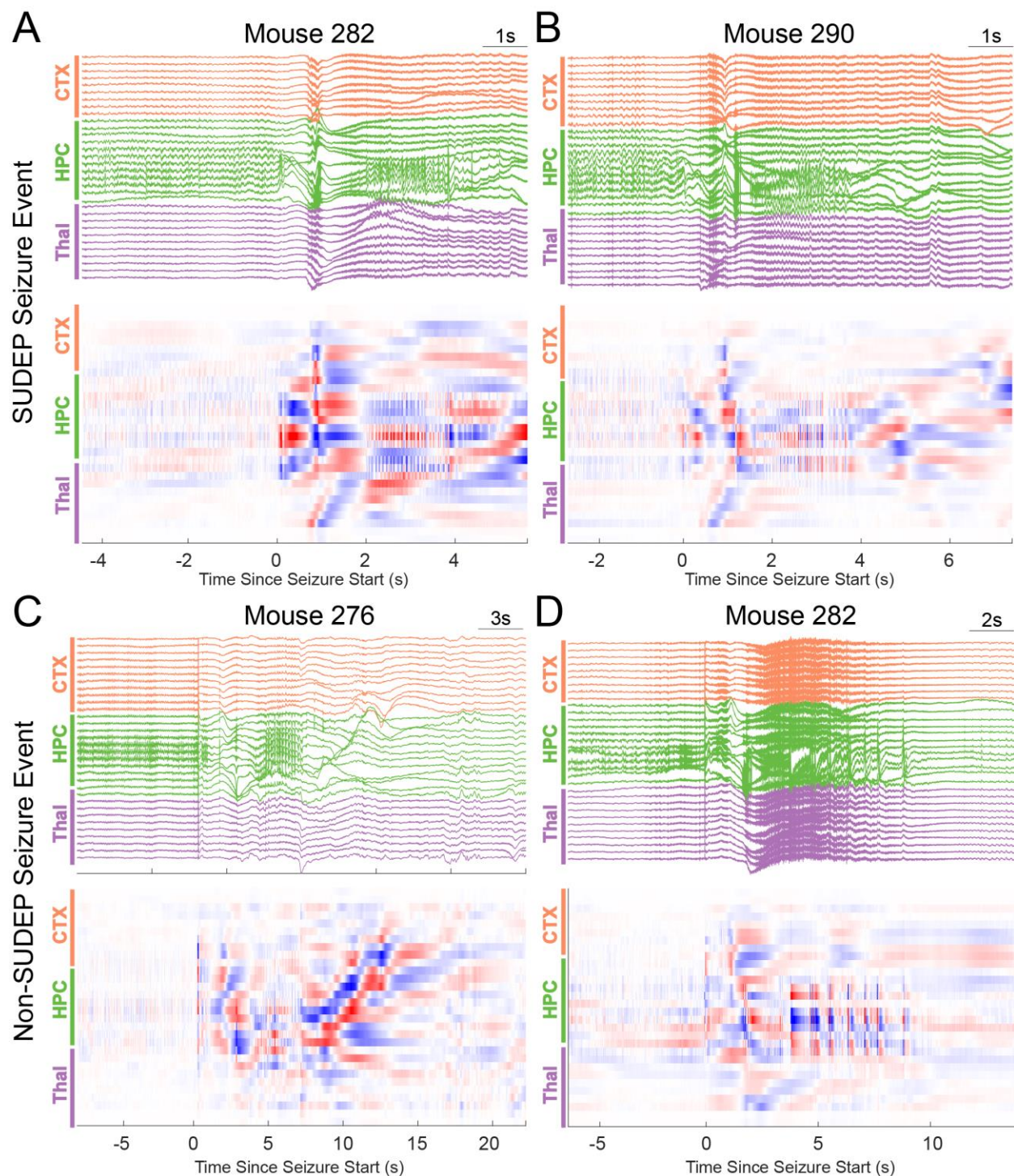
Figure 4.2: Seizures in *Scn8a^{R1872W/+}*,*CAG-Cre-ER* mice are detected in hippocampus one second prior to detection in cortex and thalamus

Electrophysiological recordings at the time of seizures. Time 0 indicates the seizure onset. **A&B)** Seizure event leading to sudden unexpected death in epilepsy (SUDEP) for Mouse 282 and 290. Brain regions are identified as cortex (CTX), hippocampus (HPC), and thalamus (Thal). (top) LFP signal for the 32 linear silicon probe channels recorded during SUDEP. (bottom) Current source density (CSD) of the top panel to identify the source of the seizure onset zone. Red indicates a source and blue indicates a sink. **C&D)** Same as **A&B** but for non-SUDEP seizure events in Mouse 276 and 282.

4.3.3 Interictal discharges are surprisingly long in *Scn8a^R1872W* mice and the event rate may increase before SUDEP

Interictal discharges commonly occur in various types of epilepsies, including temporal lobe epilepsy (Gelinas et al., 2016; Goncharova et al., 2016; Jin et al., 2020; Khan et al., 2010; Spencer et al., 2008). Typically, interictal discharges are short bursts of activity, lasting less than a second (Chvojka et al., 2021; Curtis & Avanzini, 2001). Surprisingly, we observed interictal discharges (IID) lasting 4-6 seconds in two of the five recorded *Scn8a^R1872W* mice (**Figure 4.3**). These IIDs were more likely to occur in the cortical contacts, with some near the superficial hippocampal and superficial thalamic regions. IIDs were sometimes temporally synchronous across brain regions, where we observed cortical-hippocampal, cortical-cortical, and thalamic-thalamic synchrony up to 400 microns apart (**Figure 4.3A&B**).

To determine whether these IIDs have potential as biomarkers of an impending seizure leading to SUDEP, we compared the IID rate of a one hour interval observed 24 hours prior to SUDEP and the one hour interval just before SUDEP. We selected channels where high amplitude IID activity was present in both time periods. The rates of these discharges were higher in the hour prior to seizures, and the number of IIDs more than doubled (**Figure 4.3C&F**). We have not yet assessed IIDs that occur prior to non-SUDEP seizures. These results highlight long duration IIDs as a potential biomarker of *Scn8a^R1872W* epileptic encephalopathy detectable one hour prior to SUDEP. Future investigation will compare IID properties prior to non-SUDEP seizures.
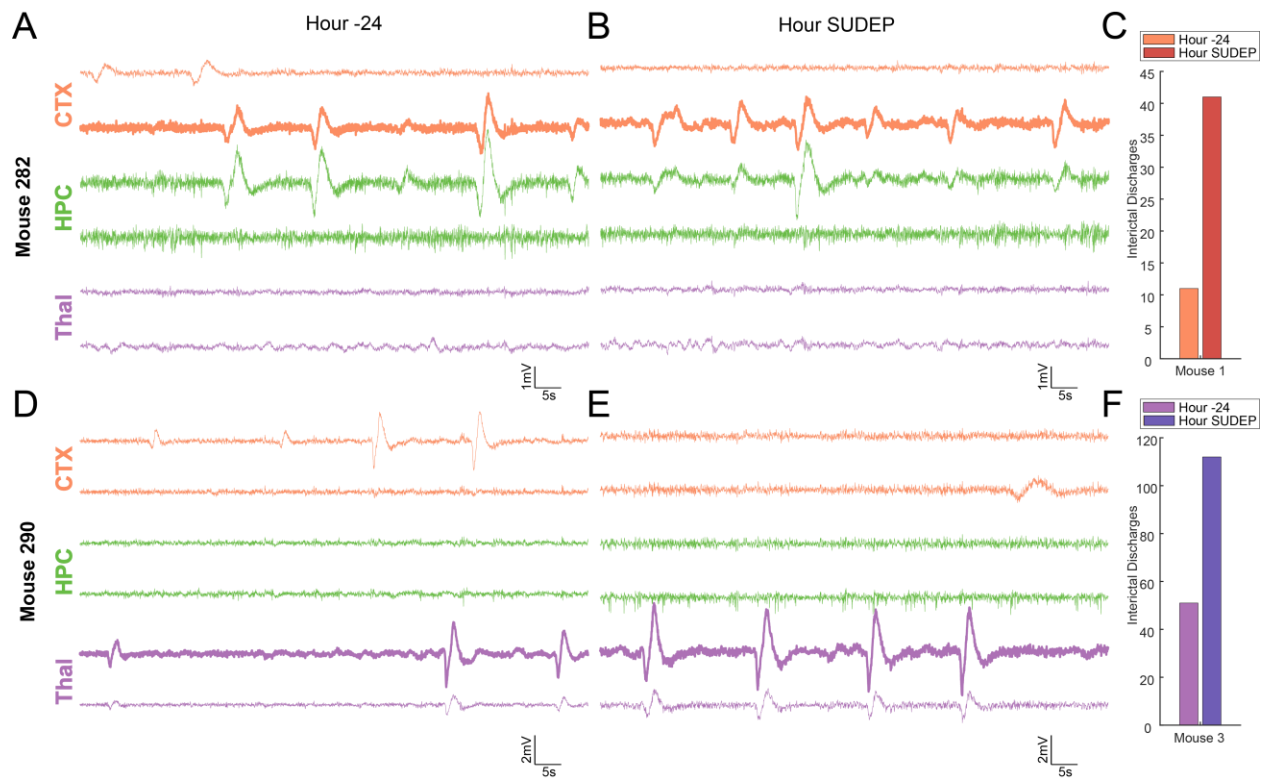
Figure 4.3: Long-lasting interictal discharges in *Scn8a^{R1872W}* mice
Hour long recordings for Interictal discharges (IID) occurring 24 hours prior to SUDEP or 1 hour prior to SUDEP. **A)** Mouse 282 LFP signal for 100 seconds of two channels from the cortex (CTX), hippocampus (HPC), and thalamus (Thal) during an hour long recording 24 hours before SUDEP. **B)** Same as A but in the hour preceding SUDEP. The bolded signal indicates the channel represented in C. Displayed time is limited to 100 seconds in order to visualize IID events. **C)** Total number of detected IID events per 60 minutes during an interval 24 hours prior to seizure and one hour prior to seizure. The number is more than doubled during the one hour prior to seizures. **D-F)** Same as A-C but in Mouse 290.

4.3.4 *Scn8a^{R1872W}* mice may have longer continuous awake epochs

Next, we investigated how sleep architecture and hippocampal SWRs may change as animals approach SUDEP. We scored over 2500 hours of sleep over multiple weeks in 0.5 second intervals for precise investigations of sleep architecture, where sleep states were categorized into awake, rapid eye movement (REM) sleep, and non-REM (NREM) sleep using neural and movement correlates **(Figure 4.4)**. For the analysis of sleep architecture and ripple properties, we included 4 *Scn8a^{R1872W}* and 2 control mice, and excluded 1 *Scn8a^{R1872W}* mouse due to an irregular light:dark cycle (see Methods; Table 4.1). Mice were on a 12:12 lights on/off cycle, where the lights on period is ZT0. A consistent light cycle allows analysis of sleep-wake cycles while controlling for circadian rhythm contributions. As expected, mice were more likely to undergo NREM and REM sleep states during the lights on period (ZT0-12) than lights off (ZT12-24) periods **(Figure 4.4E)**.
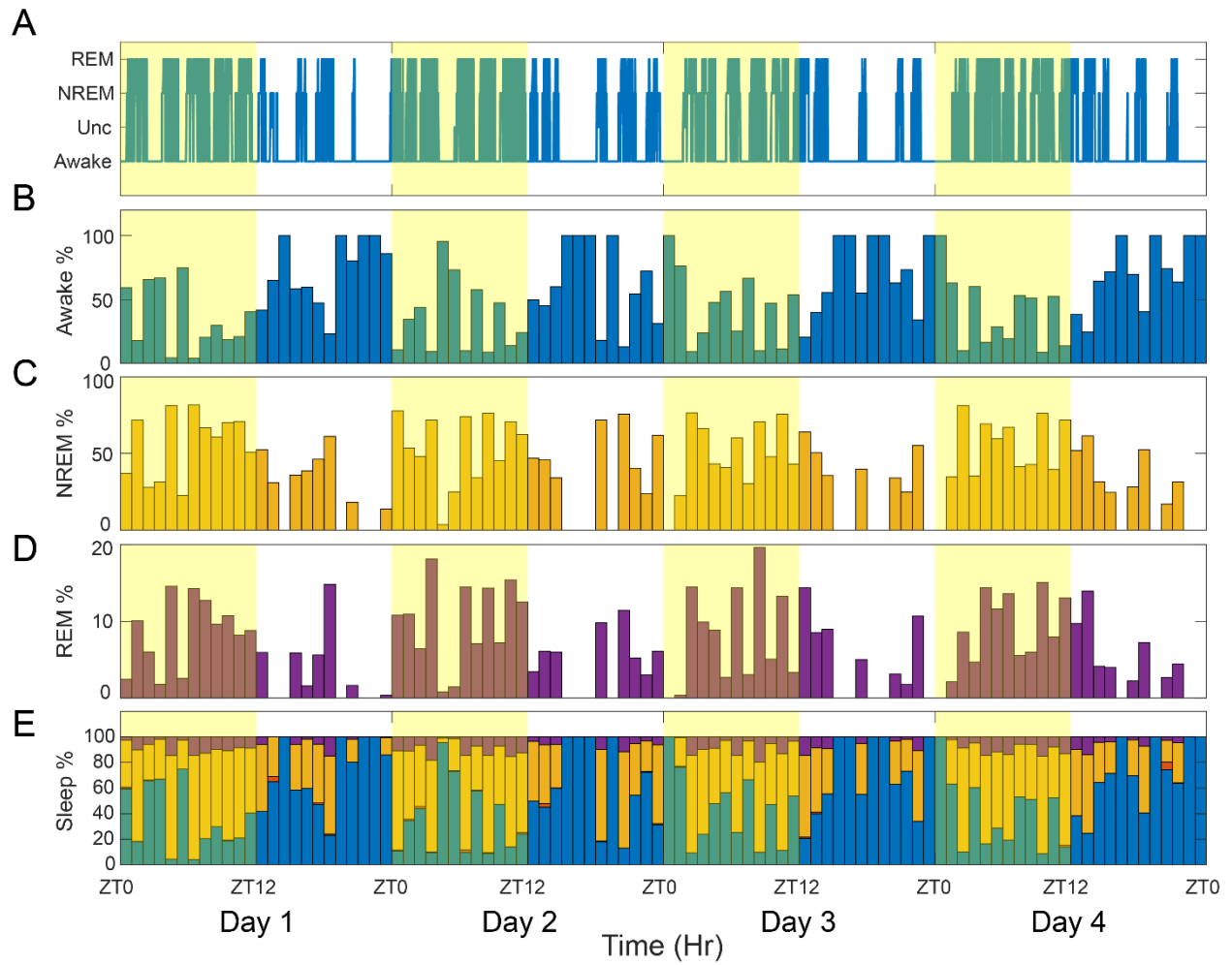
Figure 4.4: Continuous sleep recordings in an *Scn8a* mutant mouse.
Sleep states are precisely scored into awake, non-REM, and REM sleep states. Shown here are 96 hours of continuous data from Mouse 276. **A)** Hypnogram scored at 2Hz. **B-D)** Hourly bar plots of the normalized sleep state percentage in each segment. The animal preferentially sleeps (NREM and REM) during the lights on (ZT 0-12) periods. **E)** Combined data from B-D to indicate the distribution of time spent in the three states, awake (blue or green), NREM sleep (yellow) or REM sleep (red).

Since the time between administration of tamoxiphen and SUDEP ranged from 20 to 52 days (**Table 4.1**), we compared the final 15 days preceding SUDEP. For the animal that underwent SUDEP at 20 days (Mouse 282), we analyzed the last 10 days of available data. We investigated the sleep architecture of $Scn8a^{R1872W}$ mice compared to control animals by assessing the amount of time spent in each sleep state as well as disruptions in circadian rhythms. If circadian rhythm was disrupted, we would observe a phase shift in sleep states. These effects can be visually examined in 2D diagrams of sleep states across days in a 24hr cycle (**Figure 4.5B&F).** We did not observe a shift in the preferred time of day for NREM and REM states in $Scn8a^{R1872W}$ mice compared with controls (**Figure 4.5G&H;** Watson-Williams test, p>0.05**).** We did observe however, that $Scn8a^{R1872W}$ mice displayed longer continuous awake periods than controls during ZT12-24 (**Figure 4.5F and S4.6B).** Continuous analysis of sleep revealed that awake epochs were longer in $Scn8a^{R1872W}$ mice during the lights off period (**Figure 4.5I; Table 4.2**). There were no differences in NREM or REM sleep during the lights on periods.
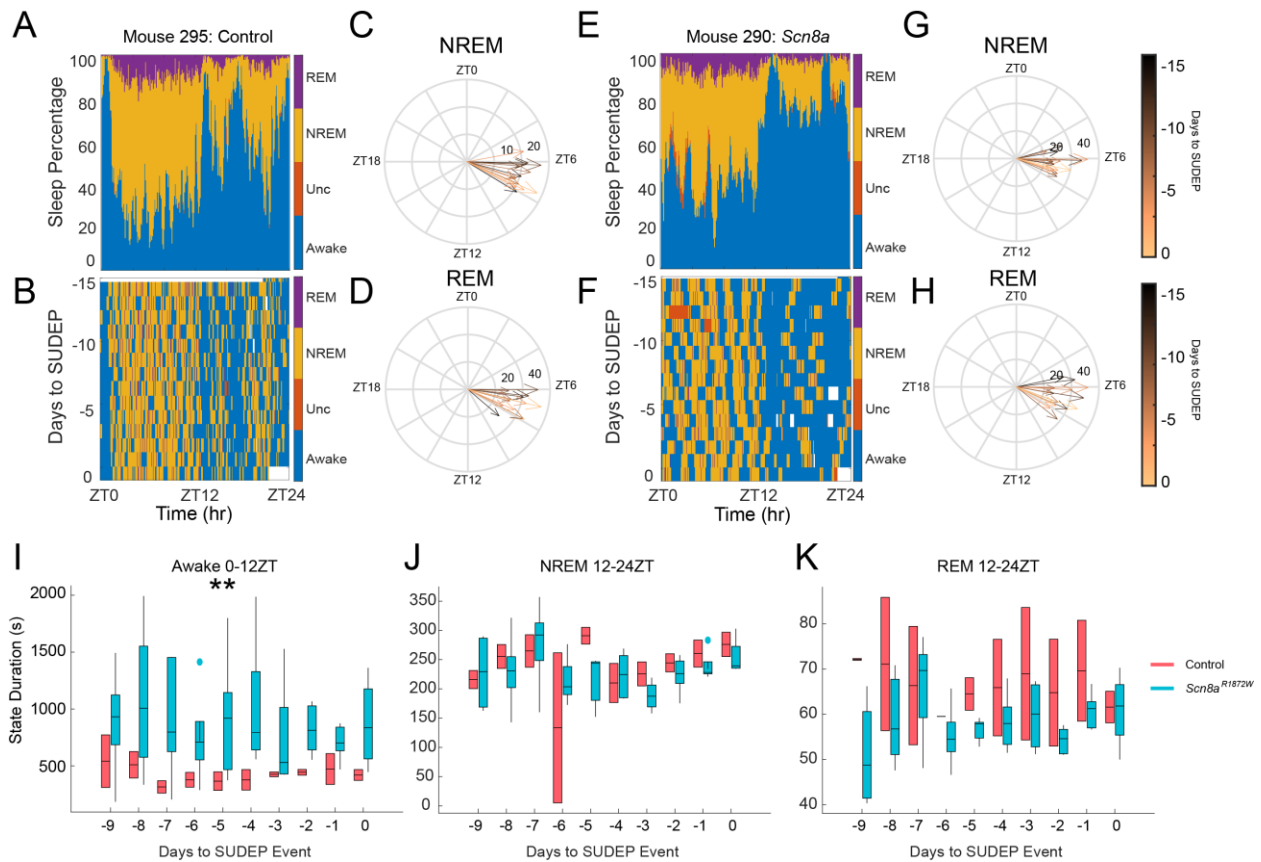
Figure 4.5: Altered sleep architecture in *Scn8a^R1872W* mice before SUDEP

Sleep activity is summarized for 15 days preceding SUDEP. **A)** Summarized sleep distribution in a 24 hour cycle for the 15 days preceding SUDEP in a control animal, showing a strong preference for NREM and REM during ZT 0-12. **B)** Preferred sleep state per day in a 24 hour cycle for control animal. **C&D)** Preferred time of day for NREM and REM sleep in a control animal. There are no substantial time shifts from the first half compared to the last half of the 15 days of recordings (Watson-Williams test; $p > 0.05$). **E-H)** Similar to A-D but in an *Scn8a^R1872W* mutant mouse. I-K) Sleep epoch durations for awake, NREM, and REM during lights off for awake, and lights on for NREM and REM states. Linear mixed effects models revealed that *Scn8a^R1872W* mice have significantly longer continuous awake bouts than control animals, but this is not observed for NREM and REM (Table S5.1; $p < 0.01$).

	Variable	Estimate	SE	t-statistic	df	p-value	lower	upper
Awake	Intercept	986.12	114.58	8.61	58	5.9e-12	756.76	1215.5
	Gene	-561.31	197.41	-2.84	58	0.006	-956.46	-166.16
NREM	Intercept	238.47	9.74	24.49	56	1.3e-31	218.96	257.98
	Gene	-0.75	15.53	-0.048	56	0.96	-31.85	30.36
REM	Intercept	59.82	3.06	19.55	55	1.9e-26	53.68	65.95
	Gene	7.41	5.29	1.40	55	0.17	-3.19	18.02

Table 4.2: Linear mixed model parameter estimates for sleep epochs

This table details the multilevel models ran to assess the relationship of sleep state durations and the mutant *Scn8a^{R1872W}* gene. We fit a multilevel model individually to each sleep state (awake, NREM, REM) with Duration as the DV, Gene as the IV, and where Time and Animal were random effects. Time was binned at 12 hour intervals.

4.3.5   Sleep architecture does not change approaching SUDEP

Earlier we described interictal discharges which occurred more often as $Scn8a^{R1872W}$

animals approached the final seizure leading to SUDEP (**Figure 4.3**). We therefore examined

whether changes in sleep architecture were predictive of SUDEP. Data from the last 15 days of

recordings from $Scn8a^{R1872W}$ mice were utilized in these analyses (see Methods). Using a linear

mixed model, we did not observed changes in the total time spent in awake, NREM, or REM as

$Scn8a^{R1872W}$ animals approached SUDEP **(Figure 4.6A-C; Table 4.3).** Furthermore, we did not

see any changes in sleep fragmentation **(Figure 4.6D; Table 4.4)**. These results may indicate

that changes in sleep architecture are occurring prior to the 15 days assessed in this analysis.
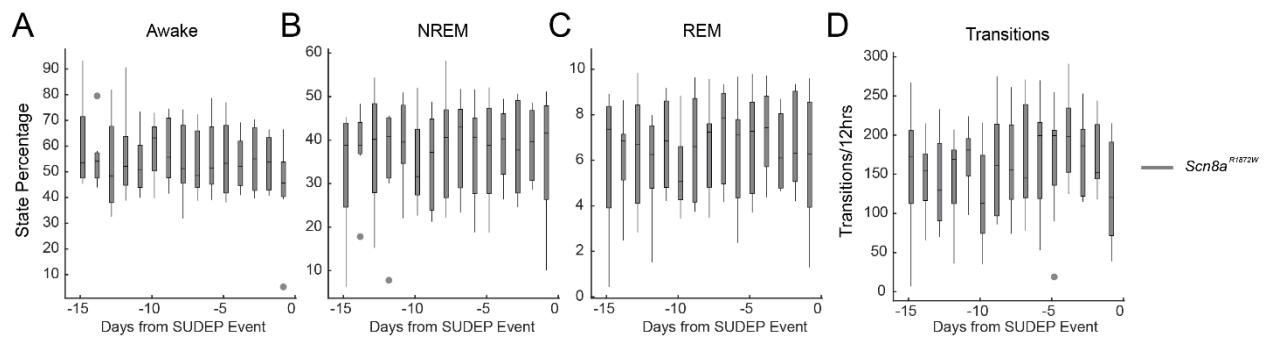
Figure 4.6: Sleep architecture does not change during the 15 days before SUDEP
A-C) Sleep percentage for awake, NREM, and REM sleep states during 0-24ZT in the 15 days preceding SUDEP. **D)** Total number of transitions every 12 hours, including any changes between awake, unclassified, NREM, and REM states. Linear mixed effect models did not reveal any significant changes across time in neither the control nor *Scn8a* mutant mice (Table S5.2).

Variable	Estimate	SE	t-statistic	df	p-value	lower	upper
Intercept	-3.61	13.65	-0.26	96	0.79	-30.7	23.48
Awake Percent	-0.044	0.14	-0.32	96	0.75	-0.32	0.23
NREM Percent	-0.12	0.16	-0.72	96	0.47	-0.44	0.20
REM Percent	0.49	0.48	1.02	96	0.31	-0.46	1.44

Table 4.3: Linear mixed model parameter estimates for sleep percentage predictors of SUDEP

This table details the multilevel models ran to assess the relationship of sleep state changes as animals approached SUDEP in *Scn8a*^{R1872W} mice. We fit a multilevel model with Time to SUDEP as the DV, percent spent in each sleep state as the IV, and animal as a random effect for intercept. Time was binned at 12 hour intervals.

Variable	Estimate	SE	t-statistic	df	p-value	lower	upper
Intercept	-7.98	1.24	-6.44	98	4.4e-9	-10.44	-5.52
Transitions	0.0036	0.0057	0.63	98	0.53	-0.0077	0.015

Table 4.4: Linear mixed model parameter estimates for sleep transition predictors of SUDEP

This table details the multilevel models ran to assess the relationship of sleep fragmentation changes as animals approached SUDEP in *Scn8a*^{R1872W} mice. We fit a multilevel model with Time to SUDEP as the DV, number of sleep state transitions as the IV, and animal as a random effect for intercept. Time was binned at 12 hour intervals.

4.3.6 SWR duration and frequency slightly decrease approaching SUDEP

Finally, we assessed whether properties of SWRs change during the 15 days prior to

SUDEP. We looked at amplitude, duration, rate, and peak frequency. Similar to the sleep

analyses, we utilized the last 15 days of data from each animal (see Methods). Using linear

mixed models we observed a small, but significant change in ripple duration and frequency

(Figure 4.7C&E; Table 4.5). However, paired signed rank tests did not reveal a significant

change from day -15 to day 0, although this may be limited by a low sample size (n=5).
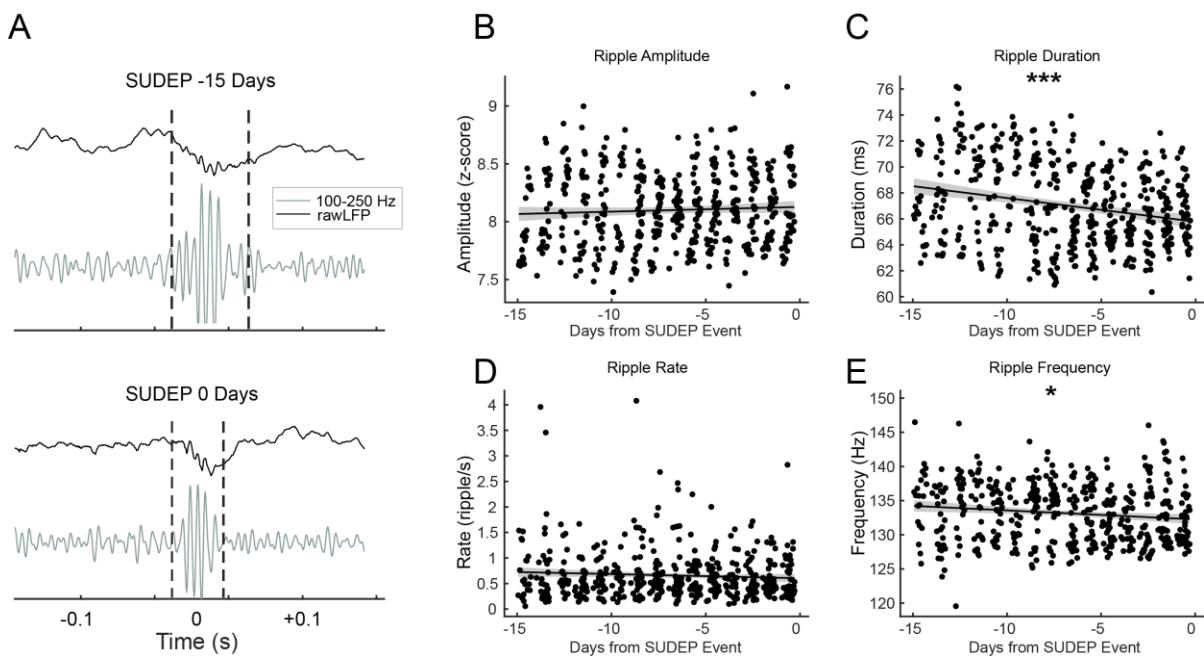
Figure 4.7: SWR duration and frequency may decrease approaching SUDEP
A) Example hippocampal sharp wave ripple, showing that the ripple duration is lower at Day 0 immediately preceding SUDEP, compared to Day -15 before SUDEP. B-E) Hippocampal sharp wave ripple properties from 2-10ZT in *Scn8a^{R1872W}* mice in the 15 days preceding SUDEP. We assessed ripple amplitude, duration, rate, and peak ripple frequency. Linear mixed effect models revealed that SWR duration and peak frequency decrease as animals approach SUDEP (Table S5.3), although these differences are not observed using paired t-tests between Day -15 and 0 (p>0.05).

Variable	Estimate	SE	t-statistic	df	p	lower	upper
Intercept	-6.63	0.58	-11.44	391	2.3e-26	-7.77	-5.49
Amplitude	0.02	0.24	0.08	391	0.934	-0.46	0.50
Duration	-1.18	0.22	-5.39	391	1.2e-07	-1.60	-0.75
Frequency	-0.01	0.21	-0.07	391	0.95	-0.42	0.39
Rate	-0.45	0.21	-2.09	391	0.037	-0.87	-0.03

Table 4.5: Linear mixed model parameter estimates for ripple predictors of SUDEP

This table details the multilevel models ran to assess the relationship of ripple property changes as animals approached SUDEP in $Scn8a^{R1872W}$ mice. We fit a multilevel model with Time to SUDEP as the DV, ripple properties as the IVs, and animal as a random effect for intercept. Time was binned in hourly hour intervals. Data was limited to ZT2-10 to capture high quality ripples. Ripple properties were standardized within animals.

4.4 Discussion

In this study, we examined and characterized how seizures manifest in *Scn8a* encephalopathy by continuously monitoring electrophysiological signals across multiple regions until the occurrence of sudden unexpected death in epilepsy (SUDEP). Using conditional *Scn8a^{R1872W}* adult mutant mice with a linear silicon probe implant spanning the cortex, hippocampus, and thalamus, we found that the earliest seizure activity was observed in the hippocampus (**Figure 4.2 and S4.1**). Seizure activity in the hippocampus preceded the cortex and thalamus by approximately one second, with transiently increased 5-20Hz activity (**Figure S4.2**), and this phenomenon was observed in both SUDEP and non-SUDEP inducing seizures (**Figure 4.2**). Furthermore, we observed uniquely long 4 second interictal discharges (IID) which occurred more often as animals approached SUDEP (**Figure 4.3**). From our assessments of sleep patterns, we did not observe any shifts in the preferred time for NREM nor REM (**Figure 4.5G&H**), but we report that *Scn8a^{R1872W}* mice have longer continuous awake bouts than control animals, potentially indicating higher prolonged states of arousal (**Figure 4.5I**). These differences may develop early after tamoxifen injection, as we did not observe changes in sleep dynamics predictive of SUDEP within the 15 days prior to SUDEP (**Figure 4.6**). Instead, hippocampal SWR duration and peak frequency slightly decrease as animals approach SUDEP (**Figure 4.7**). Therefore, among the regions examined, the hippocampus displays the earliest ictal activity and may be useful for seizure prediction in *Scn8a^{R1872W}* mice.

Determining how and when seizures occur in *SCN8A* encephalopathy would permit more precise and earlier interventions. Patients with GOF *SCN8A* mutations present with both focal and generalized epilepsy (Johannesen et al., 2021; Kong et al., 2015; Podkorytova et al., 2022; Takahashi et al., 2015). Furthermore, selective reduction of a floxed allele of Nav1.6 in the

hippocampus is sufficient to reduce the number of seizures resulting from picrotoxin (Makinson et al., 2014). Nav1.6 is the voltage gated sodium channel most associated with persistent sodium currents (I_{NaP}) (Curtis & Avanzini, 2001; Raman et al., 1997; Wengert & Patel, 2021) and $Scn8a^{R1872W}$ mice have greater I_{NaP} (Bunton-Stasyshyn et al., 2019; Meisler, 2019). Increased persistent sodium current increases the susceptibility to depolarization block (Wengert, Miralles, et al., 2021), suggesting that depolarization block of interneurons in the hippocampus may play a role in seizures in $Scn8a^{R1872W}$ mice.

We report unique long four second interictal discharges (IID) which occur more often in the final hour before SUDEP compared with the day before SUDEP (**Figure 4.3**). IIDs are high amplitude events which typically last less than 500ms, where the sharp depolarization arises from glutamatergic transmission involving calcium and sodium currents followed by hyperpolarization from GABAergic interneurons (Amakhin et al., 2016; Chvojka et al., 2021; Curtis & Avanzini, 2001; Gilles Huberfeld et al., 2011). The role of IIDs in epileptogenesis and seizure prediction are still debated (Avoli et al., 2006; Curtis & Avanzini, 2001; Karoly et al., 2016; Stafstrom, 2007; Wengert & Patel, 2021). Contrary to our results, some studies suggest that IIDs are neuroprotective against seizures, and that fewer IIDs are seen immediately before seizure events (Curtis & Avanzini, 2001). However, longitudinal multi-day assessments of seizure risk and interictal events revealed that seizure events also often occurred near the peak rate of interictal events in both rodents and humans (Baud et al., 2019; Leguia et al., 2021). Furthermore, the relationship of interictal activity and *SCN8A* encephalopathy is currently unknown, and fatal seizures may manifest differently from typical seizures (Wagnon et al., 2015; Wengert, Wenker, et al., 2021). This observation highlights the need to characterize IIDs according to the underlying seizure mechanisms.

Given the close relationship of sleep disorders and epilepsy (Garg et al., 2022; Manni & Terzaghi, 2010; Peter-Derex et al., 2020), and the severity of *SCN8A* encephalopathy, we expected to see clear changes in sleep architecture. However, *Scn8a^{R1872W}* do not display alteration in sleep architecture in the 15 days leading to the fatal seizure (**Figure 4.5**). Instead, sleep differences compared to controls manifested as longer periods of wakefulness specifically during active lights off periods (**Figure 4.4I**), suggesting that *Scn8a^{R1872W}* sleep circuits are impaired in the transition from awake to sleep states. Our findings were only revealed after accounting for circadian rhythm and looking specifically during the active period of day, potentially explaining why previous work did not observe sleep disturbances in GOF *SCN8A* patients (Gardella et al., 2018). These longer awake epochs during the lights off phase may be in alignment with the decreased awake states in an *Scn8a$^{med-jo/+}$* LOF mouse model (Papale et al., 2010) as well increased awake states in the *Scn1a$^{R1648H/+}$* LOF mouse model (Martin et al., 2010). Furthermore, we observed lower SWR duration and peak frequency as animals approached the SUDEP event (**Figure 4.7**), where the combination of lower frequency and duration would imply less time for neuronal ensembles to replay behaviorally-relevant sequences, potentially impairing memory consolidation (Buzsáki, 2015). However, there are a few limitations to these assessments: 1) We observed awake state differences between *Scn8a^{R1872W}* and controls, but could not capture when these differences began to evolve (**Figure 4.4**). This indicates that the 10 days of recordings immediately following tamoxifen injections may be crucial to determine the time of development of the abnormality in mutant mice. 2) We lacked a sufficient number of controls to permit direct comparisons between *Scn8a^{R1872W}* and controls for SWR properties. 3) We need more recordings in the period post-surgery and pre-injection to observe habituation and stabilization of sleep architecture. There may be sleep

architecture confounds immediately resulting from surgical implantation that would stabilize when given another week of rest.). In summary, these differences in sleep and hippocampal SWR require further investigation beyond the scope of this dissertation.

4.5 Supplementary Figures and Tables
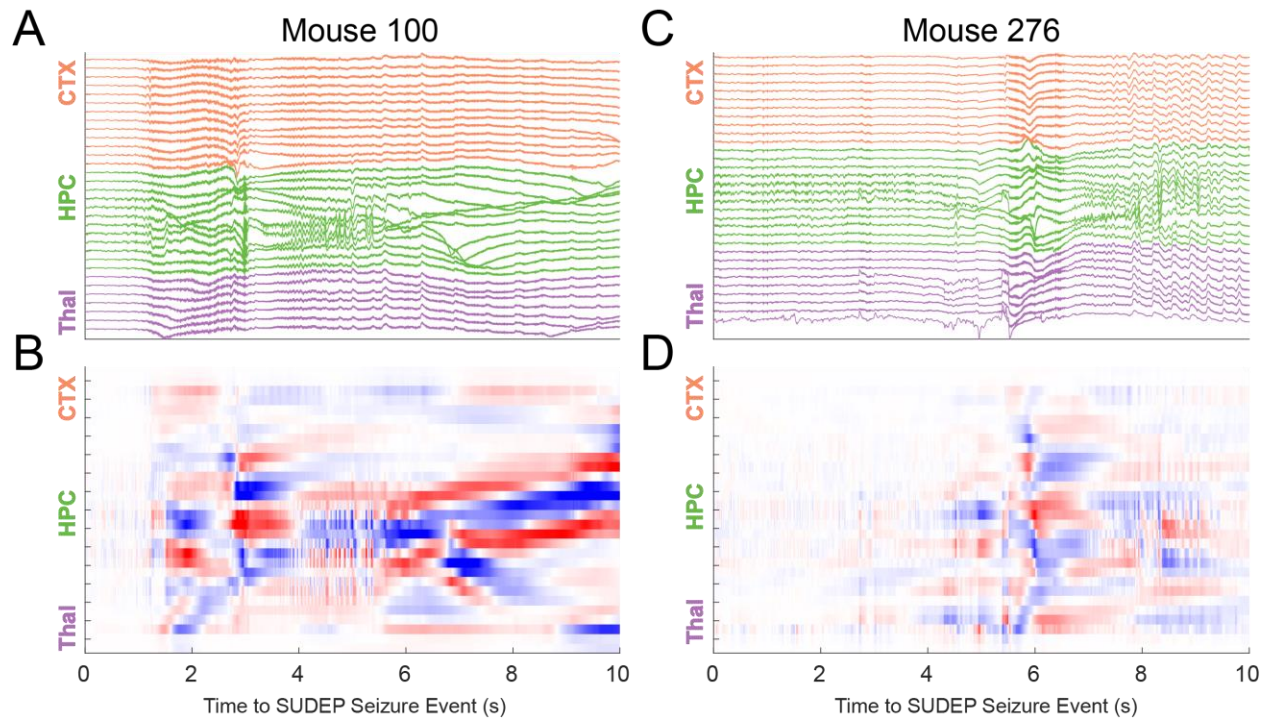
Supplementary Figure 4.1: SUDEP for remaining animals
Electrophysiological recordings at the time of seizures, similar to Figure 4.2. **A&C)** Seizure event leading to sudden unexpected death in epilepsy (SUDEP) for Mouse 100 and 276. Brain regions are identified as cortex (CTX), hippocampus (HPC), and thalamus (Thal). LFP signal for the 32 linear silicon probe channels recorded during SUDEP. **B&D)** Current source density (CSD) of the A&C to identify the source of the seizure onset zone. Red indicates a source and blue indicates a sink.
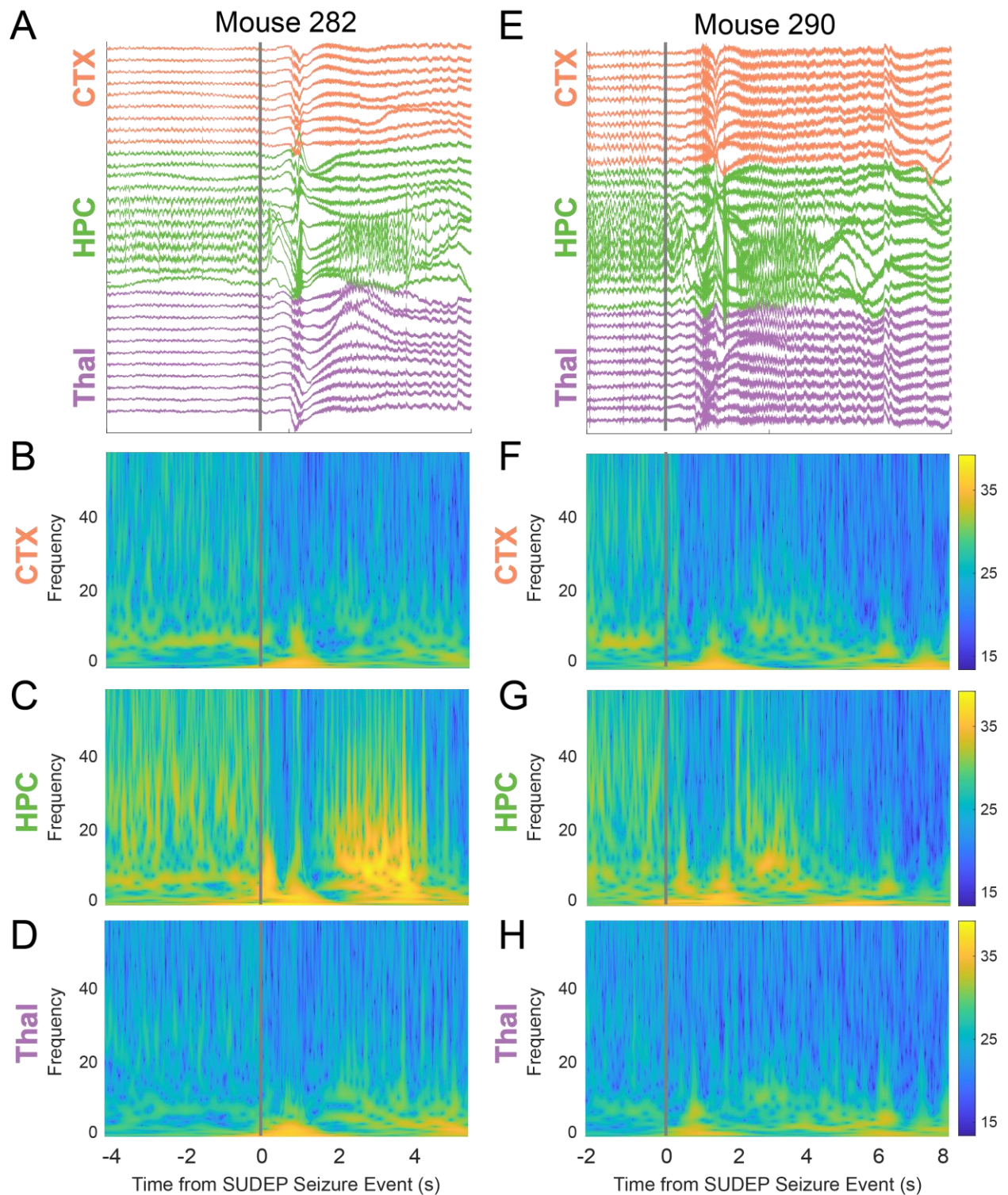
Supplementary Figure 4.2: SUDEP spectral components from the cortex, hippocampus, and thalamus

A) LFP activity of the 32 channel linear silicon probe at the time of the SUDEP seizure event for Mouse 282. **B-D)** Spectrograms from 0-60Hz for channels selected from the cortex, hippocampus, and thalamus. **E-H)** Same as A-D but for Mouse 290
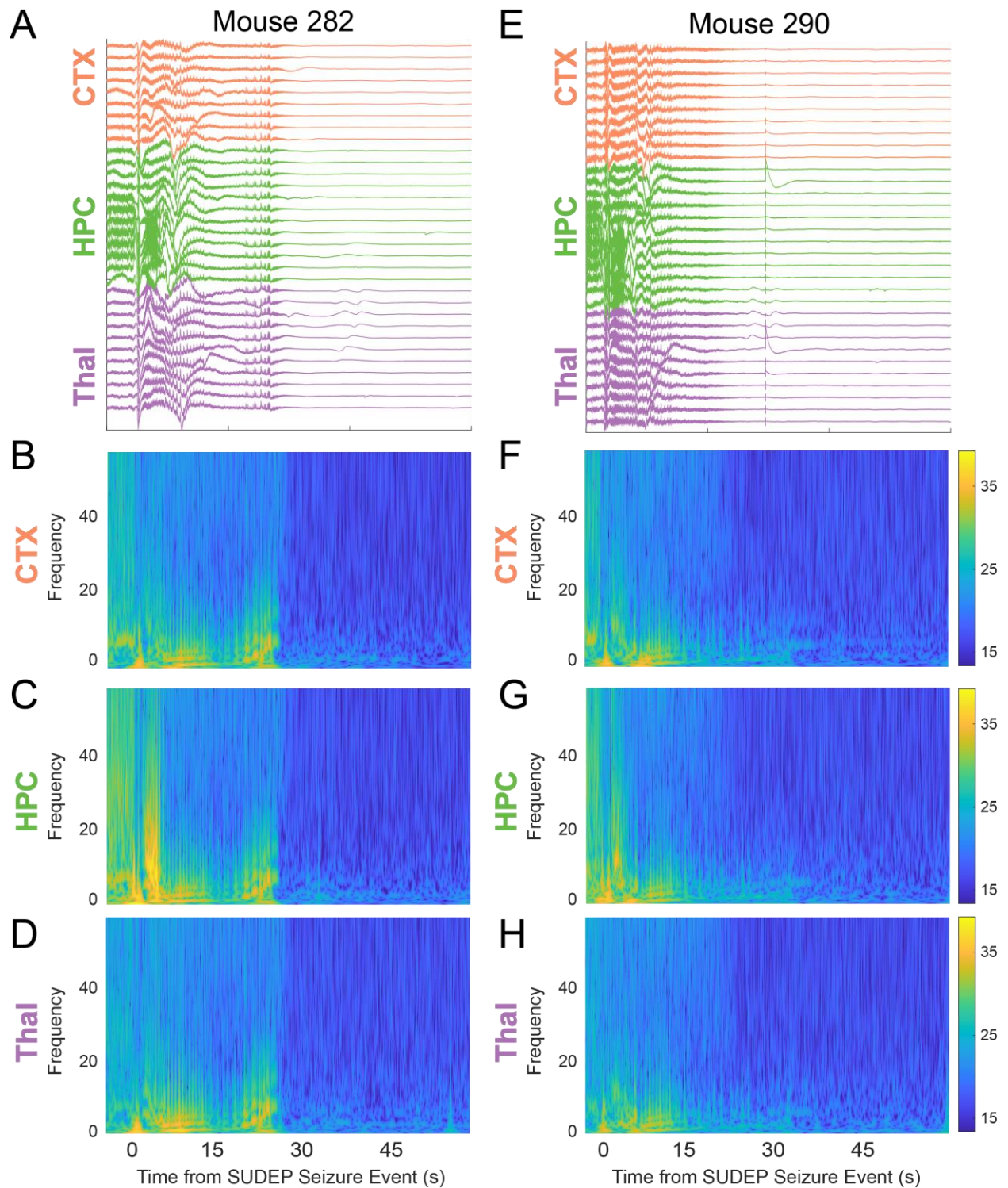
Supplementary Figure 4.3 SUDEP spectral components until electrocerebral silence
Similar to Figure S4.2 but for 60s, showing activity during electrocerebral silence. **A)** LFP activity of the 32 channel linear silicon probe at the time of the SUDEP seizure event for Mouse 282. **B-D)** Spectrograms from 0-60Hz for channels selected from the cortex, hippocampus, and thalamus. **E-H)** Same as A-D but for Mouse 290
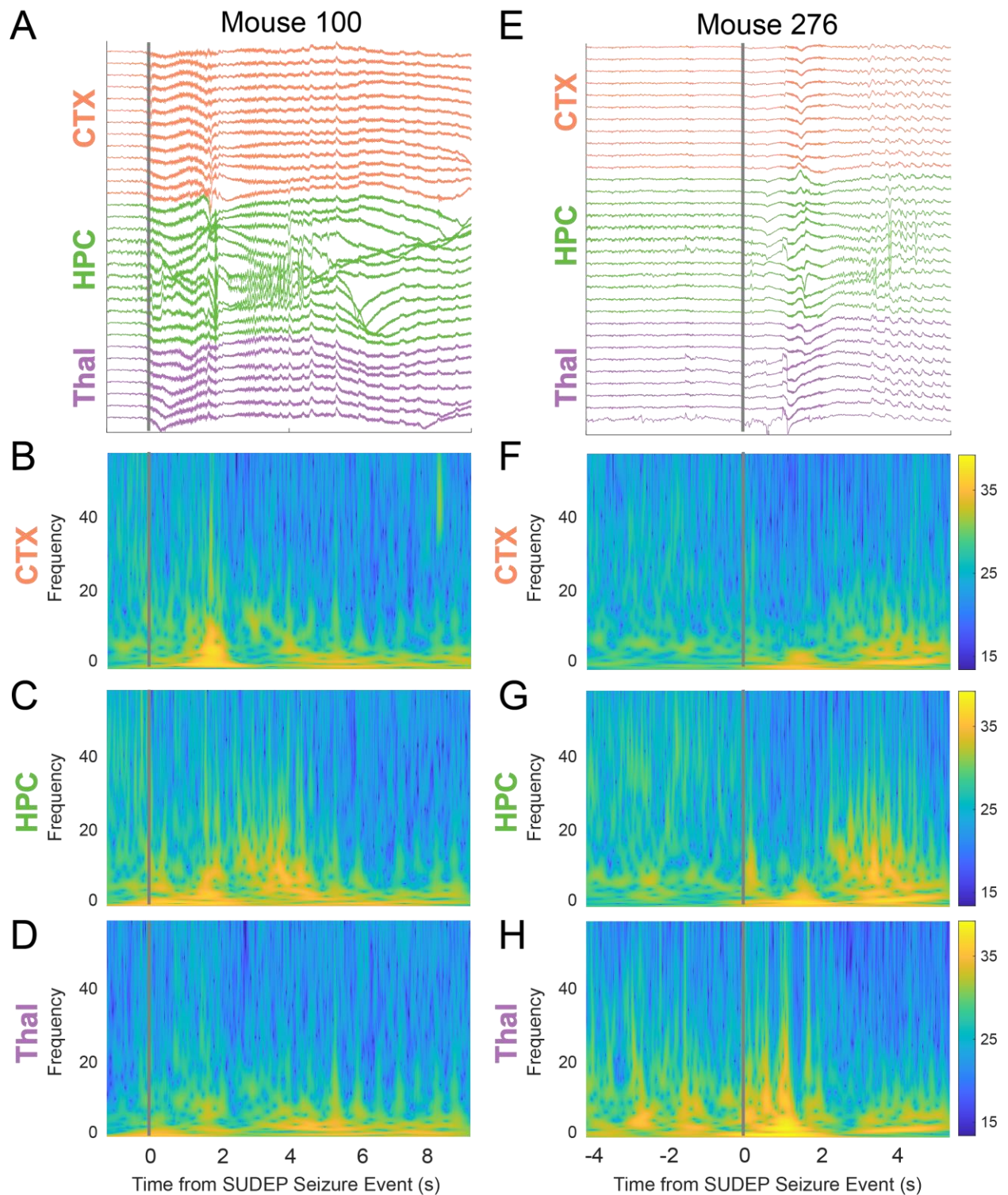
Supplementary Figure 4.4: SUDEP spectral components from the cortex, hippocampus, and thalamus for Mouse 100 and 276

A) LFP activity of the 32 channel linear silicon probe at the time of the SUDEP seizure event for Mouse 100. **B-D)** Spectrograms from 0-60Hz for channels selected from the cortex, hippocampus, and thalamus. **E-H)** Same as A-D but for Mouse 276
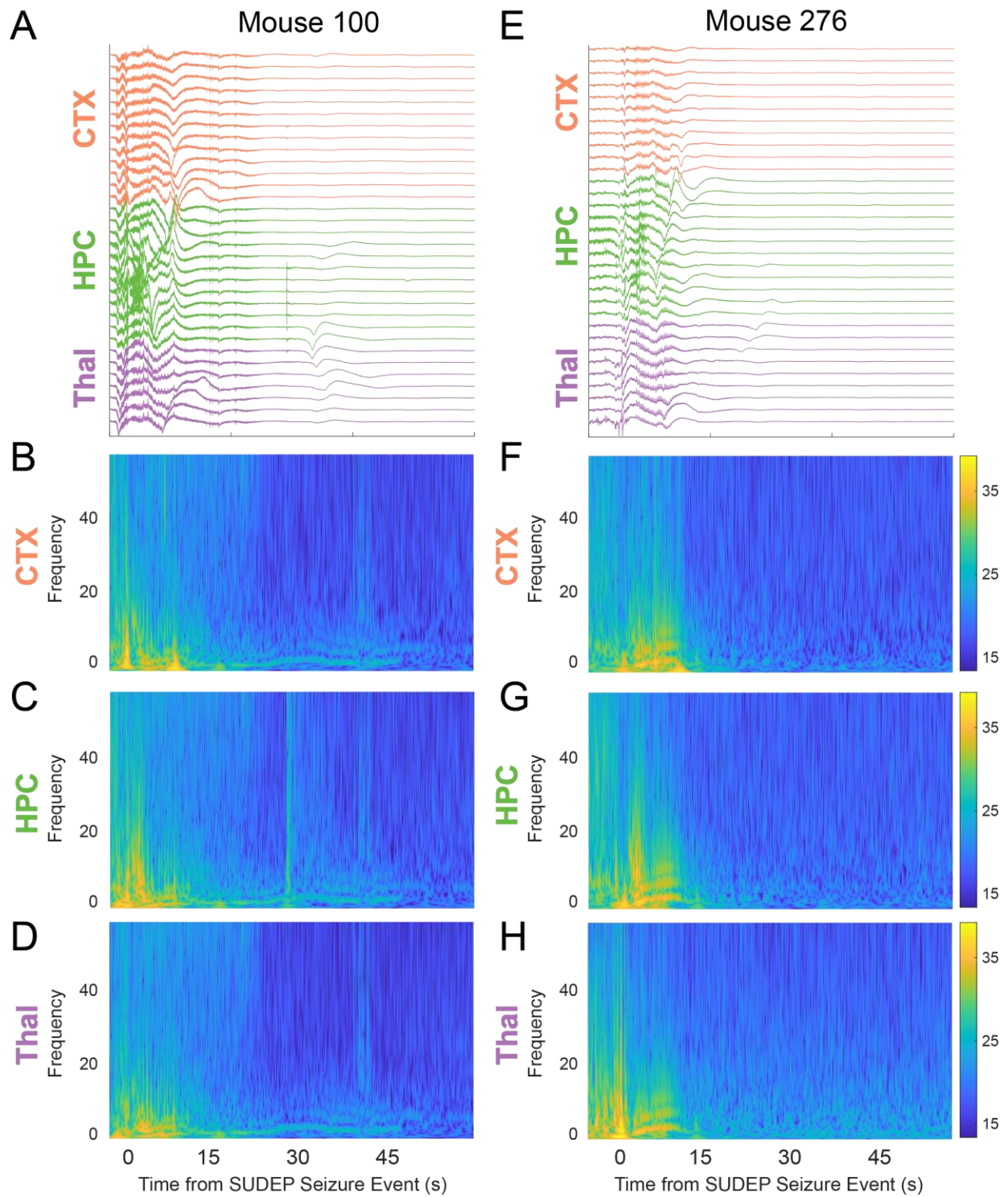
Supplementary Figure 4.5: SUDEP spectral components until electrocerebral silence for Mouse 100 and 276

Similar to Figure S4.4 but for 60s, showing activity during electrocerebral silence. **A)** LFP activity of the 32 channel linear silicon probe at the time of the SUDEP seizure event for Mouse 100. **B-D)** Spectrograms from 0-60Hz for channels selected from the cortex, hippocampus, and thalamus. **E-H)** Same as A-D but for Mouse 276
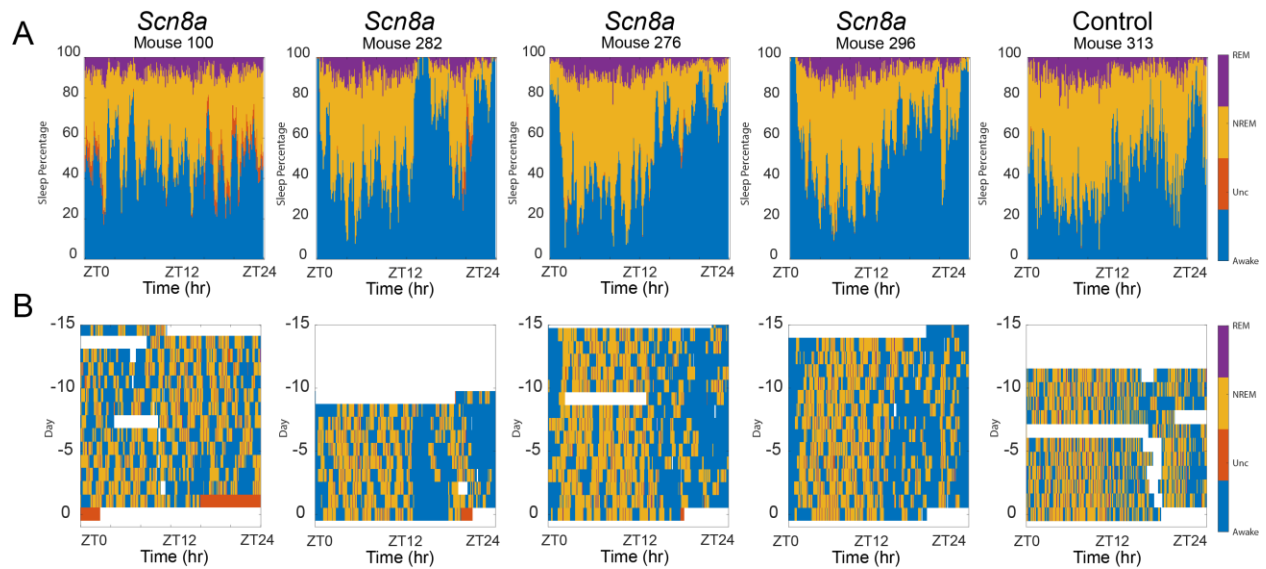
Supplementary Figure 4.6: Sleep architecture for all remaining mice 15 days preceding SUDEP

Similar to Figure 4.5 but for the remaining animals. **A)** Summarized sleep distribution in a 24 hour cycle for the 15 days preceding SUDEP in a control animal, showing a strong preference for NREM and REM during ZT 0-12. **B)** Preferred sleep state per day in a 24 hour cycle.

107
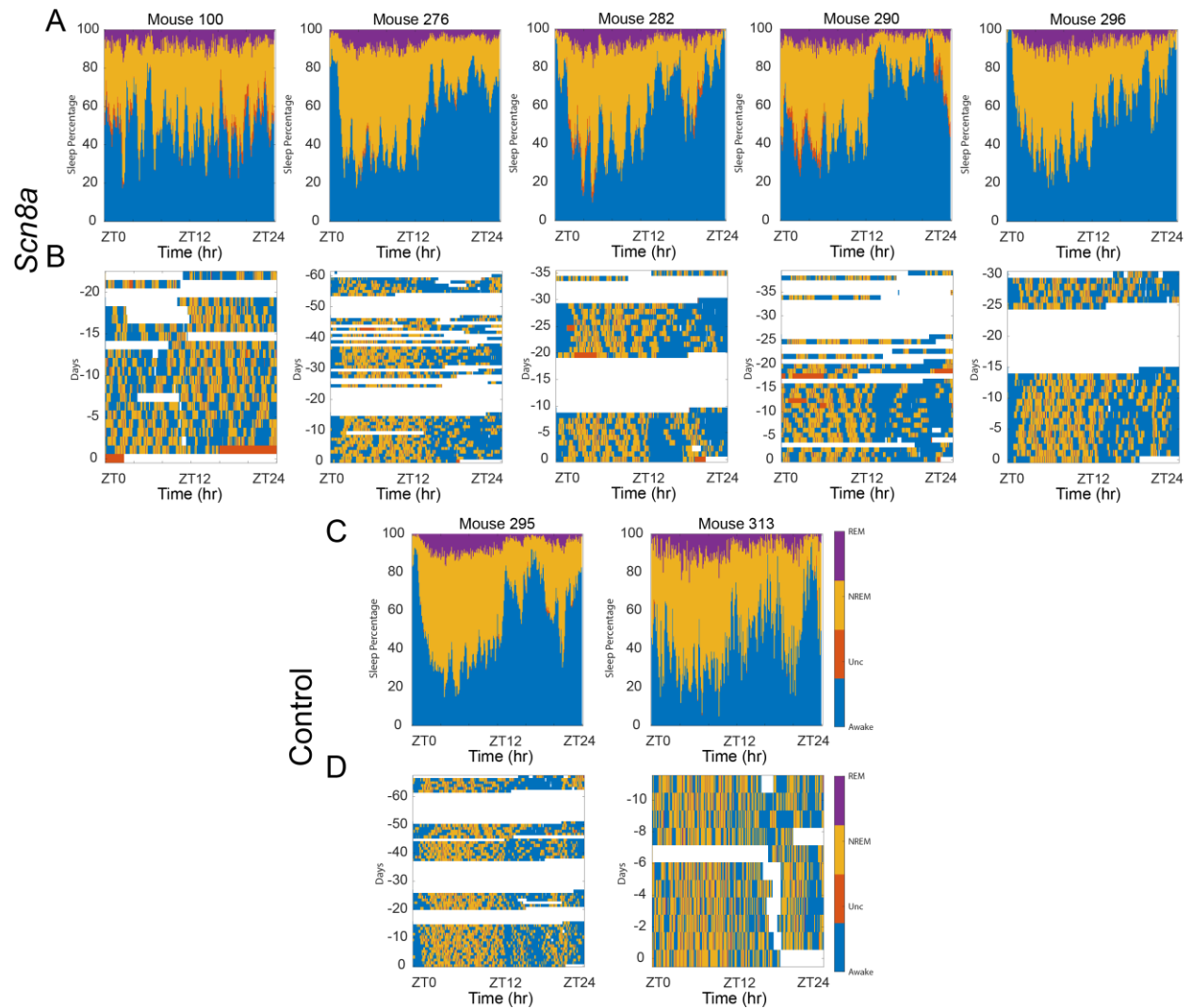
Supplementary Figure 4.7: Sleep architecture for all mouse recordings
Similar to Figure S4.6 but for all available recordings. Some animals like Mouse 276 and 295 had continuous recordings for over 60 days. White regions indicate missing data, where the large 10 day white space corresponds to the tamoxifen injection period **A)** In *Scn8a* mice, Summarized sleep distribution in a 24 hour cycle for the 15 days preceding SUDEP in a control animal, showing a strong preference for NREM and REM during ZT 0-12**. B)** Preferred sleep state per day in a 24 hour cycle. **C&D)** Same as A&B but in the two control animals

Chapter 5: Software Solutions Developed to Expedite Neural Data Science

Danny Siu, Megha Ghosh, Aditya Singhvi, Omar J. Ahmed

5.1   Abstract

Hardware and techniques for in vivo electrophysiological recordings continue to rapidly

advance, and cheaper storage has provided the opportunity for researchers to record tremendous

amounts of electrophysiological data. These novel techniques either necessitate recordings with

greater spatial resolution with more channels using probes such as Neuropixels, or continuous

24/7 recordings to capture subtle changes in behavior and neural circuits. However, without the

development of scalable, standardized analysis pipelines, the volume of data may far outpace the

capacity to analyze the data and make scientific progress. Here, I describe the software solutions

to handle the continually expanding experiments in the Omar Lab.

5.2   Methodology
5.2.1   Process to handle 24/7 electrophysiological data

Depending on the type of experiment and implant in Chapter 4, each mouse yielded up to

600 GB of data per 24 hour recording, or ~7MB/s. Handling this enormous volume of data

necessitated scalable compute and storage resources, a centralized storage system, as well as a

standardized pipeline to ingest and systematically pre-process the data. Indeed, since we required

at least 10GB of memory per 100GB of raw data, having a service on demand that allowed

dynamic memory allocation was advantageous rather than relying on local computes with

hardware constraints. Furthermore, our pre-processing pipeline to down-sample, transform, and

analyze the electrophysiological and video data requires approximately 3hrs per 100GB of raw data. It would be advantageous to have a simple no-code system which allows non-computational users to begin the analysis process immediately following data collection.

To solve these big data problems, we utilized the University of Michigan's high performance computing (HPC) cluster *Great Lakes* as well as their centralized storage solution *Turbo*. We utilized an extract, load, transform (ELT) pipeline process, where data is first transferred onto *Turbo* before it undergoes the pre-processing pipeline (**Figure 5.1**). At each step, data monitoring is essential to visualize the health and quality of the data. In each stage of the processing pipeline, graphs of the electrophysiological data were made available using various Google products (Google Drive, Google Sheets). Pipeline users are simply required to upload the data to our shared storage system and enter the necessary metadata of each experiment in a Google Sheet. Jobs for analysis are automatically queried, collected, and submitted bi-hourly from 2pm to 2am. To ensure that the system can be maintained, I implemented data contracts, data monitoring, staging environments, unit testing, and an API for new developers to add more data processing modules.
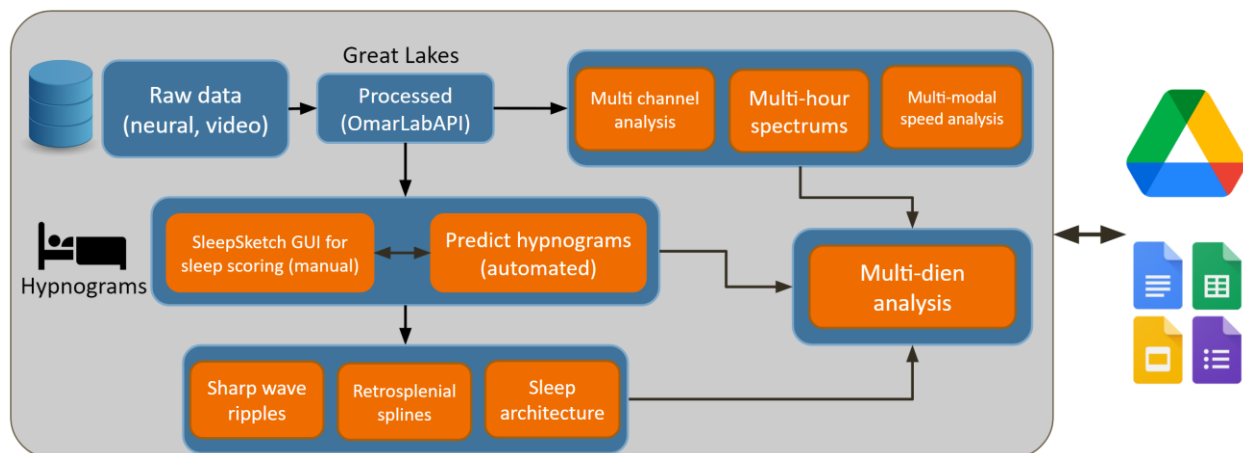
Figure 5.1: 24/7 automated workflow
End to end analysis pipeline. Raw data from multiple recording systems (Neuralynx, Open Ephys, SpikeGLX) are converted to a standardized data format usable with the OmarLabAPI. Afterwards, various sleep, spectral, and movement analyses are calculated. Animals with multiple recorded sessions are collected for multi-dien analyses of sleep and spectral components. Bi-hourly jobs are orchestrated through MATLAB, where the type of analysis pipeline is determined. After analyses have finished, the relevant figures and tables are uploaded to a shared Google Drive.

5.2.2 SleepSketch

Sleep states were manually verified using SleepSketch, a custom graphical user interface

(GUI) in 0.5s windows which allowed precise assignment of sleep transitions (**Figure 5.1**). A

custom GUI allowed the implementation of a novel scoring method as well as custom metrics

(speed, delta power, and theta ratio) and high resolution time windows that were not present in

other open source (wonambi/Sleep, SpiSOP, sleepSMG) and commercial products (SleepScore,

Gamma Sleep Scoring Software) available (Combrisson et al., 2017). As of writing, clinical

sleep scoring software typically limits users to viewing small segments of data (<60s) and

labeling sleep states in large windows of up to 30s which limits precise neural correlates of sleep,

and are limited to scoring with repeated keystrokes. A small frame of reference reduces the

context of previous and future brain states to facilitate correct decisions. Furthermore, repetitive

actions in small windows are not ideal for continuous 24/7 recordings, and may potentially lead

to repetitive strain injury.

SleepSketch allows users to use a cursor to draw a line to label the desired sleep state. This

method allows consecutive sleep states to be labeled instantaneously rather than necessitating

repeated keystrokes to achieve the same labeling. SleepSketch is particularly advantageous

during longer 24/7 recordings where instantaneous labeling of an hour of continuous

wakefulness saves the scorer many minutes. SleepSketch is implemented with semi-supervised

scoring in mind, where vertical lines can be generated for each sleep state to facilitate the

validation of model performance on an unscored session. A skilled user of SleepSketch can

manually score a new 24 hour session in under 30 minutes, and when given model predictions, a

24 hour session can be scored in under 15 minutes.

5.2.2.1 Rules based sleep classification

Sleep states were first estimated using a rules based classifier, where individual sleep states were identified using the metrics in the section above. We performed a normalization procedure by awake states to improve the generalizability of the classifier. For each session, we first normalized the movement signal by subtracting the average and dividing by the standard deviation (z-score) of the entire session. Then, we identified periods of movement using a threshold of 0.25Z as the "baseline" period. Afterwards, we performed z-score normalization of each metric (movement, delta power, theta ratio) to this "baseline." This method provides state independent normalization since some recording sessions may have any NREM and REM epochs. Furthermore, any neural recording is nearly guaranteed to have some awake periods.

Following this state independent normalization, we set a threshold of 0.25Z for wakefulness, and 1Z for NREM and REM. The sleep states were then assigned in the following order to minimize false positives: NREM, REM, then awake. The remaining sleep states were marked as unclassified. We identified awake as the final sleep state since movement is a clear indicator of wakefulness. To minimize behaviorally improbable state transitions, we required sleep states to last a minimum of 30s, and we applied a temporal majority voting (TMV) system where the most common sleep state in each 30s window is applied to the entire window.

To further ensure a generalized sleep scoring system, we applied the classifier on all implanted electrodes, ranging from 32 to 64 electrodes, and performed spatial majority voting (SMV). In the SMV procedure we require at least 1/4 of the electrodes to agree, giving preference to NREM and REM states.

5.2.2.2   Machine learning sleep classification

   The rules based classifier was used to facilitate initial process of manual sleep scoring. However, the rules based classifier often did not meet our accuracy criteria, and many states had to be re-labeled. As a secondary step to our semi-automated sleep scoring, after 24hrs of sleep states were manually labeled, we trained a supervised machine learning algorithm to further manage the large volume of data that needed to be labeled. We implemented XGBoost, a gradient boosted tree based algorithm, as opposed to a logistic regression or neural network for multiple reasons: (1) interpretability, (2) speed, (3) low data requirements, and (3) non-linear fit (Chen & Guestrin, 2016). Furthermore, statistical models and machine learning allow a greater number of features as well as cross-feature interactions in the estimation of sleep states.

   Similar to the rules based classification, we utilized spectral features from neural recordings as well as movement signal from the accelerometer or video. However, there were different steps for pre-processing aimed to provide the machine learning classifier many inputs to better estimate sleep states. For the movement signal, in sessions with accelerometer signal we (1) performed state independent normalization, (2) calculated the root mean square (RMS) in 1s windows with 0.5s steps, and averaged the x, y, and z signals, then finally we (4) set the peak of the aggregate signal to 98% of the maximum during that session to minimize outlier influence on the model fit. For spectral features, we utilized the multi-taper analysis using the chronux toolbox (https://chronux.org/). We (1) applied this transformation using 8s windows with 0.5s steps and limited the frequency range from 0 to 40 Hz in 0.2Hz steps, then (2) performed state independent normalization for each frequency feature for "spectral whitening" since neural signals follow the 1/f power rule. The final set of features used in the machine learning model

114

were the spectral power from 0 to 40Hz in 0.2Hz steps and the movement signal leading to ~200 features.

Due to the variation in signal quality and implantation sites across animals, it was necessary to fit a model to individual animals, rather than a single generalized model. Each animal had a model trained to itself after at least a 24 hour session was manually curated. A train-test split of 80-20 was applied on the ground truth data. Finally, we performed TMV and SMV voting similar to the rules based classification.
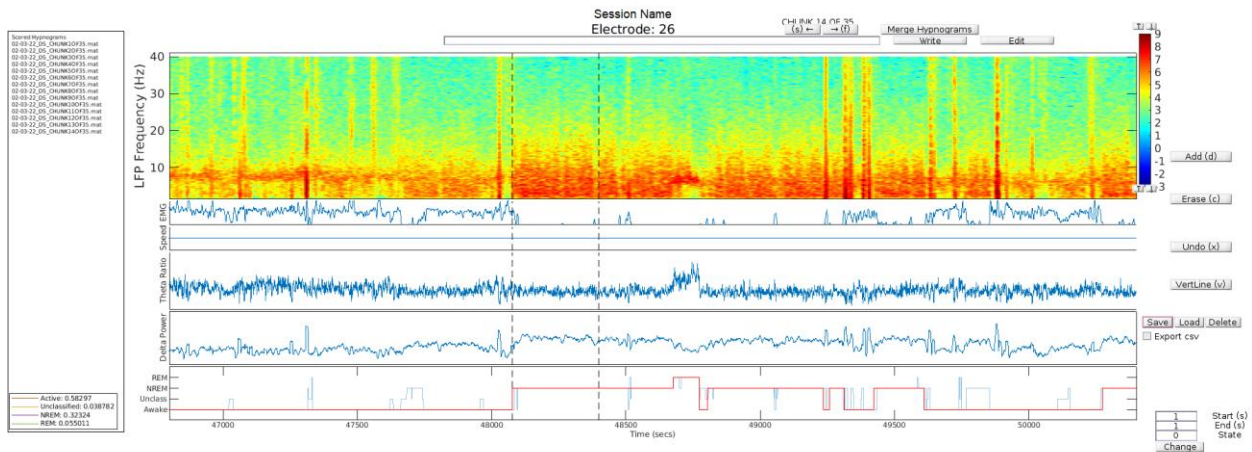
Figure 5.2: SleepSketch GUI for sleep state scoring

Software written in MATLAB to facilitate sleep scoring. Sleep states are scored in hourly segments to ensure consistent views of the data. We utilize the relationship across spectral components from 0-40Hz, speed, theta-delta ratio, and delta power to estimate sleep states. Sleep states can be drawn using the Add button to indicate awake, unclassified, NREM, and REM states. The last 5 actions can be reverted using the Undo button. The VertLine button allows users to align the various features used in scoring, providing high temporal precision. After all of the hypnograms have been scored per hour, the Merge Hypnograms function will concatenate the individual files into a single file for analysis.

5.3   Discussion

   Here, I briefly describe two software solutions developed to facilitate analysis of the 24/7 continuous recordings in Chapter 4. The 24/7 analysis service provides a no-code solution for experimentalists to effectively analyze data using a standardized pipeline (**Figure 5.1**). The service provides various benefits including 1) reducing load on computational members of the lab, 2) ensuring that the same basic transformations are applied across datasets and reducing bugs or variance across researchers, and 3) provides a plethora of visualizations that can be quickly used to assess the quality of recordings. Sleep states are scored with a semi-automated procedure utilizing the 24/7 service, then are ultimately manually verified using SleepSketch (**Figure 5.2**). SleepSketch provides researchers an efficient method to characterize sleep states with a high time resolution of 0.5s windows, where 24 hours of data can be validated in under 15 minutes. Furthermore, the intuitive GUI allows quicker training of researchers for sleep scoring, and the available tools allow project leads to rapidly validate the scoring quality. These systems have been developed with generalizability in mind, and are currently being used in various other experiments in the Omar Lab.

Chapter 6: Discussion and Future Directions

As described in Chapter 1, this dissertation aimed to investigate the contributions of the hippocampus in neural circuits pertaining to spatial navigation, reward encoding, and epilepsy. In Chapter 2, we describe novel head direction (HD) and head velocity cells (AHV) in the nucleus accumbens (NAcc) and ventral pallidum (VP), two key regions in the mesolimbic reward circuit. Importantly, these AHV cells are state-dependent, where periods of high hippocampal theta rhythm activity are accompanied by lower AHV encoding. In Chapter 3, we describe multi-timescale coordination of activity from the NAcc and VP with hippocampal sharp wave ripples (SWRs) during the pavlovian conditioned approach (PCA) task. Surprisingly, animals which oriented towards the goal (goal trackers) rather than the cue (sign trackers) during the PCA task displayed longer hippocampal SWRs indicating differential task encoding as suggested by their task responses. In Chapter 4, using a linear silicon probe spanning the cortex, hippocampus, and thalamus, we describe early hippocampal activity during seizures in a mouse model of epileptic encephalopathy ($Scn8a^{R1872W}$). The hippocampus preceded the cortex and thalamus by approximately 1 second during both fatal and non-fatal seizures. Thus each chapter in this dissertation highlights important roles and correlates of hippocampal brain rhythms.

For example, in Chapter 2 we described how periods of high hippocampal theta rhythms is associated with a state-dependent change from head velocity encoding to reward encoding within reward encoding regions. We suggest that it would be computationally efficient for cells within

the nucleus accumbens (NAcc) and ventral pallidum (VP) to compute both orientation and reward, where accurate navigation would support the motivated acquisition of a reward. While the study comprehensively identified the behavioral conditions that are associated with this change, many questions remain: 1) If the state-dependent switch hypothesis is true, then we could expect head velocity cells to have a higher likelihood of also encoding reward value. 2) Since the reward location is stationary during the task, perhaps these regions do not need to exhaustively encode orientation and instead can afford to switch encoding regimes, therefore allowing more efficient encoding of the reward value. This can potentially be tested with a behavioral task containing randomized reward locations each trial. 3) Is the AHV encoding an efference copy, or do the NAcc and VP have the capacity to influence head orientation? The VP is thought to sit at the limbic-motor interface, where motivational signals are converted to motor output. The VTA is an essential region within the mesolimbic reward circuit, which sends dopaminergic projections to the NAcc and VP. Optogenetic stimulations within the VTA in Hughes et al. 2019 induced immediate head turns, suggesting that the VTA has a direct role in motor output, which we speculate may result from projections to the VP.

Similarly, there are a few unanswered questions in Chapter 3 suitable for future studies. We showed that some NAcc neurons displayed a decrease in activity for many seconds around hippocampal SWRs, followed by a transient increase in activity during SWRs. Surprisingly, NAcc neurons showing this multi-timescale response to SWRs were more responsive to the task-related conditioned stimulus. But could this multi-timescale response manifest differently during sharp wave ripples (SWR) in awake and sleep states? How about active versus immobile awake states? More importantly, what are the underlying mechanisms leading to this multi-timescale coordination?

Lastly, in Chapter 4 we described early hippocampal seizure onset, uniquely long interictal discharge events (IID), as well as sleep architecture and hippocampal ripple predictors of sudden unexpected death in epilepsy (SUDEP), but a few questions remain: 1) How does the sustained arousal in $Scn8a^{R1872W}$ mice affect behavioral performance? 2) Would $Scn8a^{R1872W}$ mice require greater stimulation of sleep-promoting circuits to transition to a sleep state? 3) What are the mechanisms of the long interictal discharges? 4) What are the neuronal types within the hippocampus that facilitate early seizure activity in this region? It would be advantageous, but potentially computationally infeasible to record continuous 24/7 single unit activity of spontaneous seizures in $Scn8a^{R1872W}$ mice. The probes utilized in Chapter 4 contained 32 channels spaced by 100μm, which is too large a distance for optimal single unit isolation. A compromise would be to record from higher density 32-128 channel probes, with all located within the hippocampus, allowing for improved single unit recordings.

References

Agarwal, G., Ian H. Stevenson, Berényi, A., Mizuseki, K., Buzsáki, G., & Sommer, F. T. (2014). Spatially Distributed Local Fields in the Hippocampus Encode Rat Position. *Science*, *344*(May), 626–630.

Ahmed, O. J., & Mehta, M. R. (2012). Running Speed Alters the Frequency of Hippocampal Gamma Oscillations. *Journal of Neuroscience*, *32*(21), 7373–7383. https://doi.org/10.1523/JNEUROSCI.5110-11.2012

Ahrens, A. M., & Ahmed, O. J. (2020). Neural Circuits linking sleep and addiction: Animal models to understand why select individuals are more vulnerable to substance use disorders after sleep deprivation. *Neuroscience and Biobehavioral Reviews*, *108*, 435–444. https://doi.org/10.1016/j.ygyno.2016.04.081

Ahrens, A. M., Ferguson, L. M., Robinson, T. E., & Aldridge, J. W. (2018). Dynamic Encoding of Incentive Salience in the Ventral Pallidum: Dependence on the Form of the Reward Cue. *Eneuro*, *5*(2), ENEURO.0328-17.2018. https://doi.org/10.1523/eneuro.0328-17.2018

Ahrens, A. M., Meyer, P. J., Ferguson, L. M., Robinson, T. E., & Aldridge, J. W. (2016). Neural Activity in the Ventral Pallidum Encodes Variation in the Incentive Value of a Reward Cue. *The Journal of Neuroscience*, *36*(30), 7957–7970. https://doi.org/10.1523/JNEUROSCI.0736-16.2016

Ahrens, A. M., Singer, B. F., Fitzpatrick, C. J., Morrow, J. D., & Robinson, T. E. (2016). Rats that sign-track are resistant to Pavlovian but not instrumental extinction. *Behavioural Brain Research*, *296*, 418–430. https://doi.org/10.1016/j.bbr.2015.07.055

Aitken, P., Zheng, Y., & Smith, P. F. (2018). The modulation of hippocampal theta rhythm by the vestibular system. *Journal of Neurophysiology*, *119*(2), 548–562. https://doi.org/10.1152/jn.00548.2017

Alexander, A. S., Tung, J. C., Chapman, G. W., Conner, A. M., Shelley, L. E., Hasselmo, M. E., & Nitz, D. A. (2022). Adaptive integration of self-motion and goals in posterior parietal cortex. *Cell Reports*, *38*(10), 110504. https://doi.org/10.1016/j.celrep.2022.110504

Alickovic, E., & Subasi, A. (2018). Ensemble SVM method for automatic sleep stage classification. *IEEE Transactions on Instrumentation and Measurement*, *67*(6), 1258–1265. https://doi.org/10.1109/TIM.2018.2799059

Amakhin, D. V., Ergina, J. L., Chizhov, A. V., & Zaitsev, A. V. (2016). Synaptic conductances during interictal discharges in pyramidal neurons of rat entorhinal cortex. *Frontiers in Cellular Neuroscience*, *10*(OCT2016), 1–15. https://doi.org/10.3389/fncel.2016.00233

Annett, L. E., McGregor, A., & Robbins, T. W. (1989). The effects of ibotenic acid lesions of the nucleus accumbens on spatial learning and extinction in the rat. *Behavioural Brain Research*, *31*(3), 231–242. https://doi.org/10.1016/0166-4328(89)90005-3

Arduini, A. A., & Green, J. D. (1954). Hippocampal Electrical Activity in Arousal. *Journal of*

Neurophysiology, *17*(6), 533–557.

Aronov, D., Nevers, R., & Tank, D. W. (2017). Mapping of a non-spatial dimension by the hippocampal-entorhinal circuit. *Nature*, *543*(7647), 719–722. https://doi.org/10.1038/nature21692

Aserinsky, E., & Kleitman, N. (1953). Regularly occurring periods of eye motility, and concomitant phenomena, during sleep. *Science*, *118*(3062), 273.

Avila, I., & Lin, S. C. (2014). Motivational Salience Signal in the Basal Forebrain Is Coupled with Faster and More Precise Decision Speed. *PLoS Biology*, *12*(3). https://doi.org/10.1371/journal.pbio.1001811

Avoli, M., Biagini, G., & Curtis, M. de. (2006). Do Interictal Spikes Sustain Seizures and Epileptogenesis? *Epilepsy Currents*, *6*(6), 203–207.

Bassett, J. P., & Taube, J. S. (2001). Neural correlates for angular head velocity in the rat dorsal tegmental nucleus. *Journal of Neuroscience*, *21*(15), 5740–5751. https://doi.org/10.1523/jneurosci.21-15-05740.2001

Baud, M. O., Ghestem, A., Benoliel, J. J., Becker, C., & Bernard, C. (2019). Endogenous multidien rhythm of epilepsy in rats. *Experimental Neurology*, *315*(January), 82–87. https://doi.org/10.1016/j.expneurol.2019.02.006

Berens, P. (2009). CircStat: A MATLAB Toolbox for Circular Statistics. *Journal of Statistical Software*, *31*(10).

Berridge, K. C., & Kringelbach, M. L. (2015). Pleasure Systems in the Brain. *Neuron*, *86*(3), 646–664. https://doi.org/10.1016/j.neuron.2015.02.018

Blair, H. T., & Sharp, P. E. (1995). Anticipatory head direction signals in anterior thalamus: Evidence for a thalamocortical circuit that integrates angular head motion to compute head direction. *Journal of Neuroscience*, *15*(9), 6260–6270. https://doi.org/10.1523/jneurosci.15-09-06260.1995

Blanchard, M. G., Willemsen, M. H., Walker, J. B., Dib-Hajj, S. D., Waxman, S. G., Jongmans, M. C. J., Kleefstra, T., van de Warrenburg, B. P., Praamstra, P., Nicolai, J., Yntema, H. G., Bindels, R. J. M., Meisler, M. H., & Kamsteeg, E. J. (2015). De novo gain-of-function and loss-of-function mutations of SCN8A in patients with intellectual disabilities and epilepsy. *Journal of Medical Genetics*, *52*(5), 330–337. https://doi.org/10.1136/jmedgenet-2014-102813

Brandon, M. P., Bogaard, A. R., Libby, C. P., Connerney, M. A., Gupta, K., & Hasselmo, M. E. (2011). Reduction of Theta Rhythm Dissociates Grid Cell Spatial Periodicity from Directional Tuning. *Science*, *332*(April), 595–600. https://doi.org/10.7551/mitpress/3629.003.0022

Brandon, M. P., Koenig, J., Leutgeb, J. K., & Leutgeb, S. (2014). New and Distinct Hippocampal Place Codes Are Generated in a New Environment during Septal Inactivation. *Neuron*, *82*(4), 789–796. https://doi.org/10.1016/j.neuron.2014.04.013

Brennan, E. K. W., Jedrasiak-Cape, I., Kailasa, S., Rice, S. P., Sudhakar, S. K., & Ahmed, O. J. (2021). Thalamus and claustrum control parallel layer 1 circuits in retrosplenial cortex. *ELife*, *10*, 1–42. https://doi.org/10.7554/eLife.62207

Bresch, E., Großekathöfer, U., & Garcia-Molina, G. (2018). Recurrent Deep Neural Networks for Real-Time Sleep Stage Classification From Single Channel EEG. *Frontiers in Computational Neuroscience*, *12*(October), 1–12. https://doi.org/10.3389/fncom.2018.00085

Brown, J. E., Card, J. P., & Yates, B. J. (2005). Polysynaptic pathways from the vestibular nuclei to the lateral mammillary nucleus of the rat: Substrates for vestibular input to head direction cells. *Experimental Brain Research*, *161*(1), 47–61. https://doi.org/10.1007/s00221-004-2045-4

Bunton-Stasyshyn, R. K. A., Wagnon, J. L., Wengert, E. R., Barker, B. S., Faulkner, A., Wagley, P. K., Bhatia, K., Jones, J. M., Maniaci, M. R., Parent, J. M., Goodkin, H. P., Patel, M. K., & Meisler, M. H. (2019). Prominent role of forebrain excitatory neurons in SCN8A encephalopathy. *Brain*, *142*(2), 362–375. https://doi.org/10.1093/brain/awy324

Butler, W. N., Smith, K. S., van der Meer, M. A. A., & Taube, J. S. (2017). The Head-Direction Signal Plays a Functional Role as a Neural Compass during Navigation. *Current Biology*, *27*(9), 1259–1267. https://doi.org/10.1016/j.cub.2017.03.033

Buzsaki, G. (2002). Theta Oscillations in the Hippocampus. *Neuron*, *33*(3), 1–20. https://doi.org/DOI: http://dx.doi.org/10.1016/S0896-6273(02)00586-X

Buzsáki, G. (2005). Theta rhythm of navigation: Link between path integration and landmark navigation, episodic and semantic memory. *Hippocampus*, *15*(7), 827–840. https://doi.org/10.1002/hipo.20113

Buzsáki, G. (2015). Hippocampal sharp wave-ripple: A cognitive biomarker for episodic memory and planning. *Hippocampus*, *25*(10), 1073–1188. https://doi.org/10.1002/hipo.22488

Chang, S. E., & Holland, P. C. (2013). Effects of nucleus accumbens core and shell lesions on autoshaped lever-pressing. *Behavioural Brain Research*, *256*, 36–42. https://doi.org/10.1016/j.bbr.2013.07.046

Cheah, C. S., Lundstrom, B. N., Catteral, W. A., & Oakley, J. C. (2019). Impairment of sharp-wave ripples in a murine model of dravet syndrome. *Journal of Neuroscience*, *39*(46), 9251–9260. https://doi.org/10.1523/JNEUROSCI.0890-19.2019

Chen, T., & Guestrin, C. (2016). XGBoost: A Scalable Tree Boosting System. *Proceedings of the 22nd ACM SIGKDD International Conference on Knowledge Discovery and Data Mining*, 785–794. https://doi.org/https://doi.org/10.1145/2939672.2939785

Cho, J., & Sharp, P. E. (2001). Head direction, place, and movement correlates for cells in the rat retrosplenial cortex. *Behavioral Neuroscience*, *115*(1), 3–25. https://doi.org/10.1037/0735-7044.115.1.3

Chvojka, J., Kudlacek, J., Chang, W. C., Novak, O., Tomaska, F., Otahal, J., Jefferys, J. G. R., & Jiruska, P. (2021). The role of interictal discharges in ictogenesis — A dynamical perspective. *Epilepsy and Behavior*, *121*, 106591. https://doi.org/10.1016/j.yebeh.2019.106591

Cimbalnik, J., Brinkmann, B., Kremen, V., Jurak, P., Berry, B., Gompel, J. Van, Stead, M., & Worrell, G. (2018). Physiological and pathological high frequency oscillations in focal epilepsy. *Annals of Clinical and Translational Neurology*, *5*(9), 1062–1076. https://doi.org/10.1002/acn3.618

Clark, B. J., & Taube, J. S. (2012). Vestibular and attractor network basis of the head direction cell signal in subcortical circuits. *Frontiers in Neural Circuits*, *6*(FEBRUARY), 1–12. https://doi.org/10.3389/fncir.2012.00007

Colgin, L. L. (2013). Mechanisms and Functions of Theta Rhythms. *Annual Review of Neuroscience*, *36*(1), 295–312. https://doi.org/10.1146/annurev-neuro-062012-170330

Colgin, L. L. (2016). Rhythms of the hippocampal network. *Nature Reviews Neuroscience*,

17(4), 239–249. https://doi.org/10.1038/nrn.2016.21

Combrisson, E., Vallat, R., Eichenlaub, J. B., O'Reilly, C., Lajnef, T., Guillot, A., Ruby, P. M., & Jerbi, K. (2017). Sleep: An open-source python software for visualization, analysis, and staging of sleep data. *Frontiers in Neuroinformatics*, *11*(September), 1–11. https://doi.org/10.3389/fninf.2017.00060

Cooper, D. C., Klipec, W. D., Fowler, M. A., & Ozkan, E. D. (2006). A role for the subiculum in the brain motivation/reward circuitry. *Behavioural Brain Research*, *174*(2), 225–231. https://doi.org/10.1016/j.bbr.2006.05.036

Curtis, M. De, & Avanzini, G. (2001). Interictal spikes in focal epileptogenesis. *Progress in Neurobiology*, *63*, 541–567.

De Gennaro, L., & Ferrara, M. (2003). Sleep spindles: An overview. *Sleep Medicine Reviews*, *7*(5), 423–440. https://doi.org/10.1053/smrv.2002.0252

Devinsky, O., Vezzani, A., O'Brien, T. J., Jette, N., Scheffer, I. E., De Curtis, M., & Perucca, P. (2018). Epilepsy. *Nature Reviews Disease Primers*, *4*(May). https://doi.org/10.1038/nrdp.2018.24

Dudchenko, P. A., Wood, E. R., & Smith, A. (2019). A new perspective on the head direction cell system and spatial behavior. *Neuroscience and Biobehavioral Reviews*, *105*(June), 24–33. https://doi.org/10.1016/j.neubiorev.2019.06.036

Eban-Rothschild, A., Appelbaum, L., & de Lecea, L. (2017). Neuronal Mechanisms for Sleep/Wake Regulation and Modulatory Drive. *Neuropsychopharmacology*, *43*(5), 937–952. https://doi.org/10.1038/npp.2017.294

Ego-Stengel, V., & Wilson, M. A. (2010). Disruption of ripple-associated hippocampal activity during rest impairs spatial learning in the rat. *Hippocampus*, *20*(1), 1–10. https://doi.org/10.1002/hipo.20707

Eschenko, O., Ramadan, W., Mölle, M., Born, J., & Sara, S. J. (2008). Sustained increase in hippocampal sharp-wave ripple activity during slow-wave sleep after learning. *Learning and Memory*, *15*(4), 222–228. https://doi.org/10.1101/lm.726008

Etienne, A. S., & Jeffery, K. J. (2004). Path integration in mammals. *Hippocampus*, *14*(2), 180–192. https://doi.org/10.1002/hipo.10173

Ferguson, L. M., Ahrens, A. M., Longyear, L. G., & Wayne Aldridge, J. (2020). Neurons of the ventral tegmental area encode individual differences in motivational ⬳wanting⬲ for reward cues. *Journal of Neuroscience*, *40*(46), 8951–8963. https://doi.org/10.1523/JNEUROSCI.2947-19.2020

Fernández-Ruiz, A., Oliva, A., de Oliveira, E. F., Rocha-Almeida, F., Tingley, D., & Buzsáki, G. (2019). Long-duration hippocampal sharp wave ripples improve memory. *Science*, *364*(6445), 1082–1086. https://doi.org/10.1126/science.aax0758

Flagel, S. B., Akil, H., & Robinson, T. E. (2009). Individual differences in the attribution of incentive salience to reward-related cues: Implications for addiction. *Neuropharmacology*, *56*(SUPPL. 1), 139–148. https://doi.org/10.1016/j.neuropharm.2008.06.027

Flagel, S. B., & Robinson, T. E. (2017). Neurobiological basis of individual variation in stimulus-reward learning. *Current Opinion in Behavioral Sciences*, *13*, 178–185. https://doi.org/10.1016/j.cobeha.2016.12.004

Flagel, S. B., Robinson, T. E., Clark, J. J., Clinton, S. M., Watson, S. J., Seeman, P., Phillips, P. E. M., & Akil, H. (2010). An animal model of genetic vulnerability to behavioral disinhibition and responsiveness to reward-related cues: Implications for addiction.

Neuropsychopharmacology, *35*(2), 388–400. https://doi.org/10.1038/npp.2009.142

Floresco, S. B., Todd, C. L., & Grace, A. A. (2001). Glutamatergic afferents from the hippocampus to the nucleus accumbens regulate activity of ventral tegmental area dopamine neurons. *The Journal of Neuroscience : The Official Journal of the Society for Neuroscience*, *21*(13), 4915–4922. http://www.ncbi.nlm.nih.gov/pubmed/11425919

Foo, S., & Bohbot, V. D. (2020). Theta rhythm across the species: Bridging inconsistencies with a multiple memory systems approach. *Behavioral Neuroscience*, *134*(6), 475–490. https://doi.org/10.1037/bne0000440

Furtak, S. C., Ahmed, O. J., & Burwell, R. D. (2012). Single Neuron Activity and Theta Modulation in Postrhinal Cortex during Visual Object Discrimination. *Neuron*, *76*(5), 976–988. https://doi.org/10.1016/j.neuron.2012.10.039

Gardella, E., Marini, C., Trivisano, M., Fitzgerald, M. P., Alber, M., Howell, K. B., Darra, F., Siliquini, S., Bölsterli, B. K., Masnada, S., Pichiecchio, A., Johannesen, K. M., Jepsen, B., Fontana, E., Anibaldi, G., Russo, S., Cogliati, F., Montomoli, M., Specchio, N., … Møller, R. S. (2018). The phenotype of SCN8A developmental and epileptic encephalopathy. *Neurology*, *91*(12), E1112–E1124. https://doi.org/10.1212/WNL.0000000000006199

Garg, D., Charlesworth, L., & Shukla, G. (2022). Sleep and Temporal Lobe Epilepsy – Associations, Mechanisms and Treatment Implications. *Frontiers in Human Neuroscience*, *16*(April), 1–16. https://doi.org/10.3389/fnhum.2022.849899

Gelinas, J. N., Khodagholy, D., Thesen, T., Devinsky, O., & Buzsáki, G. (2016). Interictal epileptiform discharges induce hippocampal-cortical coupling in temporal lobe epilepsy. *Nature Medicine*, *22*(6), 641–648. https://doi.org/10.1038/nm.4084

Ghosh, M., Shanahan, B. E., Furtak, S. C., Mashour, G. A., Burwell, R. D., & Ahmed, O. J. (2020). Instantaneous amplitude and shape of postrhinal theta oscillations differentially encode running speed. *BioRxiv*, 2020.06.03.130609. https://doi.org/10.1101/2020.06.03.130609

Ghosh, M., Yang, F., Rice, S. P., John, T. T., Ahrens, A. M., Ahmed, O. J., Ghosh, M., Yang, F., Rice, S. P., Hetrick, V., Gonzalez, A. L., & Siu, D. (2022). Running speed and REM sleep control two distinct modes of rapid interhemispheric communication ll ll Running speed and REM sleep control two distinct modes of rapid interhemispheric communication. *Cell ReportsReports*, *40*(1), 111028. https://doi.org/10.1016/j.celrep.2022.111028

Gillis, Z. S., & Morrison, S. E. (2019). Sign Tracking and Goal Tracking Are Characterized by Distinct Patterns of Nucleus Accumbens Activity. *Eneuro*, *6*(2), ENEURO.0414-18.2019. https://doi.org/10.1523/ENEURO.0414-18.2019

Girardeau, G., Benchenane, K., Wiener, S. I., Buzsáki, G., & Zugaro, M. B. (2009). Selective suppression of hippocampal ripples impairs spatial memory. *Nature Neuroscience*, *12*(10), 1222–1223. https://doi.org/10.1038/nn.2384

Girardeau, G., Inema, I., & Buzsáki, G. (2017). Reactivations of emotional memory in the hippocampus-amygdala system during sleep. *Nature Neuroscience*, *20*(11), 1634–1642. https://doi.org/10.1038/nn.4637

Gomperts, S. N., Kloosterman, F., & Wilson, M. A. (2015). VTA neurons coordinate with the hippocampal reactivation of spatial experience. *ELife*, *4*, 1–22. https://doi.org/10.7554/elife.05360

Goncharova, I. I., Alkawadri, R., Gaspard, N., Duckrow, R. B., Spencer, D. D., Hirsch, L. J., Spencer, S. S., & Zaveri, H. P. (2016). The relationship between seizures, interictal spikes

and antiepileptic drugs. *Clinical Neurophysiology*, *127*(9), 3180–3186. https://doi.org/10.1016/j.clinph.2016.05.014

Goutagny, R., Jackson, J., & Williams, S. (2009). Self-generated theta oscillations in the hippocampus. *Nature Neuroscience*, *12*(12), 1491–1493. https://doi.org/10.1038/nn.2440

Groenewegen, H. J., der Zee, E. V. Van, te Kortschot, A., & Witter, M. P. (1987). Organization of the projections from the subiculum to the ventral striatum in the rat. A study using anterograde transport of Phaseolus vulgaris leucoagglutinin. *Neuroscience*, *23*(1), 103–120. https://doi.org/10.1016/0306-4522(87)90275-2

Hafting, T., Fyhn, M., Molden, S., Moser, M. B., & Moser, E. I. (2005). Microstructure of a spatial map in the entorhinal cortex. *Nature*, *436*(7052), 801–806. https://doi.org/10.1038/nature03721

Huberfeld, G., Blauwblomme, T., & Miles, R. (2015). Hippocampus and epilepsy: Findings from human tissues. *Revue Neurologique*, *171*(3), 236–251. https://doi.org/10.1016/j.neurol.2015.01.563

Huberfeld, Gilles, Menendez De La Prida, L., Pallud, J., Cohen, I., Le Van Quyen, M., Adam, C., Clemenceau, S., Baulac, M., & Miles, R. (2011). Glutamatergic pre-ictal discharges emerge at the transition to seizure in human epilepsy. *Nature Neuroscience*, *14*(5), 627–635. https://doi.org/10.1038/nn.2790

Hughes, R. N., Bakhurin, K. I., Petter, E. A., Watson, G. D. R., Kim, N., Friedman, A. D., & Yin, H. H. (2020). Ventral Tegmental Dopamine Neurons Control the Impulse Vector during Motivated Behavior. *Current Biology*, *30*(14), 2681-2694.e5. https://doi.org/10.1016/j.cub.2020.05.003

Hughes, R. N., Watson, G. D. R., Petter, E. A., Kim, N., Bakhurin, K. I., & Yin, H. H. (2019). Precise Coordination of Three-Dimensional Rotational Kinematics by Ventral Tegmental Area GABAergic Neurons. *Current Biology*, *29*(19), 3244-3255.e4. https://doi.org/10.1016/j.cub.2019.08.022

Ikemoto, S., & Panksepp, J. (1999). The role of nucleus accumbens dopamine in motivated behavior: A unifying interpretation with special reference to reward-seeking. *Brain Research Reviews*, *31*(1), 6–41. https://doi.org/10.1016/S0165-0173(99)00023-5

Ito, R., Robbins, T. W., Pennartz, C. M., & Everitt, B. J. (2008). Functional Interaction between the Hippocampus and Nucleus Accumbens Shell Is Necessary for the Acquisition of Appetitive Spatial Context Conditioning. *Journal of Neuroscience*, *28*(27), 6950–6959. https://doi.org/10.1523/jneurosci.1615-08.2008

Jacob, P. Y., Casali, G., Spieser, L., Page, H., Overington, D., & Jeffery, K. (2017). An independent, landmark-dominated head-direction signal in dysgranular retrosplenial cortex. *Nature Neuroscience*, *20*(2), 173–175. https://doi.org/10.1038/nn.4465

Jadhav, S. P., Kemere, C., German, P. W., & Frank, L. M. (2012). Awake Hippocampal Sharp-Wave Support Spatial Memory. *Science Magazine*, *336*(June), 1454–1458. https://doi.org/10.1126/science.1217230

Jadhav, S. P. P., Rothschild, G., Roumis, D. K. K., & Frank, L. M. M. (2016). Coordinated Excitation and Inhibition of Prefrontal Ensembles during Awake Hippocampal Sharp-Wave Ripple Events. *Neuron*, *90*(1), 113–127. https://doi.org/10.1016/j.neuron.2016.02.010

Jin, B., Aung, T., Geng, Y., & Wang, S. (2020). Epilepsy and Its Interaction With Sleep and Circadian Rhythm. *Frontiers in Neurology*, *11*(May), 1–7. https://doi.org/10.3389/fneur.2020.00327

Jirsch, J. D., Urrestarazu, E., LeVan, P., Olivier, A., Dubeau, F., & Gotman, J. (2006). High-frequency oscillations during human focal seizures. *Brain*, *129*(6), 1593–1608. https://doi.org/10.1093/brain/awl085

Johannesen, K. M., Gardella, E., Scheffer, I., Howell, K., Smith, D. M., Helbig, I., Møller, R. S., & Rubboli, G. (2018). Early mortality in SCN8A-related epilepsies. *Epilepsy Research*, *143*(March), 79–81. https://doi.org/10.1016/j.eplepsyres.2018.04.008

Johannesen, K. M., Liu, Y., Koko, M., Gjerulfsen, C. E., Schubert, J., Fenger, C. D., Eltokhi, A., Rannap, M., Nils, A., Lauxmann, S., Krüger, J., Kegele, J., Canafoglia, L., Mayer, T., Rebstock, J., Zacher, P., Ruf, S., Alber, M., Sterbova, K., … Lund, C. (2021). Genotype-phenotype correlations in SCN8A -related disorders reveal prognostic and therapeutic implications. *Brain*, *2021*, 1–19.

Jongen-Rêlo, A. L., Kaufmann, S., & Feldon, J. (2003). A differential involvement of the shell and core subterritories of the nucleus accumbens of rats in memory processes. *Behavioral Neuroscience*, *117*(1), 150–168. https://doi.org/10.1037/0735-7044.117.1.150

Joo, H. R., & Frank, L. M. (2018). The hippocampal sharp wave–ripple in memory retrieval for immediate use and consolidation. *Nature Reviews Neuroscience*, *19*(12), 744–757. https://doi.org/10.1038/s41583-018-0077-1

Karlsson, M. P., & Frank, L. M. (2009). Awake replay of remote experiences in the hippocampus. *Nature Neuroscience*, *12*(7), 913–918. https://doi.org/10.1038/nn.2344

Karoly, P. J., Freestone, D. R., Boston, R., Grayden, D. B., Himes, D., Leyde, K., Seneviratne, U., Berkovic, S., O'Brien, T., & Cook, M. J. (2016). Interictal spikes and epileptic seizures: Their relationship and underlying rhythmicity. *Brain*, *139*(4), 1066–1078. https://doi.org/10.1093/brain/aww019

Keshavarzi, S., Bracey, E. F., Faville, R. A., Campagner, D., Tyson, A. L., Lenzi, S. C., Branco, T., & Margrie, T. W. (2022). Multisensory coding of angular head velocity in the retrosplenial cortex. *Neuron*, *110*(3), 532-543.e9. https://doi.org/10.1016/j.neuron.2021.10.031

Khan, O. I., Zhao, Q., Miller, F., & Holmes, G. L. (2010). Interictal spikes in developing rats cause long-standing cognitive deficits. *Neurobiology of Disease*, *39*(3), 362–371. https://doi.org/10.1016/j.nbd.2010.05.002

Klitenick, M. A., Deutch, A. Y., Churchill, L., & Kalivas, P. W. (1992). Topography and functional role of dopaminergic projections from the ventral mesencephalic tegmentum to the ventral pallidum. *Neuroscience*, *50*(2), 371–386. https://doi.org/10.1016/0306-4522(92)90430-A

Kocsis, B., Bragin, A., & Buzsáki, G. (1999). Interdependence of multiple theta generators in the hippocampus: A partial coherence analysis. *Journal of Neuroscience*, *19*(14), 6200–6212. https://doi.org/10.1523/jneurosci.19-14-06200.1999

Koenig, J., Linder, A. N., Leutgeb, J. K., & Leutgeb, S. (2011). The Spatial Periodicity of Grid Cells Is Not Sustained During Reduced Theta Oscillations. *Science*, *332*(Issue: 6029), 592–595.

Kong, W., Zhang, Y., Gao, Y., Liu, X., Gao, K., Xie, H., Wang, J., Wu, Y., Zhang, Y., Wu, X., & Jiang, Y. (2015). SCN8A mutations in Chinese children with early onset epilepsy and intellectual disability. *Epilepsia*, *56*(3), 431–438. https://doi.org/10.1111/epi.12925

Kupchik, Y. M., Brown, R. M., Heinsbroek, J. A., Lobo, M. K., Schwartz, D. J., & Kalivas, P. W. (2015). Coding the direct/indirect pathways by D1 and D2 receptors is not valid for

accumbens projections. *Nature Neuroscience*, *18*(9), 1230–1232.
https://doi.org/10.1038/nn.4068

Kupchik, Y. M., & Kalivas, P. W. (2013). The rostral subcommissural ventral pallidum is a mix
of ventral pallidal neurons and neurons from adjacent areas: An electrophysiological study.
Brain Structure and Function, *218*(6), 1487–1500. https://doi.org/10.1007/s00429-012-
0471-9

Lamprea, M. R., Garcia, A. M. B., & Morato, S. (2010). Effects of reversible inactivation of the
medial septum on rat exploratory behavior in the elevated plus-maze using a test-retest
paradigm. *Behavioural Brain Research*, *210*(1), 67–73.
https://doi.org/10.1016/j.bbr.2010.02.011

Lansink, C. S., Goltstein, P. M., Lankelma, J. V., Joosten, R. N. J. M. A., McNaughton, B. L., &
Pennartz, C. M. A. (2008). Preferential Reactivation of Motivationally Relevant
Information in the Ventral Striatum. *Journal of Neuroscience*, *28*(25), 6372–6382.
https://doi.org/10.1523/JNEUROSCI.1054-08.2008

Lansink, C. S., Goltstein, P. M., Lankelma, J. V., McNaughton, B. L., & Pennartz, C. M. A.
(2009). Hippocampus leads ventral striatum in replay of place-reward information. *PLoS
Biology*, *7*(8). https://doi.org/10.1371/journal.pbio.1000173

Lavoie, A. M., & Mizumori, S. J. Y. (1994). Spatial, movement- and reward-sensitive discharge
by medial ventral striatum neurons of rats. *Brain Research*, *638*(1–2), 157–168.
https://doi.org/10.1016/0006-8993(94)90645-9

Lederman, J., Lardeux, S., & Nicola, S. M. (2021). Vigor encoding in the ventral pallidum.
ENeuro, *8*(4), 1–17. https://doi.org/10.1523/ENEURO.0064-21.2021

Lee, M. G., Hassani, O. K., Alonso, A., & Jones, B. E. (2005). Cholinergic basal forebrain
neurons burst with theta during waking and paradoxical sleep. *Journal of Neuroscience*,
25(17), 4365–4369. https://doi.org/10.1523/JNEUROSCI.0178-05.2005

LeGates, T. A., Kvarta, M. D., Tooley, J. R., Francis, T. C., Lobo, M. K., Creed, M. C., &
Thompson, S. M. (2018). Reward behaviour is regulated by the strength of hippocampus–
nucleus accumbens synapses. *Nature*. https://doi.org/10.1038/s41586-018-0740-8

Leguia, M. G., Andrzejak, R. G., Rummel, C., Fan, J. M., Mirro, E. A., Tcheng, T. K., Rao, V.
R., & Baud, M. O. (2021). Seizure Cycles in Focal Epilepsy. *JAMA Neurology*, *78*(4), 454–
463. https://doi.org/10.1001/jamaneurol.2020.5370

Leutgeb, S., & Mizumori, S. J. Y. (1999). Excitotoxic septal lesions result in spatial memory
deficits and altered flexibility of hippocampal single-unit representations. *Journal of
Neuroscience*, *19*(15), 6661–6672. https://doi.org/10.1523/jneurosci.19-15-06661.1999

Lin, S. C., & Nicolelis, M. A. L. (2008). Neuronal Ensemble Bursting in the Basal Forebrain
Encodes Salience Irrespective of Valence. *Neuron*, *59*(1), 138–149.
https://doi.org/10.1016/j.neuron.2008.04.031

Lisman, J. E., & Grace, A. A. (2005). The hippocampal-VTA loop: Controlling the entry of
information into long-term memory. *Neuron*, *46*(5), 703–713.
https://doi.org/10.1016/j.neuron.2005.05.002

Logothetis, N. K., Eschenko, O., Murayama, Y., Augath, M., Steudel, T., Evrard, H. C.,
Besserve, M., & Oeltermann, A. (2012). Hippocampal-cortical interaction during periods of
subcortical silence. *Nature*, *491*(7425), 547–553. https://doi.org/10.1038/nature11618

Long, X., Deng, B., Young, C. K., Liu, G. L., Zhong, Z., Chen, Q., Yang, H., Lv, S. Q., Chen, Z.
S., & Zhang, S. J. (2022). Sharp Tuning of Head Direction and Angular Head Velocity

Cells in the Somatosensory Cortex. *Advanced Science*, *2200020*, 1–15. https://doi.org/10.1002/advs.202200020

Lopez-Santiago, L. F., Yuan, Y., Wagnon, J. L., Hull, J. M., Frasier, C. R., O'Malley, H. A., Meisler, M. H., & Isom, L. L. (2017). Neuronal hyperexcitability in a mouse model of SCN8A epileptic encephalopathy. *Proceedings of the National Academy of Sciences of the United States of America*, *114*(9), 2383–2388. https://doi.org/10.1073/pnas.1616821114

Lubenov, E. V., & Siapas, A. G. (2009). Hippocampal theta oscillations are travelling waves. *Nature*, *459*(7246), 534–539. https://doi.org/10.1038/nature08010

Makinson, C. D., Tanaka, B. S., Lamar, T., Goldin, A. L., & Escayg, A. (2014). Role of the hippocampus in Nav1.6 (Scn8a) mediated seizure resistance. *Neurobiology of Disease*, *68*, 16–25. https://doi.org/10.1016/j.nbd.2014.03.014

Malow, B. A. (2004). Sleep Deprivation and Epilepsy. *Epilepsy Currents*, *4*(5), 193–195. https://doi.org/10.1111/j.1535-7597.2004.04509.x

Manni, R., & Terzaghi, M. (2010). Comorbidity between epilepsy and sleep disorders. *Epilepsy Research*, *90*(3), 171–177. https://doi.org/10.1016/j.eplepsyres.2010.05.006

Martin, M. S., Dutt, K., Papale, L. A., Dubé, C. M., Dutton, S. B., De Haan, G., Shankar, A., Tufik, S., Meisler, M. H., Baram, T. Z., Goldin, A. L., & Escayg, A. (2010). Altered function of the SCN1A voltage-gated sodium channel leads to γ-aminobutyric acid-ergic (GABAergic) interneuron abnormalities. *Journal of Biological Chemistry*, *285*(13), 9823–9834. https://doi.org/10.1074/jbc.M109.078568

Martin, P. D., & Ono, T. (2000). Effects of reward anticipation, reward presentation, and spatial parameters on the firing of single neurons recorded in the subiculum and nucleus accumbens of freely moving rats. *Behavioural Brain Research*, *116*(1), 23–38. https://doi.org/10.1016/S0166-4328(00)00249-7

Maslowski-Cobuzzi, R. J., & Napier, T. C. (1994). Activation of dopaminergic neurons modulates ventral pallidal responses evoked by Amygdala stimulation. *Neuroscience*, *62*(4), 1103–1119. https://doi.org/10.1016/0306-4522(94)90347-6

Mathis, A., Mamidanna, P., Cury, K. M., Abe, T., Murthy, V. N., Mathis, M. W., & Bethge, M. (2018). DeepLabCut: markerless pose estimation of user-defined body parts with deep learning. *Nature Neuroscience*, *21*(9), 1281–1289. https://doi.org/10.1038/s41593-018-0209-y

McFarland, W. L., Teitelbaum, H., & Hedges, E. K. (1975). Relationship between hippocampal theta activity and running speed in the rat. *Journal of Comparative and Physiological Psychology*, *88*(1), 324–328. https://doi.org/10.1037/h0076177

McGinty, V. B., Lardeux, S., Taha, S. A., Kim, J. J., & Nicola, S. M. (2013). Invigoration of reward seeking by cue and proximity encoding in the nucleus accumbens. *Neuron*, *78*(5), 910–922. https://doi.org/10.1016/j.neuron.2013.04.010

McNaughton, B. L., Chen, L. L., & Markus, E. J. (1991). "'Dead reckoning,'" landmark learning, and the sense of direction: A neurophysiological and computational hypothesis. *Journal of Cognitive Neuroscience*, *3*(2), 190–202. https://doi.org/10.1162/jocn.1991.3.2.190

Mehlman, M. L., Winter, S. S., & Taube, J. S. (2019). Functional and anatomical relationships between the medial precentral cortex, dorsal striatum, and head direction cell circuitry. II. Neuroanatomical studies. *Journal of Neurophysiology*, *121*(2), 371–395. https://doi.org/10.1152/jn.00144.2018

Mehlman, M. L., Winter, S. S., Valerio, S., & Taube, J. S. (2019). Functional and anatomical relationships between the medial precentral cortex, dorsal striatum, and head direction cell circuitry. I. recording studies. *Journal of Neurophysiology*, *121*(2), 350–370. https://doi.org/10.1152/jn.00143.2018

Meisler, M. H. (2019). SCN8A encephalopathy: Mechanisms and models. *Epilepsia*, *60*(S3), S86–S91. https://doi.org/10.1111/epi.14703

Meisler, M. H., Helman, G., Hammer, M. F., Fureman, B. E., Gaillard, W. D., Goldin, A. L., Hirose, S., Ishii, A., Kroner, B. L., Lossin, C., Mefford, H. C., Parent, J. M., Patel, M., Schreiber, J., Stewart, R., Whittemore, V., Wilcox, K., Wagnon, J. L., Pearl, P. L., … Scheffer, I. E. (2016). SCN8A encephalopathy: Research progress and prospects. *Epilepsia*, *57*(7), 1027–1035. https://doi.org/10.1111/epi.13422

Meisler, M. H., Hill, S. F., & Yu, W. (2021). Sodium channelopathies in neurodevelopmental disorders. *Nature Reviews Neuroscience*, *22*(3), 152–166. https://doi.org/10.1038/s41583-020-00418-4

Meyer, P. J., Lovic, V., Saunders, B. T., Yager, L. M., Flagel, S. B., Morrow, J. D., & Robinson, T. E. (2012). Quantifying individual variation in the propensity to attribute incentive salience to reward cues. *PLoS ONE*, *7*(6). https://doi.org/10.1371/journal.pone.0038987

Mogenson, G. J., Jones, D. L., & Yim, C. Y. (1980). From motivation to action: Functional interface between the limbic system and the motor system. *Progress in Neurobiology*, *14*(2–3), 69–97. https://doi.org/10.1016/0301-0082(80)90018-0

Mogenson, G. J., & Nielsen, M. (1984). A study of the contribution of hippocampal-accumbens-subpallidal projections to locomotor activity. *Behavioral and Neural Biology*, *42*(1), 38–51. https://doi.org/10.1016/S0163-1047(84)90412-6

Montgomery, S. M., Sirota, A., & Buzsaki, G. (2008). Theta and Gamma Coordination of Hippocampal Networks during Waking and Rapid Eye Movement Sleep. *Journal of Neuroscience*, *28*(26), 6731–6741. https://doi.org/10.1523/JNEUROSCI.1227-08.2008

Morales, M., & Margolis, E. B. (2017). Ventral tegmental area: Cellular heterogeneity, connectivity and behaviour. *Nature Reviews Neuroscience*, *18*(2), 73–85. https://doi.org/10.1038/nrn.2016.165

Morel, P. (2018). Gramm: grammar of graphics plotting in Matlab. *The Journal of Open Source Software*, *3*(23), 568. https://doi.org/10.21105/joss.00568

Moser, E. I., Moser, M. B., & McNaughton, B. L. (2017). Spatial representation in the hippocampal formation: A history. *Nature Neuroscience*, *20*(11), 1448–1464. https://doi.org/10.1038/nn.4653

Mulley, J. C., Scheffer, I. E., Petrou, S., Dibbens, L. M., Berkovic, S. F., & Harkin, L. A. (2005). SCN1A mutations and epilepsy. *Human Mutation*, *25*(6), 535–542. https://doi.org/10.1002/humu.20178

O'Keefe, J., Dostrovsky, J., & J. O'Keefe, J. D. (1971). The hippocampus as a spatial map. Preliminary evidence from unit activity in the freely-moving rat. *Brain Research*, *34*(1), 171–175. http://www.ncbi.nlm.nih.gov/pubmed/5124915

Oades, R. D., & Halliday, G. M. (1987). Ventral tegmental (A10) system: neurobiology. 1. Anatomy and connectivity. *Brain Research Reviews*, *12*(2), 117–165. https://doi.org/10.1016/0165-0173(87)90011-7

Olson, J. M., Tongprasearth, K., & Nitz, D. A. (2017). Subiculum neurons map the current axis of travel. *Nature Neuroscience*, *20*(2), 170–172. https://doi.org/10.1038/nn.4464

Orzeł-Gryglewska, J., Kuśmierczak, M., Majkutewicz, I., & Jurkowlaniec, E. (2012). Induction of hippocampal theta rhythm by electrical stimulation of the ventral tegmental area and its loss after septum inactivation. *Brain Research*, *1436*, 51–67. https://doi.org/10.1016/j.brainres.2011.12.003

Ottenheimer, D., Richard, J. M., & Janak, P. H. (2018). Ventral pallidum encodes relative reward value earlier and more robustly than nucleus accumbens. *Nature Communications*, *9*(1). https://doi.org/10.1038/s41467-018-06849-z

Papale, L. A., Makinson, C. D., Christopher Ehlen, J., Tufik, S., Decker, M. J., Paul, K. N., & Escayg, A. (2013). Altered sleep regulation in a mouse model of SCN1A -derived genetic epilepsy with febrile seizures plus (GEFS+). *Epilepsia*, *54*(4), 625–634. https://doi.org/10.1111/epi.12060

Papale, L. A., Paul, K. N., Sawyer, N. T., Manns, J. R., Tufik, S., & Escayg, A. (2010). Dysfunction of the Scn8a voltage-gated sodium channel alters sleep architecture, reduces diurnal corticosterone levels, and enhances spatial memory. *Journal of Biological Chemistry*, *285*(22), 16553–16561. https://doi.org/10.1074/jbc.M109.090084

Parkinson, J. A., Olmstead, M. C., Burns, L. H., Robbins, T. W., & Everitt, B. J. (1999). *Dissociation in Effects of Lesions of the Nucleus Accumbens Core and Shell on Appetitive Pavlovian Approach Behavior and the Potentiation of Conditioned Reinforcement and Locomotor Activity by D-Amphetamine*. *19*(6), 1–11. papers2://publication/uuid/DF5964C3-0C72-4F58-8457-BB4CD2D84C5E

Pastor, I. A., Hurtado, M. Y., Gibson, C. R., Fitzgerald, C., & Calton, J. L. (2020). Disruption of the anterior thalamic head direction signal following reduction of the hippocampal theta rhythm. *Behavioral Neuroscience*, *134*(6), 577–594. https://doi.org/10.1037/bne0000415

Pennartz, C. M. A. (2004). The Ventral Striatum in Off-Line Processing: Ensemble Reactivation during Sleep and Modulation by Hippocampal Ripples. *Journal of Neuroscience*, *24*(29), 6446–6456. https://doi.org/10.1523/JNEUROSCI.0575-04.2004

Peter-Derex, L., Klimes, P., Latreille, V., Bouhadoun, S., Dubeau, F., & Frauscher, B. (2020). Sleep Disruption in Epilepsy: Ictal and Interictal Epileptic Activity Matter. *Annals of Neurology*, *88*(5), 907–920. https://doi.org/10.1002/ana.25884

Pfeiffer, B. E. (2020). The content of hippocampal "replay." *Hippocampus*, *30*(1), 6–18. https://doi.org/10.1002/hipo.22824

Podkorytova, I., Hays, R., Perven, G., & Alick Lindstrom, S. (2022). Epilepsy surgery in patient with monogenic epilepsy related to SCN8A mutation. *Epilepsy and Behavior Reports*, *18*, 100536. https://doi.org/10.1016/j.ebr.2022.100536

Quigg, M., Gharai, S., Ruland, J., Schroeder, C., Hodges, M., Ingersoll, K. S., Thorndike, F. P., Yan, G., & Ritterband, L. M. (2016). Insomnia in epilepsy is associated with continuing seizures and worse quality of life. *Epilepsy Research*, *122*, 91–96. https://doi.org/10.1016/j.eplepsyres.2016.02.014

Raman, I. M., Sprunger, L. K., Meisler, M. H., & Bean, B. P. (1997). Altered Subthreshold Sodium Currents and Disrupted Firing Patterns in Purkinje Neurons of Scn8a Mutant Mice. *Neuron*, *19*(4), 881–891.

Ranck, J. B. (1984). Head direction cells in the deep cell layer of dorsolateral pre-subiculum in freely moving rats. In *Society for Neuroscience Abstracts* (Vol. 10, p. 176.12).

Rashidy-Pour, A., Motaghed-Larijani, Z., & Bures, J. (1995). Reversible inactivation of the medial septal area impairs consolidation but not retrieval of passive avoidance learning in

rats. *Behavioural Brain Research*, *72*(1–2), 185–188. https://doi.org/10.1016/0166-4328(96)00136-2

Richard, J. M., Ambroggi, F., Janak, P. H., & Fields, H. L. (2016). Ventral Pallidum Neurons Encode Incentive Value and Promote Cue-Elicited Instrumental Actions. *Neuron*, *90*(6), 1165–1173. https://doi.org/10.1016/j.neuron.2016.04.037

Richard, J. M., Stout, N., Acs, D., & Janak, P. H. (2018). Ventral pallidal encoding of reward-seeking behavior depends on the underlying associative structure. *ELife*, *7*, 1–25. https://doi.org/10.7554/elife.33107

Rinaldi, A., Oliverio, A., & Mele, A. (2012). Spatial memory, plasticity and nucleus accumbens. *Reviews in the Neurosciences*, *23*(5–6), 527–541. https://doi.org/10.1515/revneuro-2012-0070

Robinson, T. E., Yager, L. M., Cogan, E. S., & Saunders, B. T. (2014). On the motivational properties of reward cues: Individual differences. *Neuropharmacology*, *76*(PART B), 450–459. https://doi.org/10.1016/j.neuropharm.2013.05.040

Root, D. H., Melendez, R. I., Zaborszky, L., & Napier, T. C. (2015). The ventral pallidum: Subregion-specific functional anatomy and roles in motivated behaviors. *Progress in Neurobiology*, *130*, 29–70. https://doi.org/10.1016/j.pneurobio.2015.03.005

Rothschild, G., Eban, E., & Frank, L. M. (2017). A cortical-hippocampal-cortical loop of information processing during memory consolidation. *Nature Neuroscience*, *20*(2), 251–259. https://doi.org/10.1038/nn.4457

Russell, N. A., Horii, A., Smith, P. F., Darlington, C. L., & Bilkey, D. K. (2006). Lesions of the vestibular system disrupt hippocampal theta rhythm in the rat. *Journal of Neurophysiology*, *96*(1), 4–14. https://doi.org/10.1152/jn.00953.2005

Salgado, S., & Kaplitt, M. G. (2015). The nucleus accumbens: A comprehensive review. *Stereotactic and Functional Neurosurgery*, *93*(2), 75–93. https://doi.org/10.1159/000368279

Saunders, B. T., O'Donnell, E. G., Aurbach, E. L., & Robinson, T. E. (2014). A cocaine context renews drug seeking preferentially in a subset of individuals. *Neuropsychopharmacology*, *39*(12), 2816–2823. https://doi.org/10.1038/npp.2014.131

Scammell, T. E., Arrigoni, E., & Lipton, J. O. (2017). Neural Circuitry of Wakefulness and Sleep. *Neuron*, *93*(4), 747–765. https://doi.org/10.1016/j.neuron.2017.01.014

Schlingloff, D., Káli, S., Freund, T. F., Hájos, N., & Gulyás, A. I. (2014). Mechanisms of sharp wave initiation and ripple generation. *Journal of Neuroscience*, *34*(34), 11385–11398. https://doi.org/10.1523/JNEUROSCI.0867-14.2014

Schultheiss, N. W., Schlecht, M., Jayachandran, M., Brooks, D. R., McGlothan, J. L., Guilarte, T. R., & Allen, T. A. (2020). Awake delta and theta-rhythmic hippocampal network modes during intermittent locomotor behaviors in the rat. *Behavioral Neuroscience*, *134*(6), 529–546. https://doi.org/10.1037/bne0000409

Séguinot, V., Maurer, R., & Etienne, A. S. (1993). Dead reckoning in a small mammal: the evaluation of distance. *Journal of Comparative Physiology A*, *173*(1), 103–113. https://doi.org/10.1007/BF00209622

Sharp, P. E., Tinkelman, A., & Cho, J. (2001). Angular velocity and head direction signals recorded from the dorsal tegmental nucleus of gudden in the rat: Implications for path integration in the head direction cell circuit. *Behavioral Neuroscience*, *115*(3), 571–588. https://doi.org/10.1037//0735-7044.115.3.571

Sheeran, W. M., & Ahmed, O. J. (2020). The neural circuitry supporting successful spatial navigation despite variable movement speeds. *Neuroscience and Biobehavioral Reviews*, *108*(September 2019), 821–833. https://doi.org/10.1016/j.neubiorev.2019.11.013

Siegel, J. M. (2008). Do all animals sleep? *Trends in Neurosciences*, *31*(4), 208–213. https://doi.org/10.1016/j.tins.2008.02.001

Sjulson, L., Peyrache, A., Cumpelik, A., Cassataro, D., & Buzsáki, G. (2018). Cocaine Place Conditioning Strengthens Location-Specific Hippocampal Coupling to the Nucleus Accumbens. *Neuron*, *98*(5), 926-934.e5. https://doi.org/10.1016/j.neuron.2018.04.015

Smith, K. S., Tindell, A. J., Aldridge, J. W., & Berridge, K. C. (2009). Ventral pallidum roles in reward and motivation. *Behavioural Brain Research*, *196*(2), 155–167. https://doi.org/10.1016/j.bbr.2008.09.038

Sors, A., Bonnet, S., Mirek, S., Vercueil, L., & Payen, J. F. (2018). A convolutional neural network for sleep stage scoring from raw single-channel EEG. *Biomedical Signal Processing and Control*, *42*, 107–114. https://doi.org/10.1016/j.bspc.2017.12.001

Sosa, M., Joo, H. R., & Frank, L. M. (2020). Dorsal and Ventral Hippocampal Sharp-Wave Ripples Activate Distinct Nucleus Accumbens Networks. *Neuron*, *105*(4), 725-741.e8. https://doi.org/10.1016/j.neuron.2019.11.022

Spalla, D., Treves, A., & Boccara, C. N. (2022). Angular and linear speed cells in the parahippocampal circuits. *Nature Communications*, *13*(1907), 1–13. https://doi.org/10.1038/s41467-022-29583-z

Specchio, N., & Curatolo, P. (2021). Developmental and epileptic encephalopathies: What we do and do not know. *Brain*, *144*(1), 32–43. https://doi.org/10.1093/brain/awaa371

Spencer, S. S., Goncharova, I. I., Duckrow, R. B., Novotny, E. J., & Zaveri, H. P. (2008). Interictal spikes on intracranial recording: Behavior, physiology, and implications. *Epilepsia*, *49*(11), 1881–1892. https://doi.org/10.1111/j.1528-1167.2008.01641.x

Stackman, R. W., & Taube, J. S. (1998). Firing properties of rat lateral mammillary single units: Head direction, head pitch, and angular head velocity. *Journal of Neuroscience*, *18*(21), 9020–9037. https://doi.org/10.1523/jneurosci.18-21-09020.1998

Stafstrom, C. E. (2007). Persistent Sodium Current and Its Role in Epilepsy. *Current Review in Basic Science*, *7*(1), 15–22.

Tachibana, Y., & Hikosaka, O. (2012). The Primate Ventral Pallidum Encodes Expected Reward Value and Regulates Motor Action. *Neuron*, *76*(4), 826–837. https://doi.org/10.1016/j.neuron.2012.09.030

Takahashi, S., Yamamoto, S., Okayama, A., Araki, A., Saitsu, H., Matsumoto, N., & Azuma, H. (2015). Electroclinical features of epileptic encephalopathy caused by SCN8A mutation. *Pediatrics International*, *57*(4), 758–762. https://doi.org/10.1111/ped.12622

Taube, J. S., Muller, R. U., & Ranck, J. B. (1990a). Head-direction cells recorded from the postsubiculum in freely moving rats. I. Description and quantitative analysis. *Journal of Neuroscience*, *10*(2), 420–435. https://doi.org/10.1523/jneurosci.10-02-00420.1990

Taube, J. S., Muller, R. U., & Ranck, J. B. (1990b). Head-direction cells recorded from the postsubiculum in freely moving rats. II. Effects of environmental manipulations. *Journal of Neuroscience*, *10*(2), 436–447. https://doi.org/10.1523/jneurosci.10-02-00436.1990

Taube, Jeffrey S. (1995). Head direction cells recorded in the anterior thalamic nuclei of freely moving rats. *Journal of Neuroscience*, *15*(1 I), 70–86. https://doi.org/10.1523/jneurosci.15-01-00070.1995

Taube, Jeffrey S. (1998). Head direction cells and the neurophysiological basis for a sense of direction. *Progress in Neurobiology*, *55*(3), 225–256. https://doi.org/10.1016/S0301-0082(98)00004-5

Taube, Jeffrey S. (2007). The head direction signal: Origins and sensory-motor integration. *Annual Review of Neuroscience*, *30*, 181–207. https://doi.org/10.1146/annurev.neuro.29.051605.112854

Taube, Jeffrey S., & Bassett, J. P. (2003). Persistent Neural Activity in Head Direction Cells. *Cerebral Cortex*, *13*(11), 1162–1172. https://doi.org/10.1093/cercor/bhg102

Tiesinga, P., & Sejnowski, T. J. (2009). Cortical Enlightenment: Are Attentional Gamma Oscillations Driven by ING or PING? *Neuron*, *63*(6), 727–732. https://doi.org/10.1016/j.neuron.2009.09.009

Tindell, A. J., Berridge, K. C., Zhang, J., Peciña, S., & Aldridge, J. W. (2005). Ventral pallidal neurons code incentive motivation: Amplification by mesolimbic sensitization and amphetamine. *European Journal of Neuroscience*, *22*(10), 2617–2634. https://doi.org/10.1111/j.1460-9568.2005.04411.x

Torromino, G., Autore, L., Khalil, V., Mastrorilli, V., Griguoli, M., Pignataro, A., Centofante, E., Biasini, G. M., De Turris, V., Ammassari-Teule, M., Rinaldi, A., & Mele, A. (2019). Offline ventral subiculum-ventral striatum serial communication is required for spatial memory consolidation. *Nature Communications*, *10*(1), 1–9. https://doi.org/10.1038/s41467-019-13703-3

Trouche, S., Koren, V., Doig, N. M., Ellender, T. J., El-Gaby, M., Lopes-dos-Santos, V., Reeve, H. M., Perestenko, P. V., Garas, F. N., Magill, P. J., Sharott, A., & Dupret, D. (2019). A Hippocampus-Accumbens Tripartite Neuronal Motif Guides Appetitive Memory in Space. *Cell*, *176*(6), 1393-1406.e16. https://doi.org/10.1016/j.cell.2018.12.037

Tsanov, M. (2017). Speed and oscillations: Medial septum integration of attention and navigation. *Frontiers in Systems Neuroscience*, *11*(September), 1–15. https://doi.org/10.3389/fnsys.2017.00067

Tsanov, M., Chah, E., Vann, S. D., Reilly, R. B., Erichsen, J. T., Aggleton, J. P., & O'Mara, S. M. (2011). Theta-modulated head direction cells in the rat anterior thalamus. *Journal of Neuroscience*, *31*(26), 9489–9502. https://doi.org/10.1523/JNEUROSCI.0353-11.2011

Vachez, Y. M., Tooley, J. R., Abiraman, K., Matikainen-Ankney, B., Casey, E., Earnest, T., Ramos, L. M., Silberberg, H., Godynyuk, E., Uddin, O., Marconi, L., Le Pichon, C. E., & Creed, M. C. (2021). Ventral arkypallidal neurons inhibit accumbal firing to promote reward consumption. *Nature Neuroscience*, *24*(March). https://doi.org/10.1038/s41593-020-00772-7

Valerio, S., & Taube, J. S. (2012). Path integration: How the head direction signal maintains and corrects spatial orientation. *Nature Neuroscience*, *15*(10), 1445–1453. https://doi.org/10.1038/nn.3215

van der Meer, M. A. A., Ito, R., Lansink, C. S., & Pennartz, C. M. A. (2014). Hippocampal Projections to the Ventral Striatum: From Spatial memory to Motivated Behavior. *Space, Time and Memory in the Hippocampal Formation*, *March 2016*, 1–571. https://doi.org/10.1007/978-3-7091-1292-2

Van Twyver, H. (1969). Sleep patterns of five rodent species. *Physiology and Behavior*, *4*(6), 901–905. https://doi.org/10.1016/0031-9384(69)90038-9

Vanderwolf, C. H. (1969). Hippocampal Electrical Activity and Voluntary Movement in the Rat. *Electroencephalography and Clinical Neurophysiology*, *26*(4), 407–418. https://doi.org/10.1016/0013-4694(69)90092-3

Veeramah, K. R., O'Brien, J. E., Meisler, M. H., Cheng, X., Dib-Hajj, S. D., Waxman, S. G., Talwar, D., Girirajan, S., Eichler, E. E., Restifo, L. L., Erickson, R. P., & Hammer, M. F. (2012). De novo pathogenic SCN8A mutation identified by whole-genome sequencing of a family quartet affected by infantile epileptic encephalopathy and SUDEP. *American Journal of Human Genetics*, *90*(3), 502–510. https://doi.org/10.1016/j.ajhg.2012.01.006

Viejo, G., & Peyrache, A. (2020). Precise coupling of the thalamic head-direction system to hippocampal ripples. *Nature Communications*, *11*(1), 1–14. https://doi.org/10.1038/s41467-020-15842-4

Wagnon, J. L., Korn, M. J., Parent, R., Tarpey, T. A., Jones, J. M., Hammer, M. F., Murphy, G. G., Parent, J. M., & Meisler, M. H. (2015). Convulsive seizures and SUDEP in a mouse model of SCN8A epileptic encephalopathy. *Human Molecular Genetics*, *24*(2), 506–515. https://doi.org/10.1093/hmg/ddu470

Wang, D. V., Yau, H. J., Broker, C. J., Tsou, J. H., Bonci, A., & Ikemoto, S. (2015). Mesopontine median raphe regulates hippocampal ripple oscillation and memory consolidation. *Nature Neuroscience*, *18*(5), 728–735. https://doi.org/10.1038/nn.3998

Wengert, E. R., Miralles, R. M., Wedgwood, K. C. A., Wagley, P. K., Strohm, S. M., Panchal, P. S., Idrissi, A. M., Wenker, I. C., Thompson, J. A., Gaykema, R. P., & Patel, M. K. (2021). Somatostatin-Positive Interneurons Contribute to Seizures in SCN8A Epileptic Encephalopathy. *The Journal of Neuroscience : The Official Journal of the Society for Neuroscience*, *41*(44), 9257–9273. https://doi.org/10.1523/JNEUROSCI.0718-21.2021

Wengert, E. R., & Patel, M. K. (2021). The Role of the Persistent Sodium Current in Epilepsy. *Epilepsy Currents*, *21*(1), 40–47. https://doi.org/10.1177/1535759720973978

Wengert, E. R., Wenker, I. C., Wagner, E. L., Wagley, P. K., Gaykema, R. P., Shin, J. B., & Patel, M. K. (2021). Adrenergic Mechanisms of Audiogenic Seizure-Induced Death in a Mouse Model of SCN8A Encephalopathy. *Frontiers in Neuroscience*, *15*(March), 1–16. https://doi.org/10.3389/fnins.2021.581048

Whishaw, I. Q., & Vanderwolf, C. H. (1973). Hippocampal EEG and behavior: Change in amplitude and frequency of RSA (Theta rhythm) associated with spontaneous and learned movement patterns in rats and cats. *Behavioral Biology*, *8*(4), 461–484. https://doi.org/10.1016/S0091-6773(73)80041-0

Wilson, M. A., & McNaughton, B. L. (1994). Reactivation of Hippocampal Ensemble Memories During Sleep. *Science*, *265*(5172), 676–679.

Worrell, G. A., Parish, L., Cranstoun, S. D., Jonas, R., Baltuch, G., & Litt, B. (2004). High-frequency oscillations and seizure generation in neocortical epilepsy. *Brain*, *127*(7), 1496–1506. https://doi.org/10.1093/brain/awh149

Xu, M., Chung, S., Zhang, S., Zhong, P., Ma, C., Chang, W. C., Weissbourd, B., Sakai, N., Luo, L., Nishino, S., & Dan, Y. (2015). Basal forebrain circuit for sleep-wake control. *Nature Neuroscience*, *18*(11), 1641–1647. https://doi.org/10.1038/nn.4143

Yoder, R. M., & Pang, K. C. H. (2005). Involvement of GABAergic and cholinergic medial septal neurons in hippocampal theta rhythm. *Hippocampus*, *15*(3), 381–392. https://doi.org/10.1002/hipo.20062

Zhang, J., Yao, R., Ge, W., & Gao, J. (2020). Orthogonal convolutional neural networks for automatic sleep stage classification based on single-channel EEG. *Computer Methods and Programs in Biomedicine*, *183*, 105089. https://doi.org/10.1016/j.cmpb.2019.105089